

Development of the scintillating fibre tracker technology for the LHCb upgrade and the LHC beam profile monitoring system

THÈSE N° 8851 (2018)

PRÉSENTÉE LE 2 NOVEMBRE 2018
À LA FACULTÉ DES SCIENCES DE BASE
LABORATOIRE DE PHYSIQUE DES HAUTES ÉNERGIES 3
PROGRAMME DOCTORAL EN PHYSIQUE

ÉCOLE POLYTECHNIQUE FÉDÉRALE DE LAUSANNE

POUR L'OBTENTION DU GRADE DE DOCTEUR ÈS SCIENCES

PAR

Olivier Göran GIRARD

acceptée sur proposition du jury:

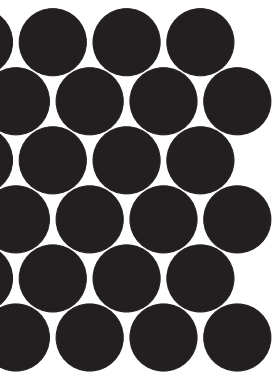
Prof. C. Hébert, présidente du jury
Prof. T. Nakada, Dr G. Haefeli, directeurs de thèse
Dr D. Gascón, rapporteur
Dr M. Ferro-Luzzi, rapporteur
Dr C. Bula, rapporteur



ÉCOLE POLYTECHNIQUE
FÉDÉRALE DE LAUSANNE

Suisse
2018

*If we knew what we were doing,
it wouldn't be called research.
— Albert Einstein*



Acknowledgements

Over this long period of four years, I have received support from many people whom I want to say a big "Thanks!" with these few lines.

My first acknowledgements go to my two thesis supervisors Tatsuya Nakada and Guido Haefeli. You made everything possible to integrate me in the projects of our lab and I have always felt a strong support for my contribution to our research. I have progressed a lot with the always very pertinent and challenging questions and feedbacks from Tatsuya regarding all possible aspects of my PhD project. When I look back, I realise how much I have learnt during these four years. I owe a large fraction of it to the very instructive supervision of Guido. You are very talented in teaching and debating the comprehensive picture of a complex problem. Under your guidance, I have been able to advance efficiently in my work and to develop a sharp critical thinking which is probably the most valuable skill for a physicist.

I would like to thank all my experimentalist colleagues and in particular Axel Kuonen and Maria Elena Stramaglia for the fruitful collaboration in setting up our lab experiments. You are the source of the so good atmosphere in the lab and at the test beams. We had also the chance to enjoy together some nice trips abroad for schools, workshops and conferences. It has been a pleasure to share my days with you two.

My work could only be achieved with the support of the electronic and mechanical workshops. I am very grateful to Raymond Frei (dit du cinquième), Guy Masson, Nicolas Auberson, Florian Bernard, Alain Pinard and Rodolfo Gonzalez for their infinite patience, their availability, their professionalism and their permanent good mood.

As a master project and at the beginning of my PhD, I spent a large part of my time on the BGV detector development and construction. I have learnt a lot through the collaboration with the BGV team and I would like to thank in particular Plamen Hopchev and Massimiliano Ferro-Luzzi for their feedbacks and their enthusiasm for this project.

What made all my time at the LPHE so enjoyable is the incredible good mood existing among colleagues. We have had fantastic lunch discussions – highlights are the philosophical input from Tatsuya and the honest apport from Pavol. After lunch, our *Soccer Physics* tournaments, which have become a tradition, brought excitement and emotions – thanks to my favorite opponents: Maxime, Brice, Axel, Lino, Pavol and Tara. I had also good times spent on correct-

Acknowledgements

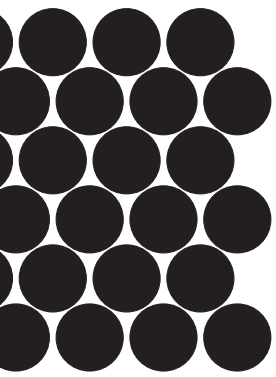
ing exams – thanks Olivier Schneider and Fred Blanc! –, playing the role of expert at exams or designing a big-enough detector demonstrator for outreach – thank you Aurelio Bay! In addition, I had no need to worry about administrative procedures or paperwork which are at the opposite of what I like doing, even on a Monday morning – a big thanks to the secretariat team: Erika, Esther and Corinne.

Quatre ans, c'est une longue période au cours de laquelle beaucoup de choses se passent en dehors de la vie professionnelle. J'ai eu la chance de pouvoir compter sur toute ma famille pour me permettre de suivre mes études. Vous m'avez toujours offert un environnement familial idéal pour me reposer, rigoler et grandir (de manière métaphorique car en taille, j'ai arrêté depuis un petit moment). Un grand merci donc à mes parents, ma sœur et mon frère.

Non, je ne t'ai pas oubliée, j'ai juste gardé le plus cher à mes yeux pour la fin. Je souhaite remercier infiniment ma femme, Aurore, pour tous les bons moments que nous avons vécus pendant mon doctorat. Nous étions "ensemble" au début des quatre ans et nous sommes maintenant aussi "mariés". Nous nous sommes adonnés pleinement à l'un de nos passe-temps favoris en profitant de voyager aux quatre coins du monde. Mon souvenir de ce doctorat est ainsi indéniablement attaché à ces road trips, ces croisières, ces balades et ces plongées. En plus de me donner toujours plus envie de faire de nouvelles découvertes, ces voyages et ta compagnie m'ont permis de recharger mes batteries et d'être plein de dynamisme et de motivation dans mon travail.

Lausanne, 18 June 2018

Olivier Girard



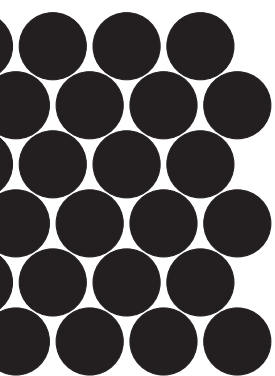
Abstract

The LHCb detector located at the large hadron collider (LHC) at CERN will undergo a major upgrade in 2019-2020. The detector will be prepared to operate at an increased instantaneous luminosity and to read out full events at 40 MHz. This requires many changes in the detector hardware as well as the full software implementation of the event selection. A large tracker has been developed and will be installed for particle tracking downstream of the magnet. It is based on 2.5 m-long scintillating fibres (SciFi) with 250 μm diameter read out by silicon photomultiplier (SiPM) multichannel arrays. A significant R&D effort has been devoted to tailor the technology to the large dimension and the radiation environment.

I have developed the instrumentation for the characterisation of SiPMs with a focus on the measurement of the radiation-induced damage. We achieve a precision of 3% on the measurement of the gain and photon detection efficiency (PDE) of SiPMs irradiated to $6 \cdot 10^{11} \text{ 1 MeV n}_{\text{eq}}/\text{cm}^2$, equivalent to the expected accumulated radiation in the LHCb SciFi tracker. The SiPM photodetector selected for the SciFi tracker features very low correlated noise (enabling a wide operation range) and a high PDE. The radiation damage is characterised by a dramatic increase in the dark count rate (typically 35 MHz/mm² at $\Delta V = 3.5 \text{ V}$ and -40°C for a device irradiated to $6 \cdot 10^{11} \text{ 1 MeV n}_{\text{eq}}/\text{cm}^2$) which is counteracted by cooling (-40°C), short signal integration time length (40 MHz read-out) and an efficient noise suppression algorithm (clustering). No significant change in gain, correlated noise and PDE due to irradiation has been observed. The expected light yield given by the fibres at the end of lifetime together with the estimated SiPM noise are in agreement with the required hit detection efficiency.

The beam-gas vertex (BGV) detector is an instrument dedicated to beam profile measurements at the LHC. A demonstrator based on the SciFi technology, installed in 2015, provides promising results and validates this detector concept for the high-luminosity LHC project.

Keywords: LHC, LHCb, Scintillating fibres, Silicon photomultipliers, Characterisation methods, Radiation-induced damage, Beam instrumentation.



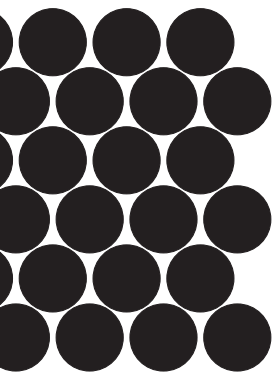
Résumé

Le détecteur LHCb, situé au grand collisionneur de hadrons (LHC) au CERN, sera mis à niveau en 2019-2020 afin de pouvoir prendre des données avec une plus grande luminosité instantanée et extraire les événements à une fréquence de 40 MHz. Plusieurs changements au niveau des composants du détecteur sont prévus, ainsi que l'implémentation de la sélection des événements purement en software. Un système permettant la mesure de trajectoire des particules sur une grande surface en aval de l'aimant sera installé. Son fonctionnement repose sur des fibres scintillantes (SciFi) d'une longueur de 2.5 m et d'un diamètre de 250 μm et des photomultiplicateurs en silicium (SiPMs). Un effort considérable a été essentiel afin d'adapter cette technologie à la grande taille du détecteur LHCb et à l'environnement de radiation auquel il sera exposé.

J'ai développé l'instrumentation nécessaire pour la caractérisation des SiPMs et en particulier pour la mesure des effets dus à la radiation. Les setups de mesures permettent de déterminer le gain et l'efficacité de détection des photons (PDE) avec une précision de 3% pour des détecteurs irradiés à $6 \cdot 10^{11} \text{ 1 MeV n}_{\text{eq}}/\text{cm}^2$, correspondant à la radiation accumulée dans le détecteur SciFi. Le SiPM sélectionné pour le détecteur se distingue par un très bas niveau de bruit corrélé et un haut PDE. L'effet le plus important de l'irradiation est une augmentation considérable du bruit aléatoire (typiquement 35 MHz/mm² à $\Delta V = 3.5 \text{ V}$ et -40°C pour un photodétecteur irradié à $6 \cdot 10^{11} \text{ 1 MeV n}_{\text{eq}}/\text{cm}^2$). Pour contrer ce type de bruit, les SiPMs seront refroidis à -40°C , la fenêtre d'intégration du signal sera minimisée (lecture du détecteur à 40 MHz) et un algorithme efficace de suppression du bruit sera implémenté (clustering). Les mesures présentées dans ce travail montrent que le gain, le bruit corrélé ainsi que le PDE ne changent pas de manière conséquente après irradiation. La quantité de lumière à la sortie des fibres à la fin de vie du détecteur ainsi que les estimations du niveau de bruit venant du SiPM permettent d'envisager le fonctionnement du détecteur avec l'efficacité de détection requise.

Un instrument consacré à la mesure du profil des faisceaux de protons du LHC a été développé. Un démonstrateur basé sur la même technologie que le détecteur SciFi a été installé en 2015. Les résultats prometteurs obtenus permettent de valider le concept de cet instrument pour le projet du HL-LHC.

Mots-clés : LHC, LHCb, Fibres scintillantes, Photomultiplicateur en silicium, Méthodes de caractérisation, Effets induits par la radiation, Instrumentation du faisceau.

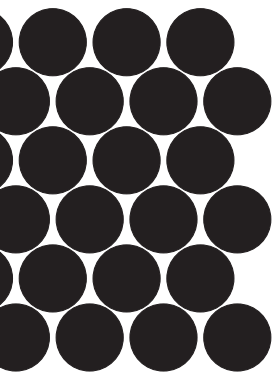


Contents

Acknowledgements	v
Abstract (English/Français)	vii
List of figures and tables	xvii
Introduction	1
1 The LHCb detector and its upgrade	3
1.1 The LHCb current detector	3
1.1.1 Vertex locator	5
1.1.2 Silicon tracker	6
1.1.3 Outer tracker	6
1.1.4 Track reconstruction	7
1.2 Upgrade conditions and new requirements	8
1.2.1 Hardware changes	8
1.2.2 Software trigger	9
1.3 The Scintillating fibre tracker	10
1.3.1 Design overview	10
1.3.2 Requirements and radiation environment	10
2 Photodetectors in high energy physics	13
2.1 Light sources	13
2.2 Review of photodetectors	14
2.2.1 Vacuum-based photodetectors	15
2.2.2 Solid-state photodetectors	17
2.2.3 Hybrid photodetectors	19
2.2.4 Gaseous photodetectors	19
2.3 Silicon photomultipliers	20
2.3.1 Working principle	20
2.3.2 Breakdown voltage	21
2.3.3 Pulse shape and gain	22
2.3.4 Dark count rate	23
2.3.5 Photon detection efficiency	24
2.3.6 Correlated noise	25
2.3.7 Radiation damage	26

3	LHCb scintillating fibre tracker	29
3.1	The SciFi technology	29
3.1.1	Scintillating fibres	29
3.1.2	Working principle and clustering	31
3.1.3	Light yield	33
3.2	Detector design and fabrication	34
3.2.1	Fibre module fabrication	35
3.2.2	Silicon photomultiplier multichannel array	36
3.2.3	Read-out electronics	38
3.2.4	Cooling and mechanical infrastructures	39
4	Silicon photomultiplier characterisation	41
4.1	Experimental methods overview	41
4.2	Waveform analysis and correlated noise measurement	42
4.2.1	Measurement setup and analysis method	43
4.2.2	Results for H2017 detectors	45
4.2.3	Correlated noise at -40°C	48
4.2.4	Direct cross-talk of irradiated detectors	49
4.2.5	Qualitative comparison with other works	50
4.3	Gain measurement	52
4.3.1	Results for an H2017 detector	53
4.3.2	Relative gain of irradiated detectors	53
4.4	Photon detection efficiency	54
4.4.1	Measurement setup	55
4.4.2	Method based on the current	56
4.4.3	Method based on the pulse frequency	57
4.4.4	Sources of systematic and statistical errors	58
4.4.5	Results for an H2017 detector	59
4.5	Current-voltage measurements	60
4.5.1	Breakdown voltage	60
4.5.2	Dark count rate	62
4.5.3	Quench resistor	62
5	SiPM multichannel array characterisation	65
5.1	Light yield measurement setup	65
5.2	Read-out of multichannel arrays	65
5.3	Breakdown voltage and ADC gain	68
5.3.1	Results for irradiated H2017 detectors	69
5.4	Light yield of a short fibre module	70
5.4.1	Correction for the DCR contribution	71
5.4.2	Light yield at -40°C	71
5.4.3	Light yield with irradiated H2017 detectors	72
5.5	Noise cluster rate	74
5.5.1	Measurements with SPIROC	74
5.5.2	Simulation based on SPIROC measurements	75

5.5.3	Simulation based on waveform measurements	75
6	Scintillating fibre tracker for LHC beam monitoring	79
6.1	The beam-gas vertex demonstrator	79
6.2	Fibre module read-out	81
6.2.1	Characterisation of the front-end electronics	82
6.2.2	Channel cross-talk	82
6.2.3	Zero-suppression implementation in the TELL1	85
6.3	Characterisation of a fibre module at test beam	86
6.3.1	Experimental setup	86
6.3.2	Light yield	87
6.3.3	Hit resolution	87
6.3.4	Hit detection efficiency	89
6.3.5	Hit detection efficiency in non-sensitive areas	90
	Conclusion and outlook	93
A	LHCb SciFi tracker module characterisation	95
A.1	Experimental setup	95
A.2	Light yield and attenuation length	95
A.3	Hit resolution	97
A.4	Hit detection efficiency and spillover	98
A.5	Radiation effects on fibre module performance	99
B	Characterisation of different SiPM types	101
B.1	Multichannel prototypes for the LHCb SciFi tracker	101
B.2	Single-channel devices	104
C	Beam size measurement techniques for the BGV detector	107
D	Cosmic particle tracker for outreach	109
	Bibliography	113
	Curriculum Vitae	121



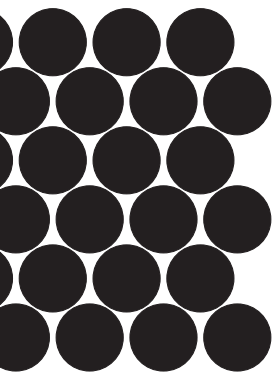
List of figures and tables

1.1	Schematic view of the LHCb detector.	4
1.2	Arrangement of the detector modules in the VELO along the beam axis.	5
1.3	VELO sensors in open or closed state.	5
1.4	Schematic view of the TT and IT.	6
1.5	Schematic view of the OT stations and their mechanical support.	7
1.6	Classification of reconstructed tracks in LHCb.	8
1.7	Layout of one station of the SciFi tracker.	11
2.1	Photomultiplier tube working principle.	15
2.2	Microchannel plate structure and illustration of the multiplication process. . .	16
2.3	Cross-section of an avalanche photodiode.	18
2.4	Current-voltage characteristic of an SiPM pixel in discharge.	21
2.5	Cross-section of an SiPM pixel with p -on- n or n -on- p structure.	21
2.6	Typical micro-structure implementation of SiPMs.	22
2.7	Equivalent circuit of an SiPM.	22
2.8	Generation of free charge carriers in a band diagram of the avalanche zone of an SiPM.	24
3.1	Electronic transitions leading to the emission of scintillation light and absorption and emission spectra of the fibre compounds.	30
3.2	Light capture and transport inside a scintillating fibre.	31
3.3	Signal formation in the SciFi tracker.	31
3.4	Illustration of the clustering algorithm.	32
3.5	Light yield of a short fibre module.	34
3.6	Picture of a cross-section of a fibre mat.	35
3.7	Pictures of the SiPM array package for the LHCb SciFi tracker.	37
3.8	Schematic views of the SciFi tracker modules with mechanical support, front-end electronics and cooling.	38
3.9	Encoding of the comparators output in the PACIFIC.	39
4.1	Examples of waveform recorded with the oscilloscope setup.	43
4.2	Illustration of the procedure to determine the breakdown voltage in the waveform analysis.	44
4.3	Correlated noise composition and contributions of higher order correlated noise and DCR for an H2017 detector.	46
4.4	Amplitude and time delay of classified correlated noise pulses.	46

List of figures and tables

4.5	Determination of pulse shape long decay time constant and recovery time. . .	47
4.6	Determination of the AP and DeXT mean lifetime and estimation of the contribution of random noise.	48
4.7	Correlated noise of H2017 detectors measured on a large sample.	49
4.8	Correlated noise at room temperature and at -40°C for an H2017 SiPM. . . .	50
4.9	Distribution of the time difference between two consecutive random pulses in the case of high DCR.	51
4.10	DiXT as a function of over-voltage for irradiated H2017 detectors at -40°C . . .	51
4.11	Pulse integral as a function of integration time.	54
4.12	Single-photon pulse integral as a function of ΔV for irradiated detectors. . . .	55
4.13	Sketch of the PDE measurement setup.	55
4.14	PDE as a function of wavelength and ΔV for an H2017 detector.	59
4.15	Results of the ΔV -dependent PDE fitted with an exponential function.	60
4.16	IV scan in reverse direction for the computation of the breakdown voltage. . .	61
4.17	DCR as a function of temperature for irradiated H2017 detectors.	62
5.1	Schemes and picture of the light yield measurement setup and the electron-gun.	66
5.2	Pulse shaping of VATA64, Beetle, SPIROC and PACIFIC.	66
5.3	Signal amplitude spectrum of a short fibre module in the dark or with electrons.	68
5.4	Example of photoelectron spectrum taken with VATA64.	68
5.5	ADC gain dependence on temperature for SPIROC read-out.	69
5.6	Photoelectron spectrum measured on non-irradiated and irradiated SiPMs with SPIROC electronics.	70
5.7	ADC gain for irradiated detectors read out by SPIROC.	71
5.8	Light yield measured with an H2017 detector operated at room temperature and at -40°C	72
5.9	Cluster sum distribution for electrons injected in the fibre module obtained with non-irradiated and irradiated H2017 detectors.	73
5.10	Noise cluster rate of irradiated H2017 detectors as a function of seed threshold, irradiation level and ΔV	74
5.11	Noise cluster rate as a function of DCR and ΔV	75
5.12	Dark spectrum of irradiated detectors obtained from a numerical integration of oscilloscope waveforms.	76
5.13	Comparison between the dark spectrum obtained from waveforms and from measurements with SPIROC.	77
5.14	Simulation of the noise cluster rate as a function of seed threshold for a detector irradiated to $3 \cdot 10^{11} \text{ 1 MeV } n_{\text{eq}}/\text{cm}^2$	77
5.15	Simulation of the noise cluster rate as a function of integration time for a detector irradiated to $3 \cdot 10^{11} \text{ 1 MeV } n_{\text{eq}}/\text{cm}^2$	78
6.1	Schematic view of the BGV demonstrator.	80
6.2	Pictures of the BGV detector after installation in November 2015.	80
6.3	Signal injector circuit for the Beetle board testing.	82
6.4	Beetle front-end electronics response and dynamic range.	83
6.5	Principle of cross-talk between two read-out channels on the Beetle board. . .	83

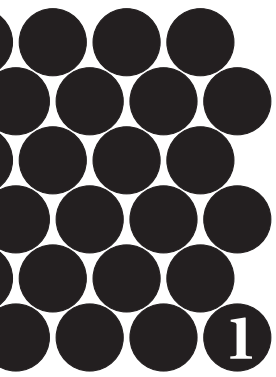
6.6	Channel correlation revealed by injection in a single channel of a front-end board.	84
6.7	Correlation between the signal of distant channels in a BGV fibre module. . . .	84
6.8	Impact of the channel correlation correction on clusters.	85
6.9	Schematic view of the test beam setup.	86
6.10	Picture of the test beam setup.	86
6.11	Cluster sum distribution for BGV fibre modules.	87
6.12	Residual distribution with the effect of the channel correlations and the cluster- ing thresholds.	88
6.13	Fit of the residual distribution.	89
6.14	Hit detection efficiency as a function of position and cluster thresholds.	90
6.15	Hit detection efficiency as a function of the light yield.	90
6.16	Hit detection efficiency in non-sensitive areas.	91
A.1	Test beam configurations at SPS and DESY.	96
A.2	Light yield of a long 6-layer fibre mat measured at test beam.	97
A.3	Residual distributions for a 6-layer mat with beam injection at the mirror side.	98
B.1	Pixel implementation in H2014, H2015 and H2017 devices.	101
B.2	Correlated noise composition of H2014 and H2015 detectors.	102
B.3	PDE as a function of wavelength and ΔV for Hamamatsu multichannel arrays.	103
B.4	Correlated noise composition of a KETEK prototype.	103
B.5	Pixel implementation for some single-channel devices available on the market.	104
B.6	Correlated noise composition and contributions of higher order correlated noise and DCR for a Hamamatsu single-channel device (S12572-050C).	104
B.7	Correlated noise composition and contributions of higher order correlated noise and DCR for an FBK single-channel device.	105
B.8	Correlated noise composition and contributions of higher order correlated noise and DCR for a SensL single-channel device (MicroES-SMA-30035-TSV-E32). . .	105
C.1	Event display of the BGV detector.	107
D.1	Picture of the cosmic tracker demonstrator.	110
D.2	Cosmic particle tracker event display.	111



Introduction

The LHCb experiment is located at the large hadron collider (LHC) at CERN. It studies the physical processes involved in collisions of high energetic particles using a complex detector system made of a combination of state-of-the-art technologies. The detector provides particle identification as well as the measurement of energy and momentum for all collision products. The particles present in the final state can originate from the decay of short-lived particles whose identification plays an important role in understanding the physical processes involved during interaction. Therefore, a detector is placed close to the interaction region and measures the trajectory of charged particles with high precision. The decay time of short-lived particles can be measured using vertex reconstruction. The trajectory of charged particles in a magnetic field is measured with several tracking detectors and allows to calculate the momentum. The energy is provided by the calorimeters which are sufficiently massive to stop the high energetic electrons, photons and hadrons by producing electromagnetic or hadronic showers. Finally, to improve the distinction between proton, pion, kaon and muon, the LHCb detector comprises a system based on the Cherenkov effect and a muon system.

The focus of my PhD work is the development of a detector technology based on scintillating fibres (SciFi) for particle tracking. I have contributed to the R&D and the construction of SciFi modules for the upgrade of the LHCb tracking system and for a new LHC beam monitoring system called the beam-gas vertex (BGV) detector. In chapter 1, I give a summary of the current experimental setup of the LHCb detector, the plans for the upgrade in 2019-2020 and a short introduction to the SciFi tracker. Chapter 2 presents a review on the photodetectors commonly used in high energy physics and describes in detail the silicon photomultiplier (SiPM) which is the technology used in the SciFi tracker. An overview of the LHCb SciFi tracker and its working principle is given in chapter 3. In the two next chapters 4 and 5, I describe various characterisation techniques for single- and multi-channel SiPMs and give the most relevant results. Finally, chapter 6 is dedicated to the BGV detector and my contribution to this project.



1 The LHCb detector and its upgrade

The LHC is CERN's and the world's largest particle accelerator and storage ring with a circumference of 27 km. It is situated in an underground tunnel between 50 and 175 m depth below the Swiss and French territory near Geneva. It is designed to accelerate two beams of protons in opposite direction from 450 GeV to 7 TeV energy. Lead or xenon ions can be accelerated instead of protons up to 2.8 TeV per nucleon. The particles are grouped in bunches separated by 25 ns and the two beams enter in collision with a frequency of 40 MHz at four interaction points. Four experiments, ATLAS, CMS, ALICE and LHCb, are devoted to study the collisions.

The LHCb experiment is optimised to study b - and c -hadrons and to find evidences for new physics in CP violation and rare decays [1]. At the LHC collision energy, most of the b - and \bar{b} -hadrons are produced in the same forward or backward cone with small opening angle with respect to the beam axis. This consideration has led to the conception of a spectrometer optimised for b -physics in forward direction. It is instrumented only in a fraction of the solid angle around the interaction point.

The LHCb detector has been operated during two data taking campaigns in 2011-2012 (Run 1) and 2015-present (Run 2). The instantaneous luminosity has been levelled down with respect to the nominal LHC design value by tuning the transverse overlap of the beams at the interaction point. The reduced luminosity has the advantage of decreasing the probability of multiple proton-proton (p - p) interactions per bunch crossing called the pile-up. This results in a lower detector occupancy. The experiment has collected data with a total integrated luminosity of 6.7 fb^{-1} from p - p interactions with centre-of-mass energy (\sqrt{s}) of 7 and 8 TeV (Run 1) and 13 TeV (Run 2). This chapter gives a short overview of the subsystems composing the detector with a focus on the tracking system as well as their upgrade planned for 2019-2020.

1.1 The LHCb current detector

The LHCb detector is a spectrometer covering a forward angle from 10 mrad to 300 (250) mrad in the bending (non-bending) plane [1]. Its layout is displayed in figure 1.1. For momentum measurement, the trajectory of charged particles is bent in the horizontal plane using a warm dipole magnet. The tracking is implemented with several devices. The *vertex locator* (VELO), surrounding the region close to the interaction point, provides a precise measurement of the

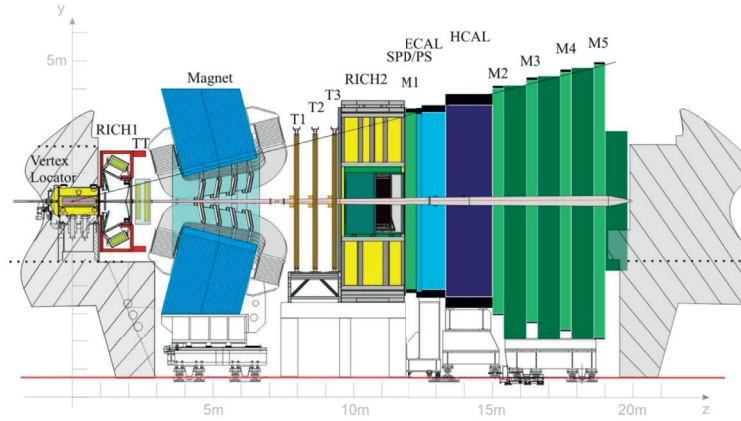


Figure 1.1 – Schematic side view of the LHCb detector. Image from [1].

track coordinates. It enables to identify the displaced secondary vertices which are distinctive features of b - and c -hadron decays [1]. The *silicon tracker* (ST) is composed of the *tracker turicensis* (TT) with two stations upstream of the magnet and the *inner tracker* (IT) with three stations close to the beam pipe downstream of the magnet. Each station comprises four detection planes. Finally, the outer tracker (OT) is situated downstream of the magnet and covers the outside of the acceptance not covered by the IT. The three stations after the magnet made of the IT and the OT are called the *T-stations* (T1-T3).

The other subsystems allow for particle identification and energy measurement. Two *ring imaging Cherenkov detectors* (RICH1 and RICH2) are employed to measure the velocity of charged particles using the Cherenkov effect in a mixture of silica aerogel and C_4F_{10} gas. In combination with the momentum measurement, this system enables to identify particles, in particular pions, kaons and protons. The calorimeter system consists of a *scintillating pad detector* (SPD), a *preshower detector* (PS) and the *electromagnetic* and *hadronic calorimeters* (ECAL and HCAL). All subsystems are made of multiple successive layers of scintillator and absorber (lead for ECAL and iron for HCAL). The SPD and PS are separated by a 1.5 cm-thick lead converter and are used to distinguish between electrons and photons. The ECAL stops electrons and photons but not the hadrons which are stopped in the HCAL. The total thickness of the calorimeters is 25 radiation lengths for ECAL and only 6 nuclear interaction lengths for HCAL (constrained by the space available). The high energy muons cannot be contained within the detector. Since they are present in many final states of b -hadron decays, their identification is a key ingredient for the measurement of the associated CP asymmetry and oscillation of mesons. They are detected by five muon stations (M1-M5). [2]

The data is sampled and stored on the on-detector front-end electronics. The events are filtered from the rate of 40 MHz to a maximum of 1.1 MHz by the *level-0 trigger* (L0) which is implemented in hardware. The b -mesons often decay in large transverse momentum (p_T) muons or large transverse energy (E_T) hadrons. The goal of the L0 trigger is to select events based on a high E_T hadron, electron or photon detected in the calorimeters or high p_T muons in the muon chambers. The distinction between electrons and photons is very important at the trigger level and, therefore, the information from the SPD and PS is integrated in the L0 trigger. In addition, two VELO upstream layers are used to estimate the number of primary

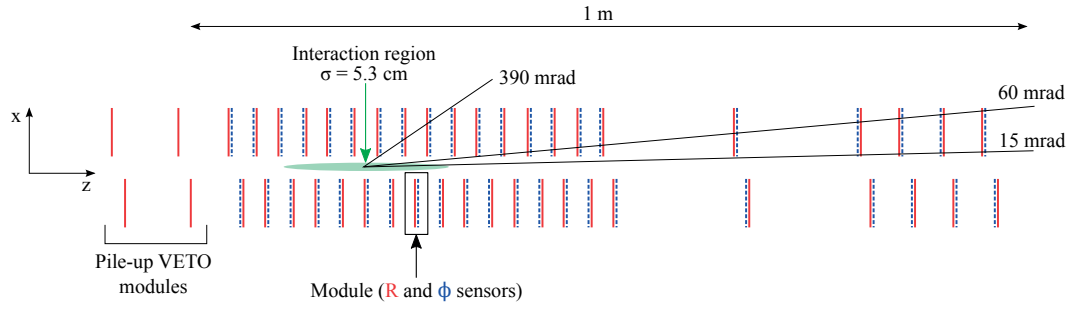


Figure 1.2 – View of a cross-section of the VELO detector in the horizontal plane at $y = 0$. Image from [1].

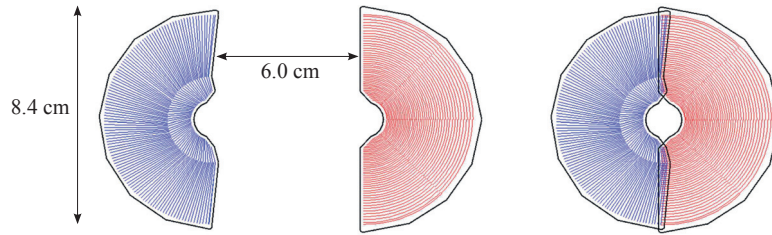


Figure 1.3 – Front view of a R (red) and ϕ (blue) sensor when the VELO is in open (left) and closed (right) state. Image from [1].

vertices and filter events with too high pile-up. After a positive decision from the L0 trigger, the complete detector is read out and the data is transmitted to the *high level trigger* (HLT). The HLT runs a simplified version of the offline event reconstruction and reduces the rate down to approximately 2 kHz for storage. [2]

1.1.1 Vertex locator

The VELO consists of a series of modules measuring the tracks position in a (r, ϕ, z) cylindrical coordinate system with the z -axis in the beam direction. The set up is approximately 1 m long and is divided in two sides. The arrangement of the modules along the beam axis is shown in figure 1.2. Each module is composed of a pair of half-discs of silicon microstrip detectors with azimuthal and quasi-radial strips. They provide the information on the position in r and ϕ (see figure 1.3). To cope with the high density of tracks, the strip pitch is as small as $38 \mu\text{m}$ in the part of the detector closest to the beam. During data taking, the radial distance of the closest sensitive area to the beam is only 8.2 mm. At beam injection, the two sides are retracted by 3 cm to prevent direct interaction with the beam. The VELO is mounted in a vacuum vessel separated by a thin aluminium foil from the LHC vacuum. This enables to protect the primary vacuum of the accelerator from possible contamination and serves also as a shield against RF noise from the beam.

The performance of the VELO detector was evaluated with Run 1 data [2, 3]. The resolution for the primary vertex position strongly depends on the number of tracks used for the vertex reconstruction. With 25 tracks, it is $13 \mu\text{m}$ and $71 \mu\text{m}$, in the transverse and longitudinal direction, respectively. The overall hit detection efficiency is 99.45% with only 0.6% of faulty

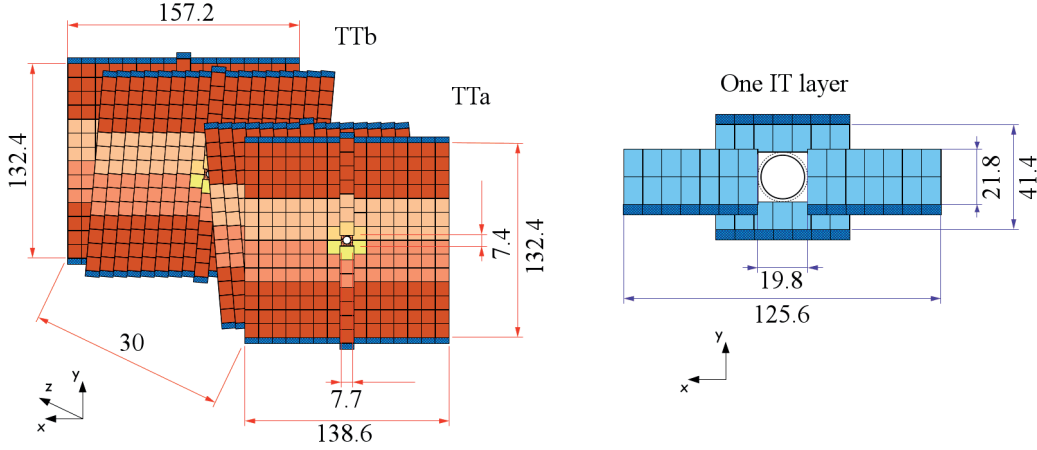


Figure 1.4 – Schematic view of the arrangement of the TT (left) and IT (right) silicon sensors (rectangles). The dimensions are given in cm. Image from [1, 4].

strips. The proximity of the silicon sensors to the beam resulted in a high radiation dose with a maximum value of $1.8 \cdot 10^{14} \text{ 1 MeV n}_{\text{eq}}/\text{cm}^2$ for the inner most strips after Run 1 operation. By the end of Run 2, it is expected to accumulate an additional $2.5 \cdot 10^{14} \text{ 1 MeV n}_{\text{eq}}/\text{cm}^2$. [3]

1.1.2 Silicon tracker

Silicon microstrip detectors cover the region with high track density in the upstream and downstream of the magnet. The TT and IT have a total area of 8 m^2 and 4 m^2 respectively. Each station is divided in four detection layers arranged in x - u - v - x configuration where x are strips oriented vertically and u (v) have stereo angle of -5° ($+5^\circ$). Figure 1.4 shows the layout of the TT and IT detectors where each rectangle represents a silicon strip sensor. The sensor size is approximately $10 \times 10 \text{ cm}^2$ with a strip pitch of $183 \text{ }\mu\text{m}$ for TT and $8 \times 11 \text{ cm}^2$ with pitch $198 \text{ }\mu\text{m}$ for IT. The TT sensors are read out by sectors depicted by the different colours in the figure. Within one sector, adjacent strips are directly bonded together. The IT sensors are placed in four boxes at each station located around the beam pipe. Each box contains seven detector modules and four detection layers. In the side boxes, the detector modules are made of two silicon strip sensors bonded together. Both TT and IT mechanical supports enable to retract the detectors from the beam line during maintenance periods.

During Run 1, the hit resolution of the TT and IT sensors was measured to be 53 and $50 \text{ }\mu\text{m}$, respectively. The intrinsic detection efficiency of the silicon strip sensors is above 99.7% for both trackers. However, several non-working channels have affected the overall efficiency.

1.1.3 Outer tracker

The OT is a drift-time gas detector made of an array of straw tubes. As shown in figure 1.5, it is divided in three stations with an area of $6 \times 5 \text{ m}^2$ each and a cut-out in the centre where the IT is placed. As in the silicon tracker, each station has four detection layers with x - u - v - x configuration. The stations are split in two half planes which are mounted on separate mechanical

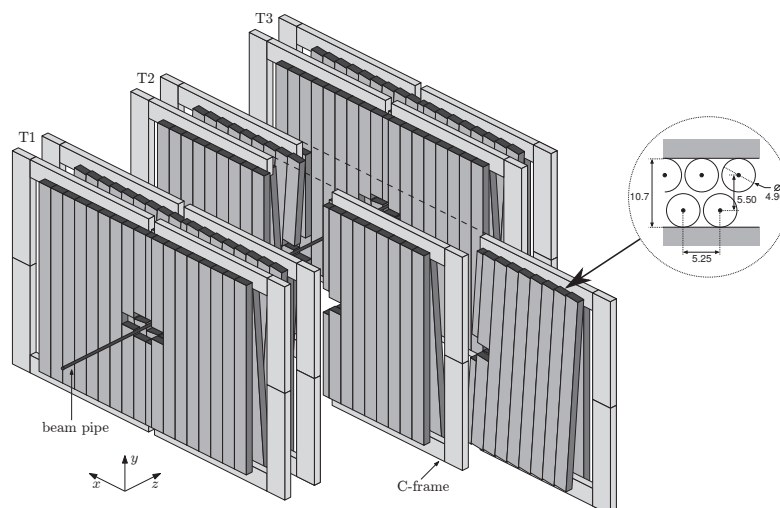


Figure 1.5 – Schematic view of the OT and its mechanical support with a zoom on a cross-section of the straw tube assembly (dimensions in mm). Image from [5].

supports such that the detector can be retracted from the beam line for maintenance. The drift tubes are 5 mm diameter and filled with a mixture of Ar (70%), CO₂ (28.5%) and O₂ (1.5%). The maximum drift time of the ionisation products from a crossing charged particle to the anode wire is approximately 35 ns. The resolution of this drift time measurement provides a position resolution of 200 μm . The detection efficiency of the straw tubes is 99.5% in the vicinity of the wire and only 50% close to the wall [5, 6].

1.1.4 Track reconstruction

Charged particle tracks are reconstructed by combining the hits measured in the VELO, TT, IT and OT. Different types of track are defined, depending on which subsystem is traversed, as illustrated in figure 1.6:

VELO tracks have typically large angle with respect to the beam axis or are even backward-oriented. They are useful for the reconstruction of the primary p - p vertex.

T tracks only have hits in the T-stations. They can be due to a secondary interaction between a particle originating from the p - p interaction and the detector material or from the decay of long-lived particles.

Long tracks are created from particles crossing the whole tracking system with hits in the VELO and the T-stations (optionally also in the TT). They feature very good momentum resolution.

Upstream tracks only cross the VELO and the TT and may create signal in the RICH1. They are used to study the background of the RICH particle identification algorithm.

Downstream tracks pass through the TT and the T-stations. They allow for the reconstruction of long-lived particles which decay outside the VELO sensitive volume.

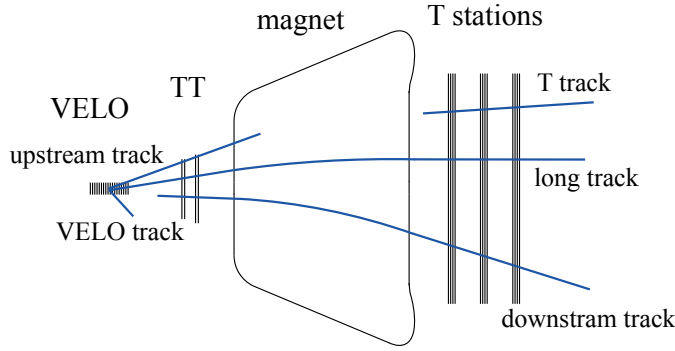


Figure 1.6 – Illustration of the different types of track determined by combining the information from all tracking subsystems. Image from [7].

To find long tracks an algorithm starts by searching for straight lines in the VELO with at least three hits in both R and ϕ sensors. Using the magnetic field map, this trajectory is extrapolated to the T-stations and different algorithms are applied to match the observed hits with the track. Finally, corresponding hits in the TT are eventually added to improve the momentum resolution. In the momentum range $[5, 200]$ GeV/c, the track finding efficiency was measured to be above 96% and the momentum resolution $\delta p/p$ between 0.5 and 1%. [2]

1.2 Upgrade conditions and new requirements

A first phase in the LHCb experiment's physics programme will end in 2018. The objective of the next phase is to exploit the luminosity of the LHC and to reduce the measurement error of CP violation observables down to the theoretical uncertainty level. For that purpose, the detector will undergo a major upgrade during the long shutdown 2 (LS2) in 2019-2020. The detector will be prepared to operate at an increased instantaneous luminosity ($2 \cdot 10^{33} \text{ cm}^{-2} \text{ s}^{-1}$ namely five times higher than in the current detector) and with a flexible trigger implemented all in software. The beam energy will be raised to the LHC design value for collisions with $\sqrt{s} = 14$ TeV centre-of-mass energy, resulting in increased cross-sections. The L0 trigger will be removed so that the full detector information will be read out and processed at 40 MHz in software. In this way, the event selection will be improved for the physics processes of interest and many signal yields will rise by typically one order of magnitude. The operation of the upgraded detector is planned for 50 fb^{-1} of collected data (about five times the amount taken during the first phase) for a data taking period of up to ten years. [8]

The removal of the L0 trigger requires 40 MHz triggerless read-out and the replacement of essentially all front-end electronics as well as the data acquisition system. The higher pile-up resulting from higher luminosities and increased cross-sections will lead to an increased occupancy and radiation damage which requires various changes in the detector hardware.

1.2.1 Hardware changes

The VELO sensors will be replaced with silicon pixel detectors ($200 \mu\text{m}$ thickness, $55 \times 55 \mu\text{m}^2$ pixels). The acceptance closest to the beam pipe will be increased by positioning the edge

of the innermost sensitive area as close as 5.1 mm to the beam. The choice of the pixel technology was driven by the high granularity and the ease of pattern recognition with respect to silicon strip detectors. After 50 fb^{-1} of integrated luminosity, a maximum hadron fluence of $8 \cdot 10^{15} \text{ 1 MeV n}_{\text{eq}}/\text{cm}^2$ in the sensors is expected. [9]

New high granularity silicon micro-strip detectors will instrument the tracking system upstream of the magnet (upstream tracker UT). It is a replacement for the current TT, however with larger coverage. To cope with the high occupancy, the innermost sensors feature a fine segmentation with $95 \text{ }\mu\text{m}$ strip-pitch, half of the pitch of outer sensors. [10]

A natural upgrade path for the T-stations would be to replace them with new OT and IT subsystems. However, progresses in photodetector technology allow to construct a large area scintillating fibre (SciFi) tracker giving sufficiently high spatial resolution and adequately low occupancies replacing both IT and OT with a single detector. In this way, there is no passive service material such as signal cables and cooling pipes within the acceptance. Furthermore, track finding software does not deal with different tracking systems depending on the region of phase space as before. Therefore, processing time can be reduced, which is crucial since the trigger will be based only on software. An overview of the layout and the requirements of the SciFi tracker is given in section 1.3. [10]

In the RICH detectors, the high occupancy will result in a too large overlap of the sparse photons coming from different tracks. To reduce this effect, the aerogel radiator will be removed and work with only the gas radiator. To recover the particle identification capability at low momentum, a time-of-flight system (TORCH) could be implemented at some later stage. The overall structure of RICH1 and RICH2 will remain unchanged whereas the photodetectors need to be replaced. [11]

The main changes in the calorimeter and muon systems are the removal of the SPD, PS and first muon station M1. All these subsystems have played an important role in the L0 trigger and are not required for the upgrade. No change in the hardware components of the ECAL and HCAL are foreseen. [11]

1.2.2 Software trigger

The new trigger architecture comprises a low and a high level trigger (LLT and HLT) implemented in software. The LLT will be present only in the early period of operation when the computing power is still insufficient to process all events. It is an evolution of the current L0 trigger, which is done in hardware, and uses limited information from the calorimeters and muon chambers [12]. Based on selection of events containing high E_T hadrons or high p_T muons, it can reduce the rate to 15 MHz. In the HLT, the use of the computing resource is optimised to bring the event reconstruction and selection as close as possible to the offline case. The online track reconstruction searches for particles with $p_T > 200 \text{ MeV}/c$ in the VELO and UT and then extrapolates them to the T-stations where hits compatible with $p_T > 500 \text{ MeV}/c$ are added. Next, a selection is performed based on the presence of individual tracks displaced from the primary vertex or of secondary vertices that can be due to the decay of heavy flavour hadrons [13]. The tunable parameters of the selection allow to reduce the rate down to approx-

imately 1 MHz after which the more complex algorithms such as the particle identification from the RICH detectors can be performed. Finally, based on the expected topology of the events of physical interest, the decision to accept the event for storage and further offline analysis can be taken. The information on the particles p_T and identity as well as the eventual presence of displaced secondary vertices are used in the decision making. The data storage bandwidth is limited to approximately 20 kHz. [12, 13]

The time budget for each processing step in the software trigger is tight. The track reconstruction deals with a large number of hits in many subdetectors and represents consequently about half of the budget. It plays a crucial role to reduce the rate allowing to perform more complex and computing-resource consuming algorithms in the next stages (i.e. track momentum calculation and particle identification). In comparison with the current offline event filtering, simulations show that the trigger algorithms foreseen for the upgrade run three times faster per event despite the higher event complexity. To a certain extent, this achievement is possible due to the simplified track reconstruction in the VELO and the design of the tracking system with a single detector technology (SciFi) for the T-stations. [12]

1.3 The Scintillating fibre tracker

This section gives an overview of the SciFi tracker design and requirements. The working principle and detailed design considerations are the subject of chapter 3. The active material are scintillating fibres of 250 μm diameter which generate light pulses from crossing particles and transport the signal to the read-out at their extremities outside the acceptance. This technological choice allows to cover the large area with sufficient granularity to cope with the occupancy in the inner region without any active or cooling services in the acceptance.

1.3.1 Design overview

The three T-stations are made of two half planes mounted on separated mechanical supports which are retractable from the beam pipe region, as shown in figure 1.7. They comprise four detection planes oriented in x - u - v - x configuration with 5° stereo angles. Each plane is made of staggered six-layer arrangements of fibres which are called *fibre mats*. The almost 5 m height of the acceptance is covered by two 2.4 m-long mats. A mirror is glued at the one end of the mats located in the middle whereas the photodetectors are only located at the top and bottom of the detector. The light is detected at the other end by multichannel SiPM arrays with 250 μm channel pitch. The SiPMs are installed in a cold box which enables their operation at -40°C necessary to mitigate the effect of radiation damage. [10]

1.3.2 Requirements and radiation environment

In order to provide a sufficient track finding efficiency, each plane of the tracker must have a hit detection efficiency as high as possible ($\sim 98\%$). This must go along with a low rate of noise hits to avoid so-called ghost tracks (tracks not matched to any charged particle). The requirement on the spatial resolution is 100 μm in the bending plane of the magnet. Since the

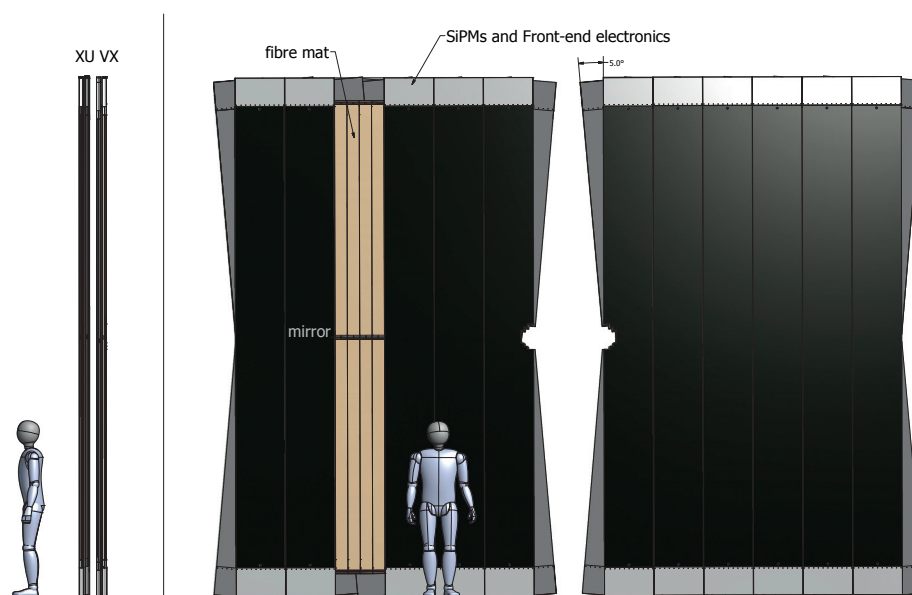


Figure 1.7 – Side (left) and front (right) view of one station of the SciFi tracker. The front view shows the left and right sides of the station retracted from the beam pipe. The arrangement of the fibre mats is shown in brown with the mirror in the middle, at the level of the beam pipe. Image from [14].

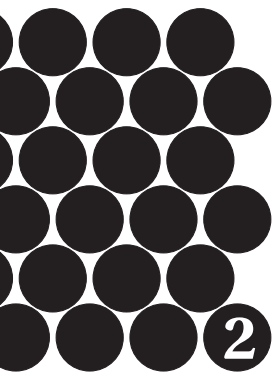
extrapolation of the track from the VELO is dominated by multiple scattering effects, better resolution is not needed. The material budget must not exceed a total of 1% of a radiation length per detection plane.

The electronics must cope with the 40 MHz read-out. The time duration of the signal from a crossing particle depends on the light generation (scintillator decay time), propagation in the fibre, the detection in the SiPMs and the signal shaping by the detector electronics. It must be short compared to 25 ns, the bunch crossing rate, in order to collect the signal within one LHC bunch crossings. Signal contaminating other bunch crossings, called spillover, results in undesired increased occupancy. [10]

The expected radiation environment after ten years of operation (50 fb^{-1} of collected data) has been simulated with FLUKA [15, 16, 17]^a. In the acceptance region, the fibres are exposed to charged particle induced dose whereas at the photodetector's location, the dominant radiation effect is due to neutrons. The irradiation profile of the fibres is very inhomogeneous and follows approximately a $1/r^2$ distribution where r is the distance from the beam centre. Close to the beam pipe, the maximum expected dose due to ionising radiation is 35 kGy. At read-out side, the neutron flux mainly originates from the ECAL situated downstream. A neutron shielding wall made of polyethylene with 5% of boron will be installed between the T-stations and the ECAL, at the location of the current M1 station. The wall is 30 cm thick in the inner region (from where most of the neutrons come) and 10 cm in the rest of the acceptance representing a total thickness of $X/X_0 \approx 60$ and 20%, respectively. It enables to reduce the neutron fluence by a factor of 2.5 and 3.4 for the SiPMs in T1 and T3 respectively, resulting in the expected values of 3.2 and $4.4 \cdot 10^{11} \text{ 1 MeV n}_{\text{eq}}/\text{cm}^2$. From the simulation, the effect of the

^a Assumptions: collision energy $\sqrt{s} = 14 \text{ TeV}$ and p - p inelastic interaction cross-section of 84 mb.

neutron shield on the calorimeters' performance was found to be negligible. The SiPMs will receive in addition an ionising dose of 50 and 100 Gy at T1 and T3 respectively. A 50 Gy dose is approximately equivalent to $5.7 \cdot 10^{10} \text{ 1 MeV n}_{\text{eq}}/\text{cm}^2$ [18]. The charged particle induced damage represents therefore about 15% of the total damage. [10]



2 Photodetectors in high energy physics

The passage of charged particles in matter can generate detectable electromagnetic radiation in the visible or near-visible spectrum. In high energy physics experiments, this phenomenon is exploited to provide the information on the particle type, energy and momentum. Thus, photon detectors are a key component of particle detectors. In the past, vacuum-based photodetectors and in particular photomultiplier tubes or hybrid photodetectors have been the most popular sensors used. Modern solid-state devices are now available for this type of applications and offer high detection efficiency, fine granularity, small size and design flexibility. One of the recent technological progress in the field is the silicon photomultiplier that can provide single photon detection, high gain, insensitivity to magnetic field and very good long-term stability. The disadvantages of this technology are the noise, temperature dependence of the internal amplification gain and radiation hardness. In this chapter, a review of the main photodetectors employed in high energy physics is given and the characteristics of silicon photomultipliers are described.

2.1 Light sources

Light sensitive devices are extensively used in daily life applications such as cameras or optical communication systems. Many high energy physics experiments also employ photosensors to detect visible or near-visible light produced by charged particles. In these applications, the photons are generated in scintillators or by Cherenkov radiation.

Scintillators are luminescent materials and are divided in two main categories: inorganic (typically crystals) and organic (typically plastics). The electron band structure of inorganic scintillators is at the origin of the light emission. The ionisation energy deposited by the charged particle excites valence electrons to the conduction band and photons are produced in the de-excitation process. To avoid direct re-absorption of the light inside the scintillator, localised intermediate energy levels are introduced in the band gap by adding impurities in the crystal. In this way, electrons in the conduction band are captured by the impurities and de-excite through the emission of optical photons with lower energy than the band gap. In organic scintillators, no band structure is present. The light emission arises from energy transitions of electrons in the molecular excitation levels. Also in this case, the energy of the

emitted photon is lower than the excitation energy. This explains the transparency of the medium to the emitted light. The shift in energy is due to the absorption by the molecules of a small fraction of the excitation through vibrations. The resulting offset between the light emission and absorption spectra is known as the Stokes shift. In both types, the production process typically yields 10^4 photons/MeV of deposited energy [19].

Inorganic scintillators have high density and are often used in calorimeter applications. Their emission spectrum peaks in the UV or blue region. The characteristic emission time is between 10 ns and 1 μ s which is almost too slow for detectors at the LHC. A typical application in the medical domain, which combines energy, position and time measurement is the time-of-flight positron emission tomography (TOF-PET). Here, two gamma rays emitted back-to-back from the $e^+ - e^-$ annihilation are identified and mapped back to the position of annihilation.

Organic scintillators are often plastics of low density and can therefore easily be shaped to the need of a particular application. Their spectrum peaks in the blue or green. The time of emission has typically a fast (fluorescence) and a slow (phosphorescence) component with characteristic time of 1 to 20 ns and $> 100 \mu$ s, respectively. Given their fast response and low density, they have a very wide range of applications such as sampling calorimeters, time-of-flight (TOF) detectors and tracking systems.

Cherenkov radiation is emitted if a charged particle travels in a dielectric medium faster than the speed of light in the medium. The emission is prompt which is useful in applications requiring fast particle timing information. The direction of emission is at a specific angle $\cos\theta = (n\beta)^{-1}$ where n is the refractive index of the medium (called a radiator) and β is the velocity of the particle. The emission spectrum is continuous but a large fraction is in the UV. The main applications are fast particle counters (TOF detectors) and hadron identification systems using the angle of emission (ring-imaging Cherenkov or RICH). In TOF detectors, scintillators are replaced by Cherenkov radiators in order to improve the time resolution. In astroparticle physics, Cherenkov radiation is used in neutrino detectors with particle tracking in low background environment (for example Super-Kamiokande [20] and IceCube [21]) and cosmic gamma ray telescopes with the atmosphere as radiator (imaging atmospheric Cherenkov telescopes as for example CTA [22]).

2.2 Review of photodetectors

The photodetectors are employed to convert the light to an electronic signal. To compare the most common types used in high energy physics, we define several characteristics determining the performance. The quantum efficiency (QE) is the probability that an incoming photon is converted into a photoelectron. For low light applications, the sensor generally includes a charge multiplication (gain) in order to overcome statistical fluctuations or electronic noise. The photon detection efficiency (PDE) is the probability that the incident photon generates a detectable electronic signal. Linearity of the signal with the number of incident photons as well as wide dynamic range are desired in many applications. All types of photodetector feature noise, often called dark noise or shot noise, which is signal uncorrelated with incident light. [23, 24]

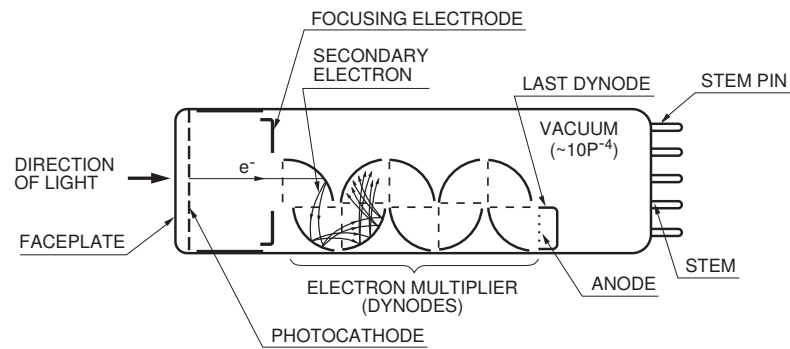


Figure 2.1 – Illustration of a photomultiplier tube and its working principle. Image from [25].

2.2.1 Vacuum-based photodetectors

In this type of photodetector, the photon conversion occurs in a cathode via the photoelectric effect. The produced photoelectron escapes the photocathode and is accelerated by an electric field to an electron amplification stage. The most common detector based on this principle is the photomultiplier tube (PMT), illustrated in figure 2.1. Material and thickness of photocathodes are optimised to obtain high quantum efficiency. The optimal thickness ensures high photon-interaction probability together with high electron-release probability. Semiconductor alloys containing alkali metals and antimony with typical QE in a range of 20 to 40% are used [25]. Certain types of photocathodes use special material at the surface such that the electron affinity (energy threshold for electron-release in vacuum) is negative leading to a higher sensitivity but also higher thermal noise.

The released photoelectron is accelerated by an electric field and hits a first multiplication electrode called the first dynode. The dynode surface enables a high emission rate of secondary electrons from a single incident accelerated electron. A PMT is composed of several dynodes which results in a gain in a range between 10^5 and 10^7 . The high voltage needed (up to several thousands of volts) and the high reactivity of the photocathode material impose the device to operate in vacuum. The transparency of the entrance window is crucial to allow for high photon detection efficiency. Borosilicate glass or quartz are chosen for their low wavelength cut-off below 300 nm. [24]

The number of electrons emitted at a dynode can be described by a Poisson statistic. The relative statistical fluctuation introduced by each dynode stage is therefore given by $1/\sqrt{\delta}$ where δ is the mean dynode gain. At the end of the amplification, the gain fluctuation of the PMT is dominated by the first stage. The generally large fluctuations can limit or even prevent single photon counting. The gain for each dynode is set with a voltage divider made of passive resistors and capacitors and the first dynode gain is chosen to be high (typically 25) to minimise the statistical fluctuation. Active instead of passive elements can be implemented in the voltage divider in order to improve linearity and operation stability.

PMTs are sensitive to magnetic field because of the deflection of electrons. To operate PMTs in a magnetic field, a shield made of high permittivity metal and optimised alignment angle between the PMT axis and the magnetic field are used. PMTs exist also with special dynode configurations for better electron collection efficiency, shorter transit time and improved

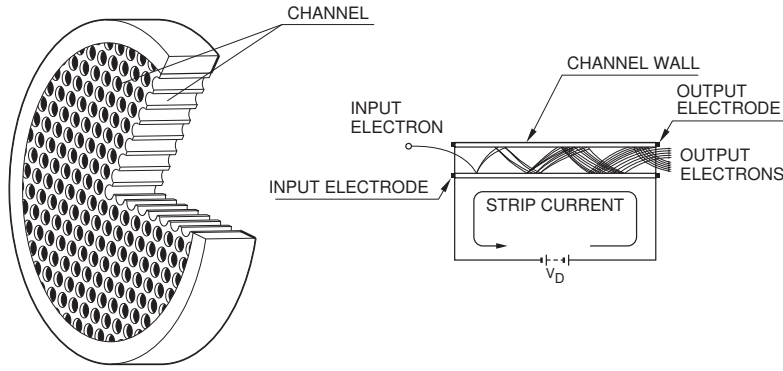


Figure 2.2 – Microchannel plate structure (left) and electron multiplication inside a microchannel (right). Image from [25].

magnetic field tolerance. In the latest developments, compact devices called flat panel PMTs use very thin metal electrode structures and segmented anodes for the photon position sensitivity. [24, 25]

Another type of vacuum-based photodetectors with similar working principle as a PMT is the microchannel plate (MCP). In this case, the electron multiplication occurs in a thin glass plate (~ 1 mm-thick) with 6 to 20 μm -diameter cylindrical capillaries (called channels), as illustrated in figure 2.2. The MCP is placed in an electric field between the photocathode and the anode. The channels inner wall act as a continuous dynode with a gain of up to 10^4 . Placing multiple MCPs one after the other enables higher gain. Operation in magnetic field is possible due to the small size of the device (only ~ 5 mm between cathode and anode). The anode can in addition be segmented (multianode) to measure the position of the incident photons. The main drawback of MCPs is the limited lifetime due to degradation of the photocathode. The residual gas present in the tube is ionised during the amplification process and migrates to the photocathode under the effect of the electric field leading to degradation. Two solutions exist to reduce this effect. Two MCPs can be placed one after the other with channels inclined with respect to the electric field's direction. An aluminium foil between the two MCPs or the first MCP and the photocathode can also be used to absorb the ions. This second solution results however in a reduced quantum efficiency. [24, 25]

Applications PMTs are very popular in RICH systems where single photon sensitivity together with low noise is required. To add spatial resolution, standard PMTs are replaced by multianode PMTs (MA-PMTs) or MCPs. An example of such an implementation is the detector of internally reflected Cherenkov light (DIRC) of the BaBar spectrometer at SLAC [26]. In the LHCb upgrade, flat panel MA-PMTs and MCPs with fine anode pitch are used in the RICH and the TORCH detectors ^a, respectively [11, 27, 28]. The particle identification detectors of the Belle II barrel is also instrumented with MCPs [29]. The good radiation hardness of PMTs and MCPs makes them suitable for calorimeters as for example the LHCb calorimeter system. Miniaturised MA-PMTs have been used in a small scintillating fibre tracker to measure the LHC absolute luminosity at the interaction point of ATLAS (ATLAS ALFA) [30].

^a The installation of the TORCH detector is planned for the LHCb phase 2 upgrade.

2.2.2 Solid-state photodetectors

Solid-state detectors can be built extremely compact. They are manufactured with the sub-micron semiconductor technology and allow therefore μm -size features. They can reach PDE beyond 50% and are insensitive to magnetic field. On the other side, they feature high noise and are sensitive to radiation-induced damage. The following discussion focuses on silicon devices which are the most common ones.

All semiconductor photodetectors are based on a p - n junction structure. At the junction, an electric field and a depleted zone are formed due to the alignment of the Fermi levels. The depletion allows to clear the zone from free thermal charge carriers. Light absorbed in the depleted region produces electron-hole (e - h) pairs which drift in the electric field and induce a measurable current. The minimum photon energy to create an e - h pair is equal to the band gap of silicon and corresponds to $1.1\ \mu\text{m}$ wavelength (infrared). The sensitivity of the device is nevertheless challenged by several phenomena. The large refractive index of silicon in the visible spectrum ($n > 3.5$) leads to a substantial loss of light due the Fresnel reflection (31% at normal incidence). An antireflective coating is applied on the surface in order to reduce this effect. The photon absorption length in silicon varies by five orders of magnitude from UV to infrared (10 nm to 1 mm respectively) which strongly affects the quantum efficiency. Once the photon is absorbed, charge carrier recombination can occur due to defects in the silicon. To reduce this, a passivation layer is applied to the surface.

The basic semiconductor device is the photodiode made of a single p - n junction where a reverse bias is applied in order to increase the thickness of the depletion zone and therefore the sensitive volume. A thicker depletion zone can be obtained by sandwiching a thick intrinsic silicon layer between two heavily doped layers at the electrodes (PIN diode). PIN diodes have low capacitance and fast response. Their main disadvantage is the absence of internal amplification. In order to produce a measurable signal, order of a thousand photons are needed.

In avalanche photodiodes (APDs), the doping profile is modified such that a high electric field is obtained, as shown in figure 2.3. In the zone called avalanche layer, charge carriers are accelerated and produce additional ionisation, called impact ionisation. Under the effect of the high electric field, the original and the additional carriers are accelerated and an avalanche is generated. In silicon, the ionisation rate of electrons is about three times larger than the one of holes. As a consequence, the doping profile is optimised to ensure that the electrons (rather than the holes) cross the entire avalanche region. The APD structure is adapted to specific wavelengths of incident light. Red and blue light sensitive devices have different structures to cope with the absorption depth. Figure 2.3 presents the cross-section of a typical APD optimised for infrared light detection. As shown, the photons absorbed inside the avalanche zone undergo incomplete multiplication. Consequently, the gain of APDs is wavelength dependent which affects the photon detection efficiency. Typical values for the gain are in the range between 50 and 200. The avalanche process is very sensitive to the electric field and therefore depends on the bias voltage (V_{bias}). Furthermore, the thermal-induced lattice vibrations limit the gain in energy of electrons and therefore the impact ionisation. Thus, the gain strongly decreases with temperature [31]. The avalanche introduces large statistical

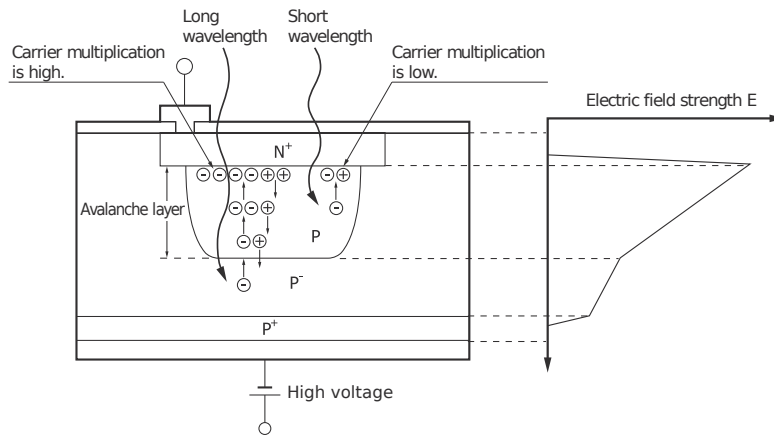


Figure 2.3 – Cross-section of an avalanche photodiode (near infrared type) with depiction of the electric field strength across the diode. Image from [31].

fluctuations preventing single-photon sensitivity [32, 33].

APDs are operated at a bias voltage sufficient to enable impact ionisation from the electrons but not from the holes. If ionisation from the holes occurs, the avalanche becomes self-sustaining. The threshold voltage for self-sustaining avalanches is known as the breakdown voltage (V_{BD}). APDs operated above V_{BD} are called Geiger-Müller APDs (GM-APDs) or single-photon avalanche diodes (SPADs). To terminate (quench) the self-sustaining avalanche, V_{bias} must be reduced below V_{BD} . This is usually done with a passive serial resistor (called quench resistor R_Q) or with an active quenching circuit. The gain of GM-APDs is in the range of 10^5 to 10^7 . The signal is extremely rapid which makes GM-APDs good timing devices with a resolution better than 100 ps. A large drawback for this detector is the noise which is produced by thermal charge carriers (typical rate in the order of 100 kHz/mm²) and is indistinguishable from signal produced by light. Another inconvenience is the absence of photon counting capability because the number of carriers generated in the self-sustaining avalanche is independent from the number of incoming photons. [24]

To enable photon counting, an array of GM-APDs can be connected in parallel. These devices are called silicon photomultipliers (SiPMs). Each GM-APD, called pixel or microcell (typical size of 10×10 to $100 \times 100 \mu\text{m}^2$), has its own quenching circuit. The signal is the sum of the individual pixels' signal. For low intensity light, the signal is proportional to the number of photons detected.

Applications Solid-state photodetectors are competing with vacuum-based devices for many existing applications [23]. Some of their advantages are the insensitivity to magnetic field, the robustness and the compactness, the fine granularity and the possible operation at relatively low voltage. PIN diodes are used for the read-out of high light yield scintillating crystals in calorimeters [24] as for example in the BaBar electromagnetic calorimeter [34]. Despite their high PDE, large dynamic range and good linearity, they are also sensitive to the ionisation produced by charged particles. APDs with thinner depletion layer can reduce this effect and provide a better sensitivity to low light intensity. They are applied for example in the CMS calorimeter [35]. A combination of photodiode and APD has been implemented for

example with BGO crystals in the calorimeter of the CALET experiment on the international space station. It enables to measure the energy of cosmic electrons and gamma rays over six orders of magnitude [36].

A clear trend in the last ten years is the use of SiPMs in many particle physics applications such as TOF detectors, calorimeters and fibre trackers. SiPMs optimised for low thermal noise are also potential candidates for RICH systems. Low noise can be achieved by a short signal integration time window and by reducing the active surface [24]. The latter can be realised by focusing the light with microlenses implemented on top of each pixel. Given their extremely fast response, SiPMs are also excellent candidates for applications with time resolution below 100 ps. An example is the timing detector under investigation for the CMS detector phase 2 upgrade [37].

2.2.3 Hybrid photodetectors

Hybrid photodetectors (HPDs) combine the technology of vacuum-based and solid-state devices. The photon conversion is implemented in a photocathode whereas the photoelectron amplification and detection occurs in a pixelised silicon sensor. In this way, a large area can be covered with the cathode and good spatial resolution can be achieved. Using a high electric field between the photocathode and the silicon sensor, the photoelectron is accelerated to the sensor where it creates a few thousands e - h pairs. Further amplification can be achieved using an APD instead of a simple photodiode (HAPD) reaching a gain of 10^5 . The electric field can be shaped to focus the photoelectrons from the cathode onto a small area sensor. This configuration is called "fountain-focused" as opposed to "proximity-focused" where one-to-one mapping from cathode to sensor is implemented. As in the case of PMTs, special care must be taken for the operation of HPDs in a magnetic field. HPDs have excellent individual photon separation and timing resolution of 50 ps on single photons is achievable [38].

Applications HPDs are very flexible in their design and implementation. Fountain-focused HPDs typically offer to cover a large area with high sensitivity and good granularity. Examples are the HPDs of the LHCb RICH detector [39]. Proximity-focused HAPDs are applied in the new aerogel RICH of the Belle II spectrometer [40]. Such photodetectors are also under consideration for the next generation of massive Cherenkov detectors such as the Hyper-Kamiokande project [41].

2.2.4 Gaseous photodetectors

Two types of gaseous photodetectors exist. In the first, the photon conversion occurs in a solid photocathode whereas in the second, it occurs in the gas mixture itself. The usual photosensitive gas mixtures are tetrakis dimethylamine ethylene (TMAE) and triethylamine (TEA) and are only sensitive to UV or extreme UV light. Small concentration of oxygen alters the quantum efficiency of the gas mixture and therefore very high gas purity is required on the long term in order to maintain good performance. The photoelectron produced in the solid photocathode or the gas travels to the anode where a high electric field is present and enables the generation of an avalanche. The electrical signal is dominated by the drift of the

ions created during the avalanche and travelling all the way to the cathode. Due to their low mobility in the gas, the ions are not substantially affected by the presence of a magnetic field. As a result, this type of photodetector can cope with high magnetic fields. Another advantage is the low cost which enables large area coverage. [23, 24]

Applications Gaseous photodetectors have been applied in RICH detectors because of their large area. An example is the ALICE RICH system which uses multi-wire pad chambers with CsI photocathode to detect Cherenkov light [42].

2.3 Silicon photomultipliers

As introduced in section 2.2.2, the SiPM is composed of an array of GM-APD pixels connected in parallel. This section first explains the working principle of these photodetectors. Second, it discusses in detail the main properties of SiPMs such as signal pulse shape, noise, photon detection efficiency and radiation effects.

2.3.1 Working principle

The working principle of a pixel of an SiPM is illustrated in the current-voltage diagram of figure 2.4. Initially, the diode is non-conductive and can be regarded as a capacitor C_d charged at a voltage $V_{bias} > V_{BD}$ (point 0). When an $e-h$ pair is generated, the electron has a probability P_{01} (known as turn-on probability or avalanche triggering probability) to reach the high-field zone and trigger an avalanche. Due to the avalanche, the diode becomes conductive (point 1) with resistance R_d representing the avalanche micro-plasma [43, 44]. The diode capacitor C_d discharges from V_{bias} down to V_{BD} producing an exponentially decreasing current. A quenching circuit is implemented in series, for example a passive serial quench resistor R_Q . The current due to the discharge of C_d flows through R_Q which leads to a voltage drop across C_d . If the current reaches a sufficiently low level, known as the latch current I_{latch} (point 2), the statistical fluctuations reduce the number of carriers in the high-field zone to zero. At this point, the avalanche is quenched (point 3). The probability of such a fluctuation is known as turn-off probability P_{10} . It becomes significant for a current below $10 - 30 \mu A$. This poses a strict constraint on the possible values for R_Q ($\gtrsim 100 k\Omega$) and the operation voltage $V_{bias} - V_{BD}$ (\lesssim few volts). Once the avalanche is terminated, the diode is non-conductive and it recharges to V_{bias} with a characteristic time called the recovery time τ_{rec} (point 0). [45]

Figure 2.5 shows a simplified view of a cross-section of an SiPM pixel. Short wavelength light (blue) is absorbed very close to the surface ($< 1 \mu m$) whereas long wavelength (red) can penetrate deeper. Using a p -on- n structure, the electrons from blue light and the holes from red light drift to the high-field zone. The avalanche triggering probability is higher for electrons than for holes because of a higher ionisation rate. As a result, a device with the p -on- n structure is more sensitive to blue light. The above considerations are inverted for the n -on- p structure which has therefore a higher photon detection efficiency for red light. [46]

An example of the detailed implementation of an SiPM with several GM-APDs connected in parallel is displayed in figure 2.6. In this example, the quench resistors are placed on the side of

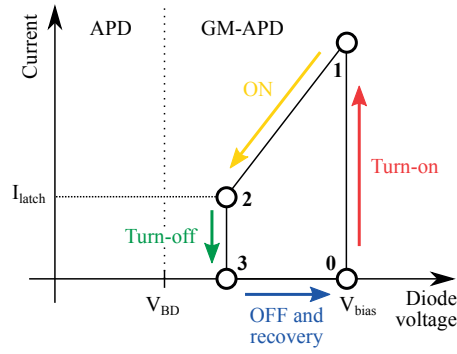


Figure 2.4 – Current-voltage characteristic of an SiPM pixel in discharge.

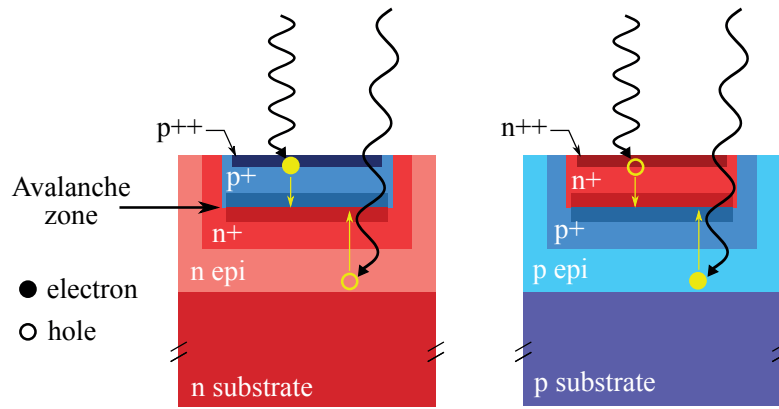


Figure 2.5 – Simplified schematic view of the cross-section of an SiPM pixel. The *p-on-n* structure (left) is preferred for blue light detection while the *n-on-p* structure (right) is better for red light. In actual devices, the substrate is typically 300 μm thickness whereas the epitaxial layer is in the order of 1 μm . Image inspired from [46].

the pixel which reduces the sensitive area. Trenches in the silicon between neighbouring pixels are also present. As it will be discussed later, they enable to reduce pixel-to-pixel cross-talk.

2.3.2 Breakdown voltage

The breakdown voltage is the voltage above which the diode undergoes a self-sustaining avalanche upon the generation of an $e-h$ pair. The relevant voltage of an SiPM is the so-called over-voltage defined as $\Delta V = V_{\text{bias}} - V_{\text{BD}}$. Many SiPM characteristics depend on ΔV rather than V_{bias} . As a consequence, a good knowledge of V_{BD} is crucial. Due to the increase of ionisation rate in silicon at low temperature, V_{BD} decreases when reducing temperature. The dependency is non-linear and follows the prediction calculated in reference [48] for an abrupt $p-n$ junction [49]. In the range from -50°C to room temperature, V_{BD} varies approximately linearly as a function of temperature. The temperature coefficient K_T can be used to calculate V_{BD} at temperature T based on the value at T_0 :

$$V_{\text{BD}}(T) = V_{\text{BD}}(T_0) + K_T \cdot (T - T_0). \quad (2.1)$$

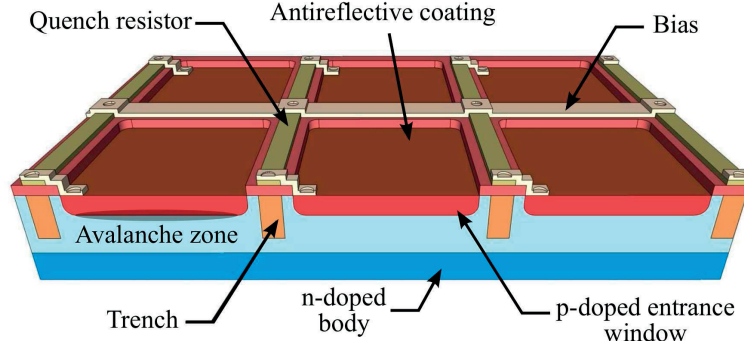


Figure 2.6 – Typical micro-structure implementation of SiPMs. Image from [47].

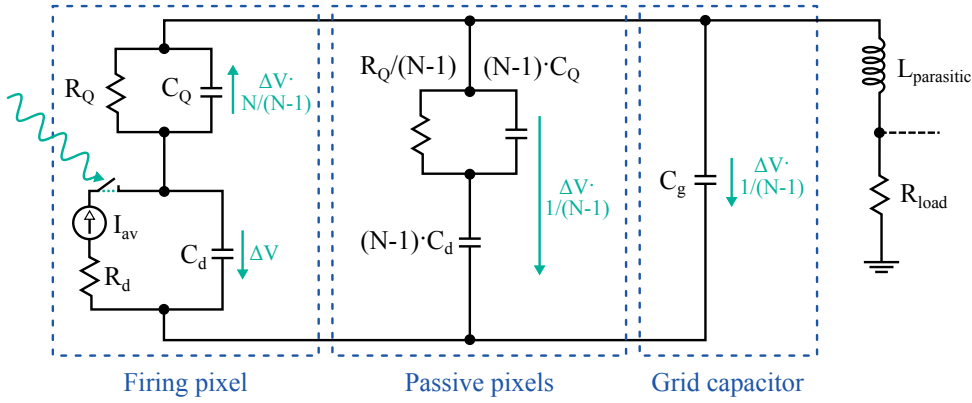


Figure 2.7 – Equivalent circuit of an SiPM with one pixel firing. The charging of the capacitor from the avalanche current is shown in green. Image inspired from [50].

2.3.3 Pulse shape and gain

To model the pulse shape, an equivalent electrical circuit, shown in figure 2.7, can be used [45, 50]. The diode is represented as a capacitor with a junction capacitance C_d in series with R_Q and its parallel capacitor C_Q . The model accounts also for the $N - 1$ inactive pixels as well as the parasitic "grid" capacitance C_g resulting from the connection between the pixels and the terminal. When a photoelectron is generated, the avalanche is modelled by a current source in parallel with C_d and in series with the micro-plasma resistance R_d . The current source delivers a Dirac delta pulse I_{av} with charge Q . C_d and C_Q are charged by currents in opposite directions to a voltage of approximately ΔV . The current through C_Q is divided through the rest of the detector and the load resistance of the read-out electronics R_{load} . It charges C_g and the inactive pixels to $\Delta V/(N - 1)$. The charging time is $\tau_d = R_d \cdot (C_d + C_Q)$ and corresponds to the signal rise time. Once the avalanche is terminated, the switch in the model is open. The capacitors will discharge with a different time constant leading to the falling edge of the pulse. The fast falling component is dominated by the inactive pixels and C_g discharging through R_{load} with decay time $\tau_{short} = R_{load} \cdot C_{tot}$ where $C_{tot} = C_g + N \cdot (C_d + C_Q)$ is the total detector capacitance. In the active pixel, C_d and C_Q are almost completely charged to ΔV and their discharge, going through R_Q , is characterised by a decay time of $\tau_{long} = R_Q \cdot (C_d + C_Q)$. The active pixel has recovered once C_d and C_Q are discharged. The time it takes to recover is therefore equal to the long decay time: $\tau_{rec} = \tau_{long} = R_Q \cdot (C_d + C_Q)$.

Note that the routing line to the read-out electronics can suffer from a parasitic serial inductance $L_{\text{parasitic}}$ which often produces oscillations, called ringing, in the pulse shape. It can be observed after the fast falling edge^b. The pulse shape changes with temperature since R_Q is temperature-dependent. For resistors made of poly-silicon (most of the devices), R_Q decreases with temperature by typically $-2.4 \text{ k}\Omega/^{\circ}\text{C}$ [51].

In the first SiPMs, C_Q was only a parasitic capacitance and the fast component was not present. However, in modern designs, it is an important tunable parameter because it allows for the fast transient pulse. C_Q is adjusted to enhance the fast pulse and suppress the slow component in a controlled manner. This is of particular importance in timing applications.

The charge released by an avalanche is $Q = \Delta V \cdot (C_d + C_Q)$ and therefore the gain is defined as $G = \Delta V \cdot (C_d + C_Q)/e$ where e is the electron charge. $C_d + C_Q$ is dominated by C_d which is proportional to the pixel area and inversely proportional to the avalanche region thickness. $G/\Delta V$, which only depends on the two capacitors, is independent of temperature. The V_{BD} temperature dependence introduced in relation (2.1) gives rise to the following relative gain variation:

$$\frac{\delta G/G}{\delta T} = \frac{\delta V_{\text{BD}}/\Delta V}{\delta T} = \frac{K_T}{\Delta V}. \quad (2.2)$$

Temperature influence can be reduced by high ΔV operation or small K_T . Temperature stabilisation and/or bias voltage compensation are needed to keep the gain and therefore the detector response constant.

We call one *photoelectron* (1 PE) the mean amplitude (charge or voltage on R_{load}) of a single pixel discharge. In the following, we will express the signals in units of 1 PE.

2.3.4 Dark count rate

Dark counts are random pulses caused by charge carrier pairs thermally generated in the depleted region of the diode. The free charge carriers undergo amplification and produce an avalanche indistinguishable from the one induced by a converted photon. The thermal generation of free e - h pairs can be due to several mechanisms illustrated in the band diagram of figure 2.8. At room temperature, the e - h pairs are produced by lattice defects and impurities where the presence of an intermediate energy level in the band gap enhances the probability to reach the conduction band. This mechanism is called the Shockley-Read-Hall process. In the avalanche zone, the high electric field deforms the band structure. Free charge carriers can be produced by direct band-to-band tunnelling. This mechanism becomes dominant at temperatures below 200 K. [49]

Dark count rate (DCR) is proportional to the active area and increases with temperature. For applications requiring very low noise, cooling is an effective means. DCR is measured by the frequency of random pulses exceeding a threshold of 0.5 PE in the dark and is denoted f_{DCR} . Concerning the temperature dependence above 200 K, it can be well described by a single

^b See figures 4.1 or 4.5a for the pulse shape of the LHCb SciFi tracker SiPM with visible ringing.

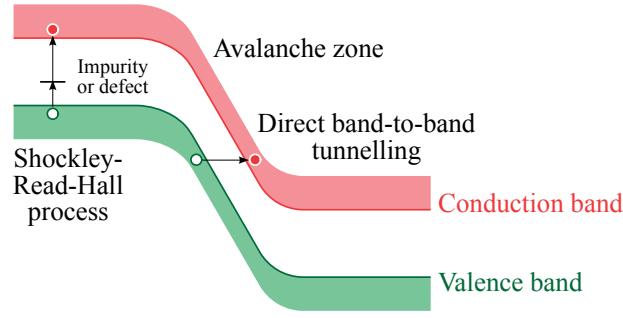


Figure 2.8 – Generation of free charge carriers depicted in a simplified band diagram of the avalanche zone.

exponential as:

$$\frac{f_{\text{DCR}}(T)}{f_{\text{DCR}}(T_0)} = 2^{(T-T_0)/T_{1/2}}, \quad (2.3)$$

where T_0 is a reference temperature and $T_{1/2}$ is the temperature difference for which DCR doubles. With small $T_{1/2}$, cooling is more effective to reduce DCR. The value of $T_{1/2}$ depends on the SiPM technology and is typically 8°C [31, 52]. DCR also increases with ΔV due to the dependence on the avalanche triggering probability P_{01} .

2.3.5 Photon detection efficiency

The PDE of SiPMs can be factorised as:

$$\text{PDE} = \text{QE} \cdot \varepsilon_{\text{geometry}} \cdot P_{01}. \quad (2.4)$$

The quantum efficiency QE is the probability that the photon penetrates into the silicon and produces an e - h pair in the depleted region. The term $\varepsilon_{\text{geometry}}$ is the geometrical fill factor defined as the ratio of the active to the total area. One can see in figure 2.6 that the space needed between the pixels for connections, quench resistor and trenches restrain the achievable fill factor. The dead space is independent of the pixel size and therefore $\varepsilon_{\text{geometry}}$ increases with pixel size. It can be as high as 70% [53] with 50 μm pixels. To gain space, Hamamatsu has implemented the quench resistor by a thin metal film (instead of poly-silicon) placed in the active area reaching transmittance above 80% for wavelengths $\lambda > 300 \text{ nm}$ [51]. Metal quench resistors have also the advantage of a reduced temperature dependence with respect to poly-silicon (typically -0.5 and $-2.4 \text{ k}\Omega/\text{C}$, respectively). Another solution to break the fill factor limit is to illuminate a fully depleted device from its backside, the routing lines and R_Q being on the front side [54]. The photoelectrons, produced close to the surface, drift through the depleted volume to the cathode situated on the other side. The electric field is shaped to guide the photoelectrons to the centre of the pixel where the multiplication zone is implemented. This allows to reduce cross-talk between microcells (cross-talk is explained in the next section). Nevertheless, the cross-talk remains large in back illuminated SiPMs unless they are operated at low gain. Finally, P_{01} is the probability that the generated charge carriers initiate an avalanche. It is larger for electrons than for holes because they have a

higher ionisation rate. As explained before, SiPMs are of type *n-on-p* with thick depletion layer for red/green light detection and *p-on-n* for blue light. [24]

The wavelength dependence of the PDE is due to the QE and, to a smaller extent, to P_{01} since the probability that the photoelectron reaches the avalanche zone depends on the photon absorption depth. Given that P_{01} is strongly affected by the electric field, the PDE changes with ΔV . It grows asymptotically and reaches a plateau at high ΔV because of the saturation of charge carrier ionisation rates at high electric field. Changes in PDE with temperature are also observed [49]. This can be related to the factor P_{01} through the changes in photon absorption depth, carrier mobility and, at very low temperature, the onset of carrier freeze-out.

Inefficiency due to the recovery time of the pixels can influence the PDE. During the recovery time ($\tau_{\text{rec}} \sim 100$ ns), the over-voltage on the pixel increases from zero to the nominal value. The pixel suffers therefore from a low P_{01} . For devices with large pixels (long recovery time and high DCR per microcell), this effect can be important.

Under illumination by pulsed light, the SiPM sensitivity is affected by the finite number of pixels and its resulting saturation. With N_γ incident photons and N_{pixels} number of pixels, the saturation is caused by several photons hitting simultaneously the same pixel and can be described by:

$$N_{\text{fired pixels}} = N_{\text{pixels}} \cdot (1 - e^{-\text{PDE} \cdot N_\gamma / N_{\text{pixels}}}), \quad (2.5)$$

where $N_{\text{fired pixels}}$ is the number of fired microcells. This is of particular importance in calorimeter applications where a wide dynamic range with linear response is required.

2.3.6 Correlated noise

Related to a primary avalanche, either photo-generated or thermally generated, correlated subsequent avalanches are called correlated noise. We distinguish three categories, each related to the different origins:

Direct optical pixel-to-pixel cross-talk (DiXT): Luminescent photons are emitted in the avalanche multiplication process with an efficiency of $3 \cdot 10^{-5}$ photons (mostly in the infrared) per carrier crossing the junction [55]. For large gain devices (large pixels), a significant number of photons (~ 100) can be generated and reach the depleted region of neighbouring pixels. Upon creation of an *e-h* pair, they can subsequently initiate a secondary avalanche. This phenomenon is called optical pixel-to-pixel cross-talk (denoted DiXT in the following) and results in pulses produced simultaneously (or with small time delay of a few 100 ps) with respect to the primary avalanche. The DiXT can be approximated by a linear function of the gain ($G \propto \Delta V$). In addition, it depends on P_{01} introducing a non-linear dependency on ΔV . Temperature dependency has not been observed [49]. For large gain devices, trenches around the pixel active area, filled with opaque material, can be implemented to reduce optical cross-talk. However, cross-talks due to photons reflected at the interface between the high-field region and the substrate or the entrance window are still present. For the optimisation of a device, one

can choose between small pixels and trenches where both solution result in a limited achievable fill factor and therefore PDE.

Delayed pixel-to-pixel cross-talk (DeXT): Cross-talk is also observed with significant delay compared to DiXT. This phenomenon can be explained by avalanche photons absorbed deep in the substrate of the neighbouring pixels [56]. The released electron diffuses out of the substrate before drifting to the amplification zone. The secondary pulses are significantly delayed in time (order of 20 ns).

After-pulse (AP): In a pixel undergoing an avalanche, charge carriers can be trapped at impurities or lattice defects in the active layer and released with some delay or undergo the same process described as DeXT. In both cases, the carriers can initiate a secondary avalanche within the same pixel and create a so-called after-pulse (denoted AP). The AP has typically lower charge than the primary pulse depending on the recovery state of the pixel. Measurements show that AP is constant with temperature down to ~ 100 K taking into account the temperature dependency of R_Q . Below 100 K the probability of AP rises, probably due to new traps becoming active [49]. The AP probability depends on the trap capture probability as well as P_{01} and shows, as a result, a $(\Delta V)^2$ dependence.

Effect of correlated noise Due to correlated noise, dark noise pulses can reach values well above 1 PE. As a consequence, high thresholds are required for noise discrimination. Since correlated noise strongly depends on ΔV , it is the limiting factor for the operation range and hence the achievable PDE.

Statistical model of optical cross-talk generation In a simple model of the generation mechanism of optical cross-talk (DiXT and DeXT) [57], the primary avalanche produces a Poisson distributed random number of new avalanches in neighbouring pixels. These secondary avalanches can in turn fire new pixels, following the same Poisson distribution. This is called a branching Poissonian process. The cross-talk generation cascade stops (after a random number of steps) if the mean of the Poisson distribution is smaller than 1 [58]. After a pixel fired, the total number of produced cross-talks n follows the Borel distribution [57]^c:

$$P_{\text{Borel}}(n) = \frac{[\lambda \cdot (n+1)]^n \cdot e^{-(n+1) \cdot \lambda}}{(n+1)!}, \quad (2.6)$$

where λ is the Borel distribution parameter. This model will be needed for the interpretation of the measurements of gain and photon detection efficiency presented in the next chapter.

2.3.7 Radiation damage

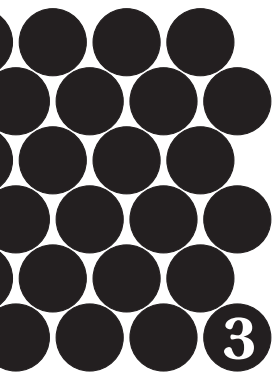
At the microscopic level, the damage caused by radiation in SiPMs is the same as in standard silicon junctions and is due to ionising and non-ionising interactions. The result is the displacement of atoms out of the lattice site (point defects) and large disordered regions. The radiation damage is proportional to the fluence and depends on particle type and energy. The *non-ionising energy-loss hypothesis* (NIEL), which assumes that any radiation effect scales

^c The expression is slightly modified with respect to reference [57]. n represents here the number of cross-talks, as opposed to the parameter k in [57] that represents the total number of microcells that fired ($k = n + 1$).

linearly with the energy imparted in displacing interactions, allows to compare the radiation damage caused by different particle types and energies [59]. In this work, the irradiation fluence unit used is the equivalent fluence of 1 MeV neutrons ($1 \text{ MeV n}_{\text{eq}}/\text{cm}^2$).

Defects in the silicon lattice introduce new generation centres for thermal charge carriers. In SiPMs, this leads to a radiation damage induced DCR which is proportional to the fluence. This type of DCR can be reduced by cooling with a characteristic coefficient $T_{1/2}^{\text{rad}}$ that is in general larger than the $T_{1/2}$ for the DCR described in section 2.3.4. It has been observed that SiPMs with higher V_{BD} have smaller $T_{1/2}^{\text{rad}}$ [60]. At high irradiation fluence ($\sim 10^{14} \text{ 1 MeV n}_{\text{eq}}/\text{cm}^2$), in addition to the DCR increase, change in V_{BD} and reduction in gain and PDE were also observed. Extremely high DCR will eventually saturate the SiPM and the recovery time will reduce the overall sensitivity. This effect can be mitigated by small pixel size [61]. The rate of after-pulses is expected to increase after irradiation due to the introduction of additional traps whereas optical cross-talk is expected to be constant.

Some of the defects introduced in silicon are mobile and can gather at impurities or form larger stable defect complexes. They can also annihilate with their counterpart (for example a recoil atom with a vacancy) decreasing in this way the defect concentration. Therefore, some of the radiation damage can be recovered by annealing, namely heating for a certain time. [59]



3 LHCb scintillating fibre tracker

The SciFi tracker measures the trajectory of charged particles in the LHCb detector downstream of the magnet. This chapter starts with a description of the SciFi technology and its working principle and continues with a short summary of various aspects of the design of the SciFi tracker. The precise characterisation of long fibre modules was performed with test beams and is presented in appendix A.

3.1 The SciFi technology

Scintillating fibres have been used for applications in high energy physics since the 1980's. The technology combines fast scintillators and fine granularity achievable by plastic fibres. It enables the design of fast and low mass detectors with the possibility to adapt shape and size. In the last decade, the introduction of SiPMs for the light detection has boosted the interest and the potential applications. The technology has reached the maturity for implementation in the environment of LHC experiments with the requirements on the read-out rate, the fine granularity, the large scale and the harsh radiation environment. [62]

3.1.1 Scintillating fibres

The role of the fibre is two-fold. It produces the scintillation light from the energy deposition of a charged particle and transports the signal to the photosensor. The amount of light produced is the dominant characteristic defining the hit detection efficiency. In a plane made of a single layer of fibres, the light intensity is proportional to the particle path length in the fibre and therefore to the fibre diameter. In a first approximation, the spatial resolution is given by the pitch between fibres divided by $\sqrt{12}$. In order to obtain a sufficient signal and preserve a fine granularity, the SciFi tracker uses a multilayer staggered arrangement of fibres (see figure 3.3). The resolution is improved beyond the $\sqrt{12}$ -limit by choosing the fibre diameter equal to the channel width.

The fibre chosen for LHCb is the SCSF-78MJ blue emitting double cladded plastic fibre (250 μm diameter) from Kuraray^a. It is the only fibre available that combines a sufficiently fast light

^a Kuraray Co. Ltd., Ote Center Building, 1-1-3, Otemachi, Chiyoda-ku, Tokyo 100-8115, Japan.

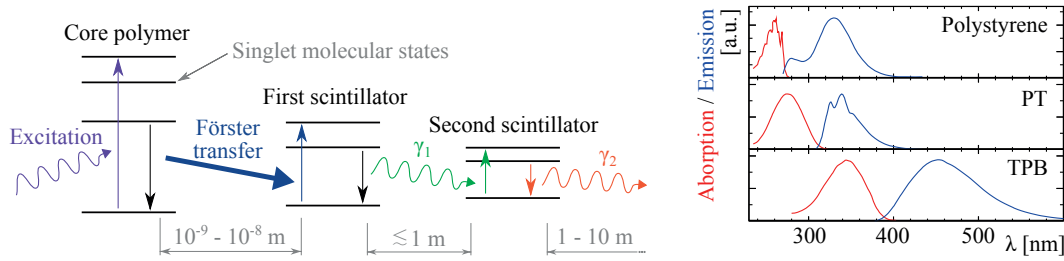


Figure 3.1 – Electronic transitions leading to the emission of scintillation light in a fibre (left). Absorption (logarithmic scale) and emission spectra of the fibre compounds (right). Right image from [65, 66].

emission with a high scintillation yield and low attenuation. It is composed of a core polymer (polystyrene) doped with a primary scintillator (p-terphenyl PT, $\sim 0.10\%$ by weight) and a wavelength shifter (tetraphenyl-butadiene TPB, $\sim 0.05\%$ by weight). The scintillation light is generated through a multistep process illustrated in figure 3.1. The ionisation energy is absorbed by the core polymer molecules [63]. Polystyrene has a high efficiency for the transfer of absorbed energy to the primary scintillator. The concentration of the primary scintillator molecules is optimised such that the energy is transferred through local non-radiative dipole-dipole transmission which is called Förster transfer. The efficiency of this particular type of energy exchange drops as the distance between the resonating molecules increases. The primary scintillator releases subsequently the excitation energy in the form of photons within a short time ($\lesssim 1$ ns). The large Stokes shift prevents the direct re-absorption of emitted photons. The emitted photons are in a wavelength region where polystyrene has poor transmission properties. The second scintillator is a wavelength shifter with an emission spectrum peaking in the blue where the fibre is more transparent. The overall time spread of the created photons depends on the relaxation decay time of the primary scintillator and of the wavelength shifter (the Förster transfer is much faster). The characteristic time of emission for the SCSF-78MJ, 2.8 ns, is dominated by the relaxation time of the TPB. Note that an R&D has also been carried out for fibres with faster scintillator based on covalent bonding of the activator and the wavelength shifter (so-called NOL fibres) [64]. These fibres have not been considered for the final design of the LHCb SciFi tracker due to the lower light yield. However, even at this early stage of the R&D, they are already competitive for applications requiring time information. [10, 62]

Scintillation light is emitted with random directions inside the fibre. Only a fraction is trapped in the fibre by total internal reflection. As shown in figure 3.2, the light capture is improved by using two cladding layers with decreasing refractive index. The fibres in the mats are glued together with an epoxy-based glue with refractive index of 1.53. Thus, no internal reflection occurs at the interface between the second cladding and the glue. Overall, 10.7% of the light is trapped inside the fibre [68]. The light propagation operates via different modes. On average, the propagation time is 6 ns/m and results from the different path lengths inside the fibre. Helical modes are strongly suppressed due to the many internal reflections and the long path. The light output as a function of the distance from the source can be described by the sum of two exponential functions modelling the short attenuation of the helical modes and the

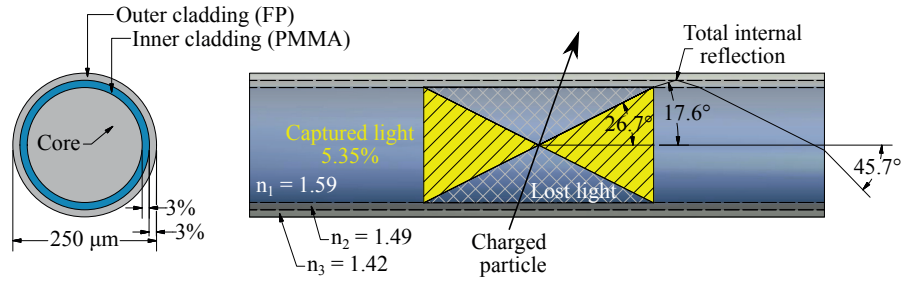


Figure 3.2 – Scintillating fibre schematics. The light is trapped and propagates within the fibre through total internal reflection. Image from [67].

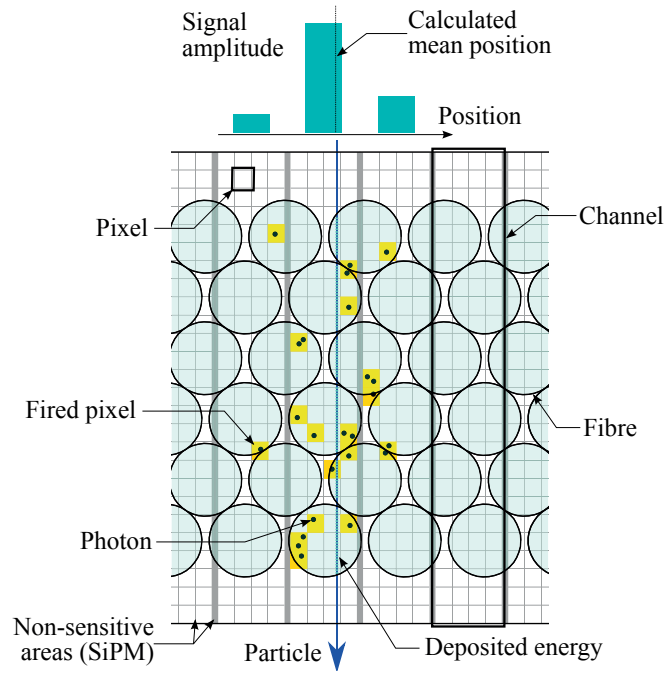


Figure 3.3 – Illustration of the signal formation of a particle crossing the fibre mat and its detection in the photodetector. This example is taken from a simulation of the LHCb SciFi tracker.

longer attenuation of straight paths. For the SCSF-78MJ, the characteristic distance of the short and the long attenuation component are 0.1 and 3.3 m, respectively. As shown in the bottom right plot of figure 3.1 (TPB), the emission spectrum ranges from 400 to 600 nm with a peak at 450 nm. [10]

3.1.2 Working principle and clustering

The signal generation in the SciFi tracker is illustrated in figure 3.3. A particle crossing the fibre mat produces scintillation from the energy deposited in the fibres core. The light captured is transported to the fibre end where the read-out is done by sections of 250 µm width using a multichannel photosensor based on silicon photomultipliers. Due to the staggered geometry, the signal from a single particle at normal incidence is typically spread over two to three channels and can be increased for other incident angles. In reality, we observe larger spread

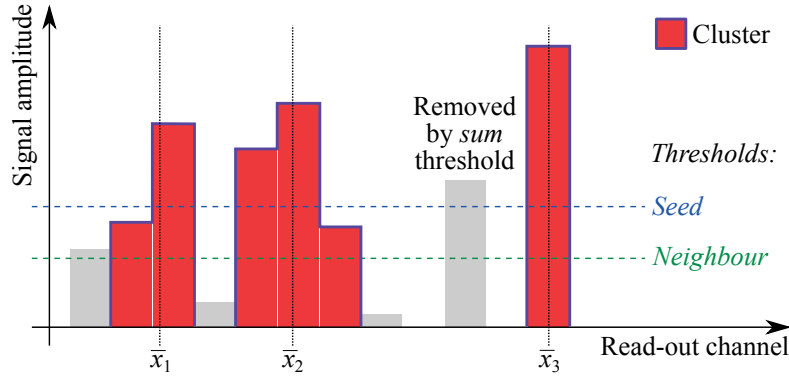


Figure 3.4 – Illustration of the clustering algorithm.

with respect to the geometrical expectation due to cross-talk between adjacent fibres^b and large exit angle of the photons from the fibres^c. The crossing position of the particle is estimated by the centre-of-gravity of the signals over all affected channels.

The radiation environment in the LHCb SciFi tracker induces a drastic increase of DCR in the photodetector. Noise hits from the DCR must be avoided for fast pattern recognition and track finding. The rate of noise hits can be reduced by the optimisation of the three following parameters. The SiPM can be cooled, the time window for signal collection (called the integration time window) is minimised and the signal can be discriminated from the noise using a threshold-based algorithm. This algorithm is called the clustering and is illustrated in figure 3.4. It combines neighbouring channels and forms units called clusters. It comprises the three following steps [72]:

- 1 Identify channels with signal above a *seed threshold* (seed channels).
- 2 Identify channels with signal above a *neighbour threshold* (neighbour channels).
- 3 Form clusters from adjacent seed channels and, at maximum, one neighbour channel on the left and one on the right. Finally, accept the cluster if the total signal inside the cluster (called the cluster sum) exceeds the *sum threshold*.

Typical thresholds used in the SciFi tracker to suppress the noise from irradiated SiPMs are *seed/neigh/sum* = 2.5/1.5/4.5 PE. The thresholds have a strong influence on the hit detection efficiency and noise rejection. The rate of clusters due to noise for a 128-channel SiPM array, called the *noise cluster rate* (NCR), is typically 100 times lower than the DCR. Sources of noise clusters are the SiPM correlated noise and, at very high DCR, the overlap of DCR pulses in the integration time window.

The mean cluster position \bar{x} , calculated as the average of the channel positions x weighted by

^b Simulation studies show that the main contribution to fibre cross-talk comes from UV photons emitted by the primary scintillator (PT) and absorbed by the wavelength shifter (TPB) in another fibre. [69, 70].

^c Most of the light from a fibre is emitted in the form of a cone with approximately 40° opening angle [71]. Since the SiPM entrance window includes a 100 µm epoxy layer, the light can travel laterally by roughly half a channel.

their signal amplitude s , gives the estimation of the hit position:

$$\bar{x} = \frac{\sum x(i) \cdot s(i)}{\sum s(i)} \quad \text{for channels } i \text{ in the cluster.} \quad (3.1)$$

Note that, in the LHCb SciFi tracker, a modified algorithm is used for a simpler implementation in the read-out electronics. More details will be given in section 3.2.3.

3.1.3 Light yield

For a thin layer of matter^d, the deposited energy by a charged particle follows a Landau distribution. In a first approximation, the number of photons detected by the SiPM (cluster sum) is proportional to the deposited energy. In reality, it is affected by the following aspects:

Low signal: A convolution with a Poisson distribution arises due to the small number of photons and the associated statistical fluctuations (scintillation, transmission, attenuation and detection).

Geometrical aspects: The non-homogeneous cross-section of a fibre mat leads to different path lengths inside the fibres depending on the injection point and incident angle.

Clustering: If the average number of photons is close to the threshold values (*seed* and *neighbour*), a significant fraction of the cluster sum can be lost at the edge due to the cuts. This shifts the distribution towards smaller values. The *sum* threshold introduces a minimum cutoff.

SiPM noise: Random dark noise pulses occurring during the integration time and correlated noise contribute to the cluster sum. The contribution of the random noise depends on the DCR and the integration time and can be significant, especially in irradiated SiPMs. The input from direct cross-talk can be obtained from the cross-talk probability. The contribution from delayed correlated noise depends on the probability and the integration time.

SiPM pixel saturation: High signals in the distribution are affected by pixel saturation, as described in equation (2.5) in the previous chapter.

Electronics non-linearity: The electronics used for the measurement can have non-linear response or show saturation effects.

Figure 3.5 presents the typical cluster sum distribution obtained for a short mat (30 cm long fibres) with five layers of fibres. The *light yield* is an important figure-of-merit defined as the most probable value (MPV) of the distribution and found by fitting the peak region with a Gaussian function. It is the dominating characteristic for the tracking performance of the SciFi technology. Inefficiencies (lost signal clusters) are due to low cluster sum rejected by the algorithm. The tail in the small signal region of the cluster sum distribution allows to estimate the number of lost clusters. As shown in the figure, one way to increase the light yield and therefore the detection efficiency is to operate the photodetector at higher

^d A SciFi detection plane has a thickness in the order of 1% of a radiation length and can be regarded as a thin layer of matter in this discussion.

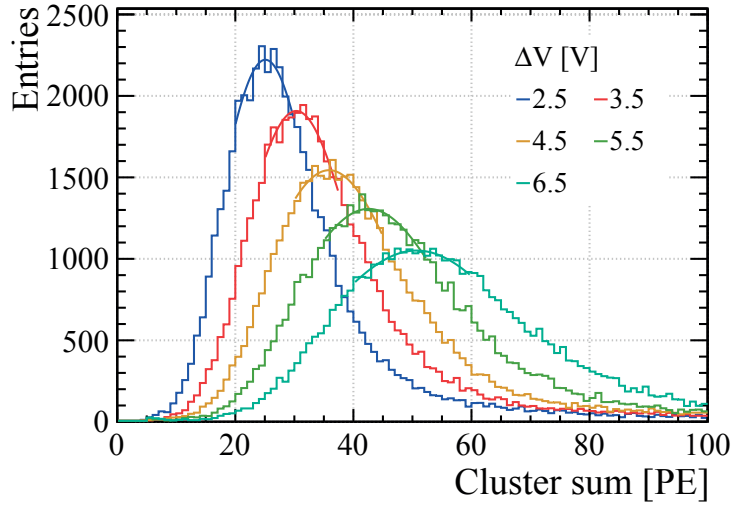


Figure 3.5 – Light yield of a short fibre mat (30 cm) measured at different SiPM bias voltages and with VATA64 electronics. More details on the measurement method will be given in chapter 5.

over-voltage with the consequence to increase the noise cluster rate at the same time. This consideration illustrates one of the most challenging aspects of the SciFi technology: finding the best compromise between hit detection efficiency and noise cluster rate. The optimisation parameters which can be adjusted are: the design of the fibre mats (e.g. number of fibre layers), the SiPM technology and the threshold settings for the clustering.

For the LHCb SciFi tracker, the number of fibre layers is limited to six in order to minimise multiple scattering. Most of the particles traverse the detector in the central region close to the beam pipe far from the photodetector read-out. A mirror is placed to increase the light yield and ensure high detection efficiency. The gain from the mirror is approximately 75% for particles crossing at the mirror end (80% mirror reflectivity minus 5% Fresnel reflection already present without mirror) [73]. The disadvantage is an additional lateral dispersion of the light and the spread of the photons' arrival time (especially for particles far from the mirror) that can lead to spillover effects. The performance of fibre modules for the LHCb SciFi tracker is discussed in appendix A.

3.2 Detector design and fabrication

The SciFi covers a total active area of 320 m^2 and is composed of independent modules. The large size, the mechanical stability and the precision positioning are in contradiction with the low mass requirement. The detector is a complicated system including SiPM cooling, precision alignment, modular design and electronics read-out. A large fraction of the manufacturing steps require custom solutions.

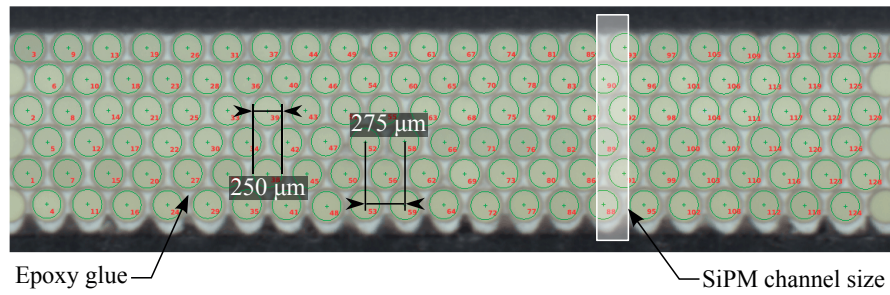


Figure 3.6 – Cross-section of a fibre mat. The fibres' position and diameter is measured by a quality control software (green circles) in order to detect defects. An SiPM channel is drawn at the same scale. The pitch between fibres is 275 μm . Image from [75].

3.2.1 Fibre module fabrication

Each fibre mat covers an area of $0.13 \times 2.40 \text{ m}^2$ and has an active thickness of 1.35 mm (1.6 mm including the epoxy glue on top and bottom). Eight mats are assembled to a module of dimension $0.53 \times 4.85 \text{ m}^2$. The fabrication is shared between the participating institutes of the project and comprises three main steps which are shortly described in the following.

Fibre quality assurance After a tendering process in 2015, a contract was signed with Kuraray for the procurement of 12'500 km of fibres and the delivery was completed in 2017. A quality assurance process has been performed at CERN. The procedure comprises the verification of the fibre performance as attenuation length, scintillation light yield and, for a small sample, radiation damage studies. A scan of the fibre diameter was performed using a custom-made scanner and large diameter fluctuations were automatically shrunk by a heat and pull process. [68, 67]

Mat winding The qualified fibres are distributed to four institutes (RWTH Aachen University, TU Dortmund, EPFL Lausanne and Kurchatov Institute Moscow) for the fabrication of mats. Approximately 1000 are needed to equip the full SciFi tracker. A custom machine was developed to wind the fibre onto a threaded wheel with sufficient precision allowing to stack many staggered layers. The layers are fixed together during the winding with a TiO_2 -loaded^e epoxy glue. The mats are then unformed from the wheel, a polycarbonate precision piece is glued to each end, a thin Kapton foil is laminated onto the mat for mechanical stabilisation and light tightness, the two ends are cut to obtain a clear optical interface and a mirror is glued at one end. For the quality assurance, an optical scan is performed, as displayed in figure 3.6. The software allows to measure the fibres' diameter and position with respect to reference points on the end-piece and ensure the alignment with the photodetector. The final check is a light yield scan performed with a ^{90}Sr source. [67, 74]

Module assembly The 128 modules are assembled in two institutes (Rupert-Karls University Heidelberg and NIKHEF Amsterdam). The mats are aligned using precision pins incorporated during the winding process and, to make a module, eight mats are sandwiched between two panels made of 20 mm thick honeycomb and carbon fibre sheets. The ends of the module are

^e This additive allows to reduce optical cross-talk between adjacent fibres and to diffuse part of the escaping light back into the fibre.

rigidified with metallic endplugs containing also a light injection system for calibration of the photodetectors. Special modules with the beam-pipe cut-out are also fabricated. [67]

3.2.2 Silicon photomultiplier multichannel array

The customisation of SiPMs from Hamamatsu^f for applications with scintillating fibres started in 2011 in the context of a balloon-borne experiment named PEBS [76, 77] and continued through 2018. From 2013, KETEK^g has also produced prototypes for the SciFi tracker and several devices from both manufacturers were evaluated. The detector from Hamamatsu was selected to equip the SciFi tracker and 5500 multichannel arrays were ordered (3840 needed).

Packaging The SiPM package delivered by Hamamatsu is displayed in figure 3.7. The multichannel array has a total active area of $32.540 \times 1.625 \text{ mm}^2$. The package is made of two silicon dies (64 channels each) mounted on a common PCB. The channel is $230 \mu\text{m}$ active width ($250 \mu\text{m}$ pitch between channels) and contain 104 pixels of size $57.5 \times 62.5 \mu\text{m}^2$. The quench resistors are implemented by transparent thin metal films put on top of the pixels. Non-sensitive areas in the package include a $220 \mu\text{m}$ gap between the two dies and a $160 \mu\text{m}$ gap at each side. The optical window and the bond wires are protected with a $105 \mu\text{m}$ thick epoxy layer. The large pixels were chosen to optimise the fill factor. To mitigate the relatively large resultant optical cross-talk, isolation trenches are implemented between pixels.

The SiPM array is soldered on a Kapton flex PCB. This manufacturing step is subcontracted to three different companies: Cicor^h (flex PCB and stiffener manufacturing), PacTechⁱ (SiPM laser balling) and Valtronic^j (component assembly, inspection and testing). The flex cable allows to bias the two silicon dies separately and route the signals out from the SiPM located in the cooling system to the front-end electronics. The flex is made of three copper layers (one for the ground plane and two for signals). Its low heat conductivity allows to minimise the cooling power needed for the SiPM operation and to avoid condensation outside the cooling enclosure. On the backside of the flex close to the SiPM, an AlN^k stiffener is glued which ensures rigidity and high heat conductivity. A Pt1000 sensor is also soldered on the backside to monitor the temperature with a precision of $\pm 1^\circ\text{C}$. Capacitive coupling between neighbouring signal lines on the flex results in a negative cross-talk between closest even or odd channels of approximately 8%.

Serial production and quality assurance Throughout the production phase, the SiPM and flex assembly undergoes several inspections and quality assurance tests. Upon delivery from Hamamatsu, the photodetectors are optically inspected using a microscope. This procedure has two objectives: the rejection of samples with defects on the optical surface or in the epoxy entrance window and the cleaning of the optical surface in case needed. A small fraction (0.4%)

^f Hamamatsu Photonics K.K., 325-6, Sunayama-cho, Naka-ku, Hamamatsu City, Shizuoka Pref., 430-8587, Japan.

^g KETEK GmbH, Hofer Str. 3, 81737 München, Germany.

^h Cicorel SA, Route de l'Europe 8, 2017 Boudry, Switzerland.

ⁱ Pac Tech – Packaging Technologies GmbH, Am Schlangenhurst 7 – 9, 14641 Nauen, Germany.

^j Valtronic Technologies (Suisse) SA, Route de Bonport 2, 1343 Les Charbonnières, Switzerland.

^k This material has approximately the same thermal expansion coefficient as silicon.

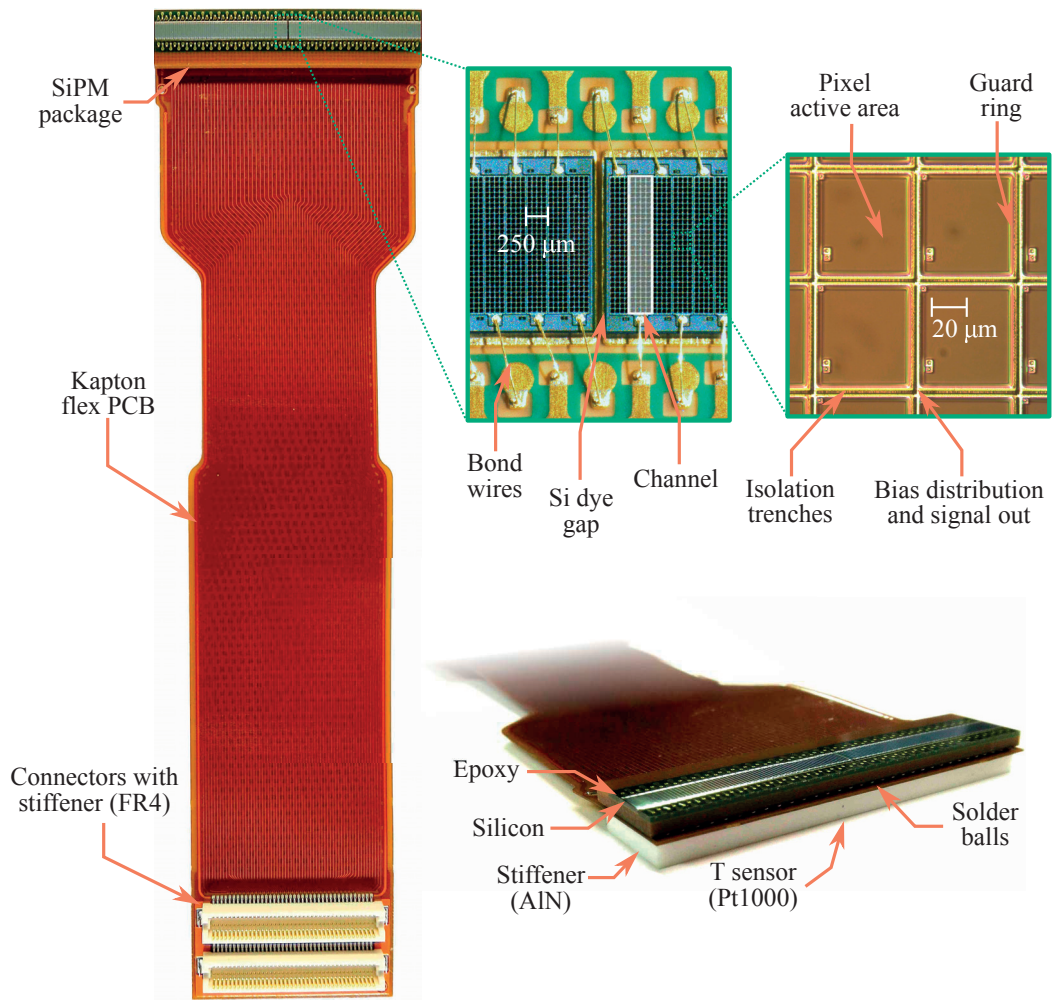


Figure 3.7 – Pictures of the SiPM array package. Photodetector assembled on a flex PCB (left). Zoom on the active area close to the gap between two silicon dies (top middle) and on the pixels (top right). Side view of the SiPM mounted on the flex (bottom right).

of the detectors (called QA samples) are randomly selected for complete characterisation (correlated noise, PDE, R_Q , DCR).

At Valtronic, all devices (SiPM+flex assembly) are temperature cycled (three cycles -40 to 80°C) to provoke early failure. This is followed by optical and electrical inspections. The latter consists in detecting disconnected or shorted channels by measuring the forward bias current and comparing with the value expected from the quench resistance. At this point, the connectivity of the temperature sensor is also tested.

To assure the quality of the device at the end of the production line and a smooth integration into the SciFi tracker, a final series of tests is performed at EPFL. At the integration in the electronic and cooling systems, four photodetectors are glued on a cooling pipe and connected to one bias voltage supply. Therefore, groups of four arrays are formed according to the total thickness and the breakdown voltage. Adjacent SiPMs on the cooling pipe with the same total thickness ensure a good optical interface (without air gap) with the fibres. The thickness is measured using a microscope by focal point adjustment without any mechanical contact. The

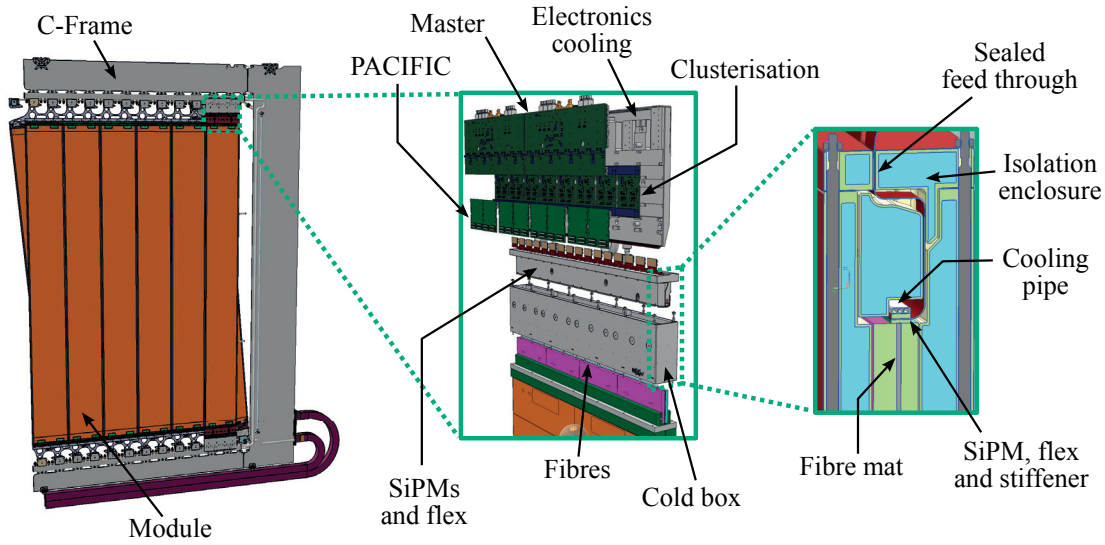


Figure 3.8 – Schematic views of the SciFi tracker modules. Half station mounted on a C-frame (left), read-out electronics, cold-box and module assembly (centre) and cross-section of the cold-box (right). Images from the LHCb SciFi collaboration.

breakdown voltage is measured with a setup based on the method explained in section 5.3 and optimised to test automatically eight arrays (1024 channels) simultaneously in less than 10 minutes. The groups of SiPMs are chosen such that V_{BD} variations are below 0.5 V allowing for an accurate bias voltage compensation at the front-end electronics. Finally, a small sample of the final devices are irradiated and the DCR, NCR and light yield are measured to control the performance after irradiation.

3.2.3 Read-out electronics

The front-end electronics for the read-out of SiPMs is custom-designed to meet the SciFi tracker requirements. It provides a read-out at 40 MHz with short signal integration time. The data transmitted to the LHCb detector back-end electronics is zero-suppressed and only contains the hit position. The clustering explained in section 3.1.2 is used for the zero-suppression. The algorithm is however adapted to the limitations imposed by the fast read-out and data rate. Instead of the condition on the cluster sum, the cluster is accepted either if it contains more than one channel (at least a seed plus a neighbour) or if the single-channel signal is above the *high threshold*. The clusters are also limited in size (four channels maximum) to allow for the most efficient data compression.

A schematic view of the front-end electronics assembly on the SiPM cooling system and the modules is shown in figure 3.8. The electronics is composed of three elements [78]. The PACIFIC ASIC [79] includes a preamplifier, a shaper, an integrator and a digitiser. The conversion from analogue to digital is based on three comparators configured with the neighbour, seed and high threshold, respectively. The output of the comparators is encoded into a 2-bit information as described in table 3.9. One PACIFIC chip processes the data of 64 channels. The fast shaper includes a pole-zero cancellation to filter the slow component of the SiPM pulse. It is tuned to provide a very short output signal (5 ns FWHM) thus minimising the

Table 3.9 – Encoding of the comparators output in the PACIFIC.

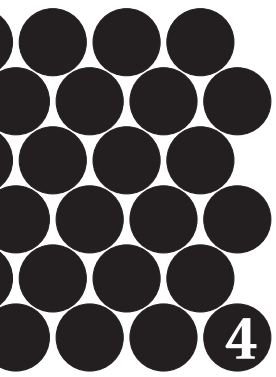
Analogue signal s				Digital output
<i>neigh</i>	>	s		00
<i>seed</i>	>	s	> <i>neigh</i>	01
<i>high</i>	>	s	> <i>seed</i>	10
		s	> <i>high</i>	11

effect of spillover and random pulse overlap. The shaper output is integrated by a dual interleaved gated integrator. It allows to maximise the charge collection while avoiding dead time as one integrator collects the signal and the other can reset. The cluster-finding and zero-suppression is done in the second front-end electronics element called the clusterisation board. It hosts two FPGAs and processes the data of four PACIFIC chips. In the cluster mean position computation of equation (3.1), the signal amplitudes $s(i)$ are replaced by configurable values representing the weight attributed to the channel when the neighbour, seed or high threshold is reached. The weights can be tuned to optimise the resolution. The clusterisation board plays a central role in the data reduction. The algorithm allows to suppress the dark noise from the SiPM while retaining and transmitting the relevant hits from particles. The last element of the front-end electronics is the master board. It provides power and control to the front-end and to the light injection system. It serialises the cluster data and sends it out through gigabit (optical) transmission (GBT) [80].

3.2.4 Cooling and mechanical infrastructures

The SiPMs are operated at -40°C but to benefit from thermal annealing, heating to 30°C during technical stops is foreseen. Given the dimension of the tracker, the cooling system is the result of a complex engineering work done at NIKHEF, Amsterdam, and at CERN. The integration of SiPMs in the cooling system comprises their alignment (based on an optical system) and gluing on a titanium cooling pipe, the mounting in an isolated cold enclosure named the cold-box and finally the assembly on the fibre module. The Ti pipe and the isolation enclosure are 3D-printed. The photodetectors are pushed against the fibres using springs incorporated in the cooling pipe. It was checked that the small movements during the thermal cycles do not damage the optical surface of the fibres and the SiPM. As shown in the right image of figure 3.8, the cold volume is kept very small in order to minimise the surface to the outside. The inside of the cold-box is flushed with nitrogen in order to avoid icing due to humidity. The cooling is based on a liquid circulator (Novec 649 monophase) connected to a chiller via a heat exchanger. The chiller is shared with the VELO and UT cooling systems. To limit heat losses, the distribution pipes are vacuum-insulated.

The fibre modules with their cold-boxes and read-out electronics are mounted on a mechanical support (C-frame) to form a half station (see left image of figure 3.8). To cope with the achievable mounting tolerance of such large objects, a 1 mm-gap between adjacent cold-boxes is foreseen. The reduction in the overall tracking efficiency due to this gap is estimated to be 0.4%. The C-frame is fixed to a rail via carriages so that the tracker can be retracted from the beam-pipe for maintenance. It contains all services as pipes and cables.



4 Silicon photomultiplier characterisation

A detailed and accurate characterisation of SiPMs is required to understand their signal and noise in many applications. The collected information is a valuable feedback in the attempt to improve the device technology. During the R&D phase of the LHCb SciFi tracker, we developed experimental methods for the determination of all important SiPM characteristics. In this chapter, we review the principle of methods and the results obtained for a version of the SiPM used in the SciFi tracker (H2017) including also irradiated devices. To measure pulse shape, correlated noise, gain and photon detection efficiency, we use statistical analyses of waveforms recorded by an oscilloscope. Breakdown voltage, dark count rate and quench resistor are determined from current-voltage (IV) scans.

In the next chapter 5, we describe complementary methods using very different equipment and approach for the characterisation of multichannel arrays. In addition, results from previous versions of SiPMs (H2014, H2015), KETEK prototypes and single-channel devices from other suppliers are shortly summarised in appendix B.

4.1 Experimental methods overview

We have developed two complementary setups for the characterisation of single-channel SiPMs (or one channel of an array). The first one uses a digital oscilloscope and allows to collect the data for the waveform analysis, the gain and the PDE measurements. The data, recorded at different V_{bias} , consists in time-dependent voltage pulses and pulse frequencies. The second setup allows to measure the IV characteristics in forward and reverse direction for the determination of the breakdown voltage, the DCR and the quench resistor value.

The characterisation of SiPMs is performed at constant temperature. Temperature dependent parameters such as f_{DCR} or V_{BD} can be corrected if the measured temperature deviates from the nominal value. For devices with high f_{DCR} (due to irradiation or very large surface), the operation temperature can be lowered in order to reduce the probability of random overlapping dark pulses. Constant temperature operation can be achieved either by stabilising the temperature with a cooling system or by recording all measurements in a short time.

Irradiation studies The radiation effects on SiPM prototypes was measured throughout the R&D phase of the SciFi tracker. Irradiation with neutrons was performed in a nuclear reactor in Ljubljana ^{a b} [81]. The neutron fluence was checked with PIN diodes and the estimated error is 10% [82]. Irradiation with 18 MeV-protons was done in the Bern Swan Cyclotron facility [83] with an estimated error on the dose below 10% [84]. Irradiations were performed at room temperature and without bias voltage on the detectors apart from one test in Bern during which we monitored in real time the current as a function of the received dose. We observe identical radiation damage whether the SiPM is biased or not during irradiation.

Right after irradiation, the SiPM leakage current as a function of the time behaves as a sum of negative exponentials, describing the effect of different defects that anneal with individual temperature-dependent time constants. After four days of annealing at 40°C, the dark current reaches a plateau at a level of about two to three times lower than the initial value. [85]

Except for the PDE measurement, the methods that will be described in the following can be used to characterise irradiated SiPMs. An alternative measurement method for the PDE will be discussed in chapter 5. Due to the large increase in DCR, irradiated detectors must be operated at low temperature for their characterisation. To verify that the high DCR and low temperature operation do not bias the results, we use a non-irradiated reference sample of the same type. This detector is operated in the same conditions and a high frequency of random pulses is injected using a continuous light source, producing similar bias current as for irradiated devices. This procedure allows to distinguish between effects due to radiation damage and effects only related to the high DCR.

4.2 Waveform analysis and correlated noise measurement

The waveform analysis allows to measure the correlated noise probabilities as direct cross-talk, delayed cross-talk and after-pulse as a function of ΔV . It also gives a statistical measurement of the most important time constants of the pulse shape and the noise: long pulse component decay time, recovery time, delayed cross-talk mean lifetime and after-pulse mean lifetime. The results are important ingredients for the optimisation of the SiPM performance in touch with the manufacturers. They are in addition needed for the PDE measurement to introduce precise corrections for correlated noise. The method provides such corrections with high accuracy over a large range of ΔV .

The principle is to acquire on an oscilloscope a large number of triggered dark pulses. Waveforms of $t_{\text{sample}} = 200$ ns duration around the peak of the pulse are recorded (see examples in figure 4.1). The statistical analysis, based on the ROOT analysis framework [86], is performed offline and includes a peak finding algorithm in order to detect and classify pulses produced in correlation with the primary dark pulse.

We developed this method for small size SiPMs with an area of 0.4 mm^2 and $f_{\text{DCR}} < 50 \text{ kHz}$ at room temperature. In this case, f_{DCR} is sufficiently small to have low probability of a

^a The spectral composition of neutrons is 37.9% thermal neutrons ($< 0.625 \text{ eV}$), 29.4% epithermal neutrons (0.625 eV to 0.1 MeV) and 32.7% fast neutrons ($> 0.1 \text{ MeV}$). The total neutron flux is $1.175 \cdot 10^{13} \text{ 1 MeV n}_{\text{eq}}/\text{cm}^2/\text{s}$.

^b We received financial support from the H2020 project AIDA-2020, GA no. 654168.

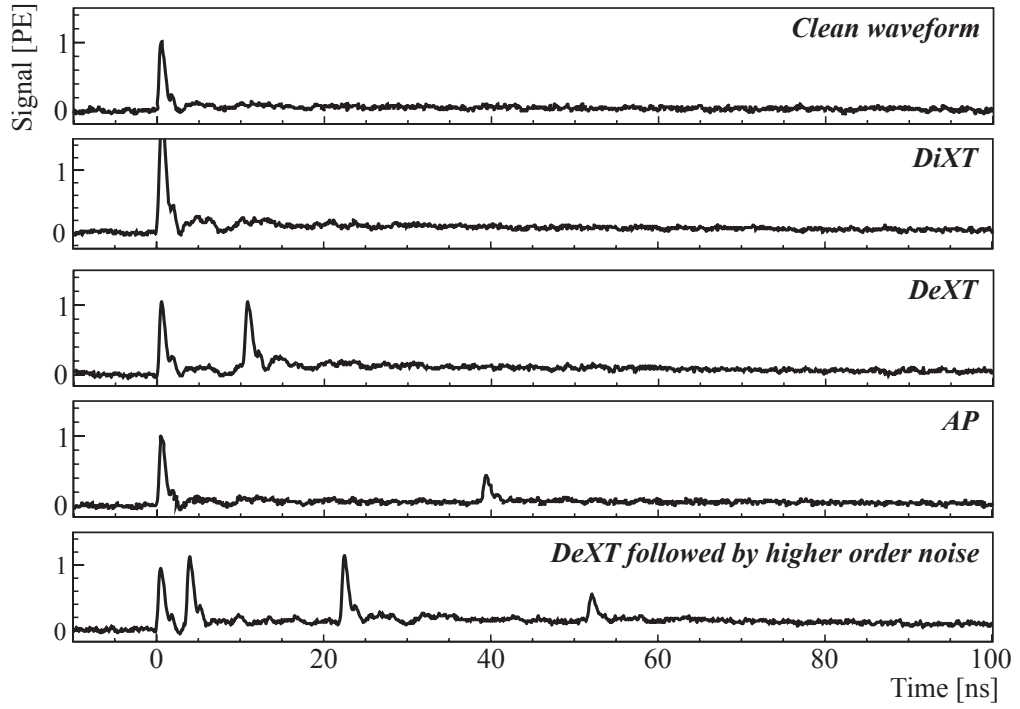


Figure 4.1 – Waveforms recorded with an H2017 detector. The voltage amplitude is scaled with respect to the amplitude of 1 PE pulses. Different types of correlated noise are shown.

second random dark pulse falling in the sampling window ($p_{>1 \text{ dark}} = 200 \text{ ns} / 20 \mu\text{s} = 1\%$). The method can be extended to larger devices with higher f_{DCR} by performing the tests at reduced temperature. Effects introduced by very high random pulse frequency will be discussed with the case of irradiated detectors. Similar methods have been proposed for example in references [87, 88, 89]. After the description of our method and the discussion of the results, we give a short comparison with these other works (see section 4.2.5).

4.2.1 Measurement setup and analysis method

The setup is made of a shielded box to protect the SiPM against electromagnetic interference (EMI) and the detector is read out by a high bandwidth preamplifier (2.5 GHz, 20 or 40 dBV) and a digital 1 GHz oscilloscope (10 GS/s) ^c. The excellent signal-to-noise ratio achieved in this way allows to operate and characterise the detector over a large range of operation voltages without being dominated by the electronic noise. The fast component of the SiPM pulse has typically a rising edge shorter than 1 ns which imposes to the mounting, cabling and read-out system to cope with high speed signals. A low serial inductance is also required to avoid the associated ringing. The bias voltage filtering is provided by a serial 1 k Ω resistor and two parallel ceramic capacitors (100 nF and 1 μF) mounted close to the detector. The setup is equipped with a cooling system which allows to reach -40°C reducing the DCR by typically more than a factor 100 compared to ambient temperature operation. The bias voltage source meter ^d and the oscilloscope are controlled and read using Python routines.

^c Preamplifier: FEMTO, HSA-X-2-20, HSA-X-2-40. Oscilloscope: LeCroy, WAVERUNNER 104MXI

^d Keithley 2400

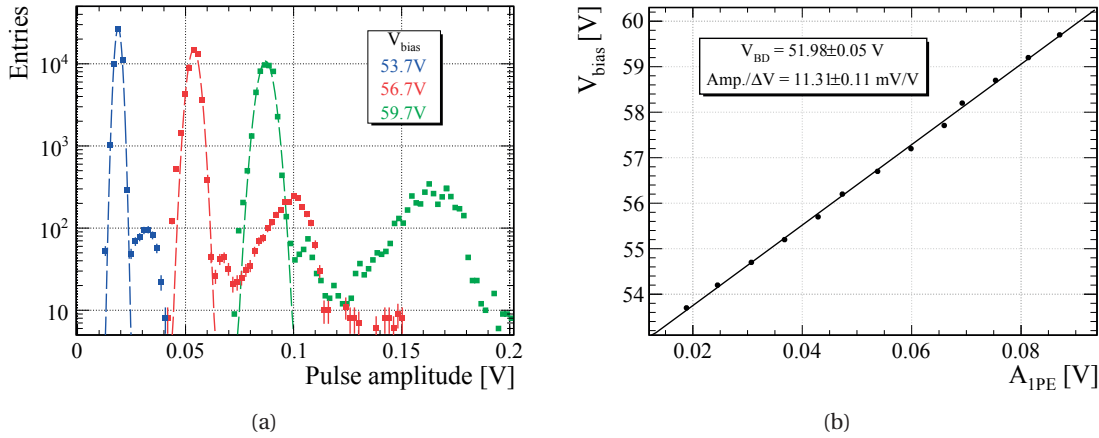


Figure 4.2 – Dark pulse amplitude distribution for three different bias voltages and determination of A_{1PE} using a fit with a Gaussian function (left). Calculation of V_{BD} using the A_{1PE} obtained at different V_{bias} (right).

Breakdown voltage measurement The first step in the analysis of waveforms is the computation of V_{BD} . The procedure is illustrated in figure 4.2. For each V_{bias} , the 1 PE pulse amplitude A_{1PE} is extracted from a Gaussian fit of the amplitude distribution of the dark pulses. The obtained values are fitted with a linear function. Using the assumption $A_{1PE} \propto \Delta V$, V_{BD} is calculated from the extrapolation of the fit function to zero. Since the duration of the measurement is sufficiently short to avoid any temperature changes, the V_{BD} obtained in this way can be used to calculate the ΔV without further temperature compensation. We call V_{BD}^{Amp} the breakdown voltage obtained with this method. Measurements were taken and repeated on several detectors in order to estimate the reproducibility and the uncertainty on V_{BD}^{Amp} . The robustness of the procedure was evaluated by injecting random light on the detector. The increased rate of random pulses does not affect the V_{BD}^{Amp} measurement. The reproducibility is found to be better 5 mV and the uncertainty is below 50 mV.

Instead of the pulse amplitude, one can use the charge computed from a numerical integration of the 1 PE-pulse waveforms. The breakdown voltage found in this way is denoted V_{BD}^{Int} . Comparing a large number of measurements performed on H2017 QA samples, we observe a systematic difference of 400 mV on average between V_{BD}^{Amp} and V_{BD}^{Int} . This offset is linked to the fast pulse component in the V_{BD}^{Amp} measurement. At ΔV lower than 0.3 V, the linearity of A_{1PE} as a function of V_{bias} does not hold. In contrast, the slow pulse component and the pulse charge (dominated by the slow component) is linear over the full range. For the following discussion, V_{BD}^{Int} is used as a reference since it fulfils the relation $G \propto \Delta V$.

Correlated noise classification In the next step of the analysis, an algorithm finds all peaks present in the waveform. The peaks are identified as direct cross-talk, delayed cross-talk or after-pulse using conditions on the time and amplitude. Typical values optimised for the H2017 detectors are 1.17 PE in a time window 0 to 1 ns for DiXT, 0.85 PE with times > 1 ns for DeXT and 0.25 PE with times > 10 ns for AP^e. The 10 ns time window discarded for AP detection is needed to avoid misidentification of the ringing following the fast transient.

^e To compare the AP probability with the manufacturer specification, the threshold should be set to 0.5 PE.

As shown in figure 4.1, each waveform may contain only the triggered dark pulse (clean event), or a single or several correlated noise pulses. Every waveform containing correlated noise peaks is classified as DiXT, DeXT or AP, according to the nature of the first correlated noise peak. If, for a single recorded waveform, more than one correlated noise peak is detected, the additional peaks are counted as *higher order* correlated noise. For a large correlated noise probability, the higher order noise is significant. The probability of correlated noise of the kind X (DiXT, DeXT or AP) is the ratio of the number of classified waveforms (N_X) to the total number of waveforms (N_{ev}): $p_X = N_X / N_{ev}$. In the bottom example of figure 4.1, the waveform is classified as DeXT. The two following pulses (DeXT and AP) are simply classified as higher order noise peaks. In the case of high correlated noise probabilities, the overlap of consecutive pulses can lead to a substantial shift of the baseline. The robustness of the peak-finding algorithm allows however to count the higher order correlated peaks even in extreme cases.

Pulse misidentification and contributions neglected The increasing amplitude of APs can reach the threshold set for DeXT. At this point the pulses are classified as DeXT. This effect is typically small since the occurrence probability of APs decreases exponentially with the time delay. Also, random dark count pulses arriving in the sampling window are accounted as DeXT, since they fulfil the amplitude and time conditions.

For detectors with pronounced fast pulse component, the amplitude of DiXT pulses rarely reaches 2 PE. A small delay of 100 ps is sufficient to reduce significantly the summed amplitude. The detection of multiple DiXT cannot be achieved by an amplitude selection because they rarely add up to a fast component larger than 2 PE. Consequently, a single threshold is used and multiple DiXTs are not differentiated from a single DiXT. The probability p_{DiXT} represents an effective cross-talk probability. It is related to the parameter λ of the Borel distribution introduced in equation (2.6) as:

$$p_{DiXT} = P_{Borel}(n > 0) = 1 - P_{Borel}(n = 0) = 1 - e^{-\lambda}. \quad (4.1)$$

Note that, in principle, multiple cross-talks could be distinguished using the integrated pulse charge.

The amplitude of delayed 1 PE pulses is shifted by the slow component of the primary pulse. Due to this amplitude offset, DeXT pulses can reach amplitudes higher than 1 PE and even exceed the threshold for DiXT detection. To ensure the robustness of the algorithm, DiXTs on delayed pulses are therefore not taken into account. The expected error scales with $p_{DiXT} \cdot (p_{AP} + p_{DeXT})$.

4.2.2 Results for H2017 detectors

The composition of correlated noise for an H2017 detector is shown in figure 4.3a. Significant contributions from all three correlated noise sources (DiXT, DeXT and AP) are seen. Higher order noise represents an important contribution if the total primary correlated noise exceeds 20%, as shown in figure 4.3b. The number of DCR pulses present during the measurement is evaluated using a technique which is explained later. Figure 4.4 shows the distribution of correlated pulses in amplitude and arrival time. DiXTs are composed of single and multiple

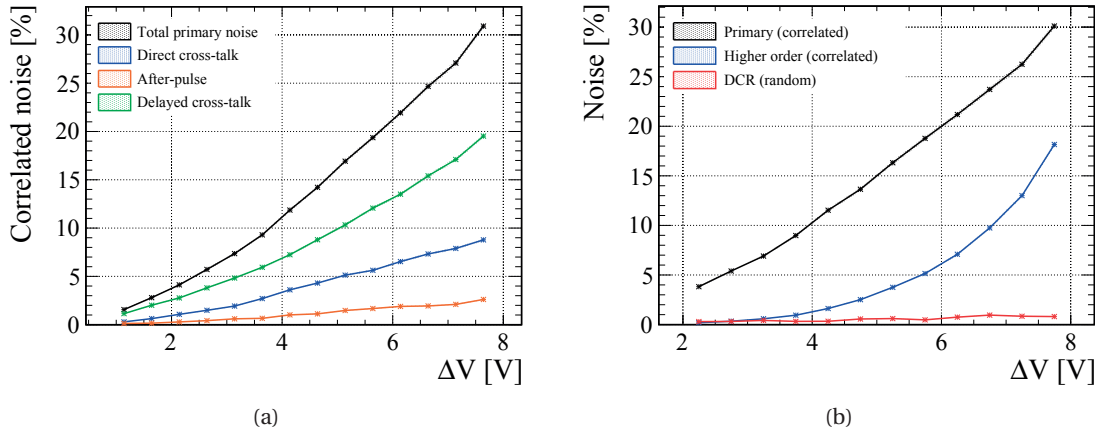


Figure 4.3 – Correlated noise composition for an H2017 detector as a function of ΔV (left). The AP probability is measured with a threshold of 0.5 PE. Total primary and higher order correlated noise (right). The fraction of pulses attributed to DCR is also shown.

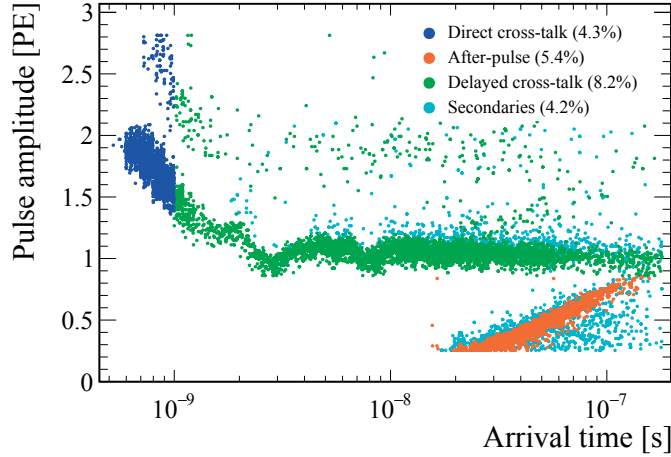


Figure 4.4 – Amplitude and time delay of classified correlated noise pulses for an H2017 detector operated at $\Delta V = 4.8$ V. The detection threshold for APs is set here to 0.25 PE. Note the logarithmic scale of the x-axis.

simultaneous DiXT (up to 3 PE is reached) and show a spread in amplitude resulting from small time delay. The figure also shows the effect of the ringing on the amplitude DeXTs. Delayed pulses with amplitude well above 1 PE are caused by DiXT from DeXTs or APs.

Long pulse component time constant Clean waveforms are used to obtain the time constants of the pulse shape. The time constant associated with the fast falling edge cannot be accurately determined due to the ringing and the bandwidth limitation introduced by the acquisition system. The slow falling edge of the pulse is fitted with an exponential function to find τ_{long} , as illustrated in figure 4.5a.

Recovery time constant The pixel recovery time constant τ_{rec} is measured from AP waveforms. The AP amplitude is linked to the recovery state of the pixel and assumed to follow the relation $1 - e^{-\frac{t-t_0}{\tau_{\text{rec}}}}$, where t_0 is the time needed for the recovery to start. A correction to the

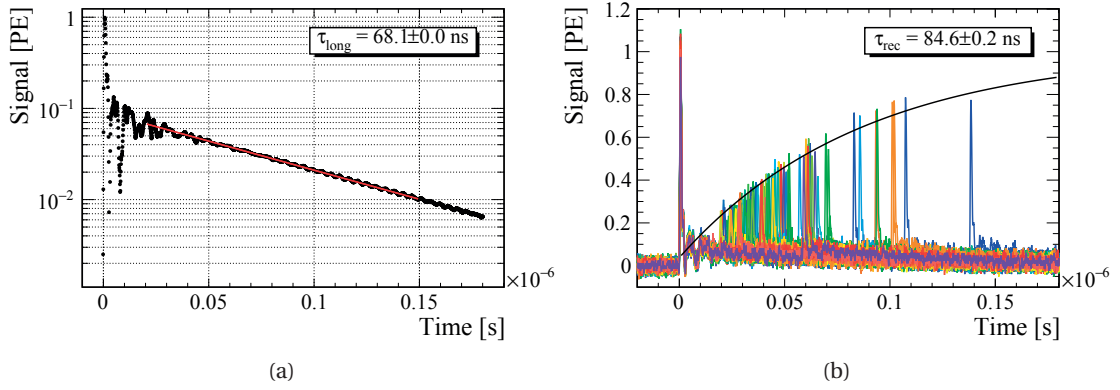


Figure 4.5 – Determination of the long decay time constant using the average pulse shape of clean waveforms (left) and the recovery time using after-pulses (right) for an H2017 detector.

amplitude is introduced to compensate for the slow component of the primary pulse. The fit function is:

$$A(t) = A_{1\text{PE}} \cdot \left(1 - e^{-\frac{t-t_0}{\tau_{\text{rec}}}}\right) + A_{\text{slow}} \cdot e^{-\frac{t}{\tau_{\text{long}}}}, \quad (4.2)$$

where A_{slow} is the amplitude of the slow component of the SiPM pulse. The two parameters A_{slow} and τ_{long} are given by the fit of the long pulse component and t_0 is fixed to the average observed value (4 ns for H2017). An illustration of the fit is shown in figure 4.5b where the waveform of hundred AP events are superimposed.

AP and DeXT mean lifetime The AP mean lifetime τ_{AP} is calculated with an exponential fit of the arrival time distribution as shown in figure 4.6a. Knowing τ_{AP} and τ_{rec} and using a numerical integration, one can calculate the fraction of missed APs due to the amplitude and time thresholds applied. For a threshold of 0.5 PE, the fraction of missed APs is 93%.

An exponential function is also used to describe the arrival time of DeXT pulses and allows to obtain the mean lifetime τ_{DeXT} as shown in figure 4.6b. The offset from the baseline is measured and attributed to random dark pulses present during the measurement. In this particular example, 204 delayed pulses are attributed to dark pulses for a total of 50k waveforms. This corresponds to 5.6% of the detected DeXT pulses and 0.4% of all detected delayed pulses. The fraction of delayed pulses attributed to DCR is monitored in figure 4.3b.

Time constants and the SiPM model The measured time constants (τ_{long} , τ_{rec} , τ_{AP} , τ_{DeXT}) are consistent within the uncertainties over a wide operation range ($\Delta V = 1$ to 8V). We obtain $\tau_{\text{rec}} = 84 \text{ ns}$ and, using $R_Q = 503 \text{ k}\Omega$ obtained from the IV measurement (see section 4.5), we can compute the gain $G/\Delta V = (C_d + C_Q)/e = \tau_{\text{rec}}/(R_Q \cdot e) = 1.05 \cdot 10^6 \text{ V}^{-1}$. This is in good agreement with the value of $1.02 \cdot 10^6 \text{ V}^{-1}$ found with an independent method described in section 4.3. In contrast, the value obtained for the long time constant $\tau_{\text{long}} = 67 \text{ ns}$ is in contradiction with the prediction of the model $\tau_{\text{long}} = \tau_{\text{rec}}$. The results are compatible with $\tau_{\text{long}} = R_Q \cdot C_d$ where $C_d = 136 \text{ fF}$ and $C_Q = 34 \text{ fF}$.

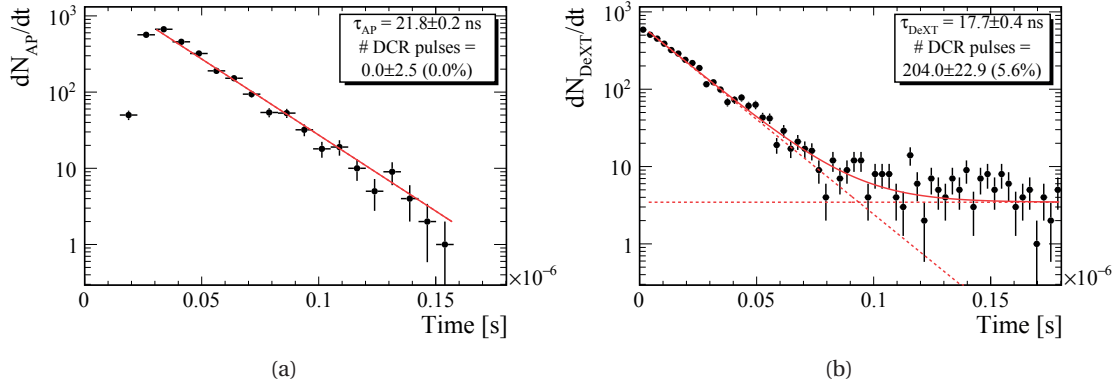


Figure 4.6 – Mean lifetime determination and dark pulse contribution estimation from the arrival time distribution of AP (left) and DeXT (right).

Results on a large sample The correlated noise was measured on a large number of devices for the quality assurance of SiPMs in the context of the SciFi tracker. We have measured a difference between the first delivered lot (500 devices) and the second one (5000), as shown in figure 4.7. From device to device within each lot, the variations of p_{DiXT} , p_{DeXT} and p_{AP} are in the order of $\pm 1\%$. The time constant τ_{AP} is similar for all devices whereas the variations in τ_{long} and τ_{rec} are explained by the differences in the quench resistor value. The delayed cross-talk mean lifetime τ_{DeXT} has changed from approximately 18 ns to 9 ns (first and second lot, respectively).

The difference between the two lots cannot be understood without knowing the details of the changes implemented by the manufacturer. We have observed large AP probability in a previous prototype version (H2015, see appendix B) which was not expected even from the low quench resistor value. We suspect that, between the 2015 and 2017 versions, some effects on the silicon purity, doping or manufacturing process were not well under control.

4.2.3 Correlated noise at -40°C

The correlated noise composition was measured at -40°C for an H2017 detector (first lot). Figure 4.8 shows that only the AP probability changes substantially, with a reduction by a factor of 2 at -40°C . The DiXT is unchanged whereas the DeXT is increased by approximately 14% only at $\Delta V > 4$ V. The time constants τ_{long} and τ_{rec} are increased by approximately 40 to 45% at low temperature due to the quench resistor temperature dependence (see section 4.5.3). The AP and DeXT mean lifetimes τ_{AP} and τ_{DeXT} are also increased by 30 and 10%, respectively. The changes in τ_{rec} and τ_{AP} lead to a modification of the AP time distribution which affects the computation of p_{AP} at the fixed detection threshold of 0.25 PE. Using the amplitude and time distribution of APs (obtained from the fits illustrated in figures 4.5b and 4.6a), a numerical integration can be performed to calculate the fraction of missed after-pulses and therefore the total AP probability. We estimate a reduction of the total AP probability by a factor 2.3 between room temperature and -40°C .

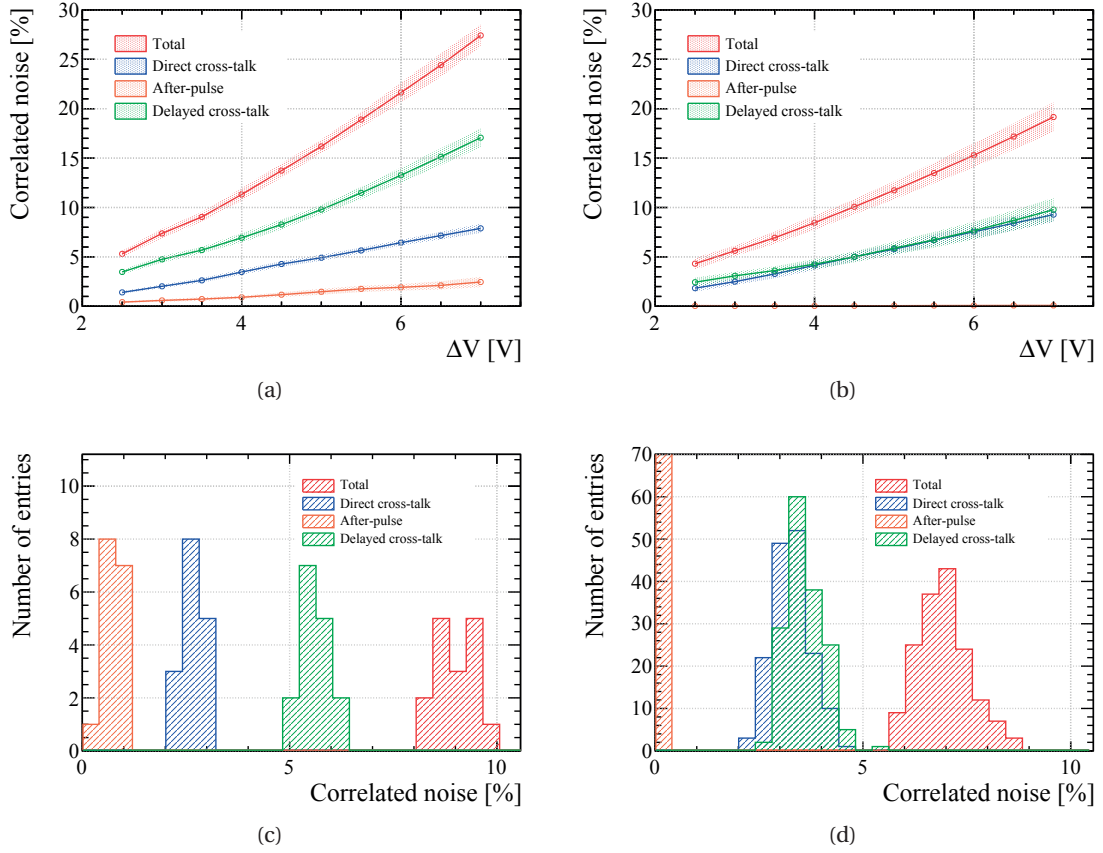


Figure 4.7 – Correlated noise average (top) and distribution at $\Delta V = 3.5$ V (bottom) of H2017 detectors measured with QA samples from the first lot (left) and the second lot (right). The after-pulse is measured with a threshold of 0.5 PE. The uncertainty band (top plots) correspond to the RMS between all measured devices.

4.2.4 Direct cross-talk of irradiated detectors

The application of the waveform analysis to irradiated detectors yields valid results apart from the measurement of delayed correlated noise which is dominated by the high DCR. Some precautions must nevertheless be taken in the data acquisition and the interpretation of the results. The high DCR produces a large baseline fluctuation from overlapping dark pulses which alters the V_{BD} and DiXT measurements. This is mitigated by implementing a veto time interval (400 ns) before the trigger in the oscilloscope data acquisition.

Non-irradiated detectors illuminated with continuous light (injected random pulse frequency f_{light}) are used to verify that no systematic error is introduced by the analysis. The calculation of the breakdown voltage using the pulse amplitude is found to be very robust. The obtained value is almost independent of the noise level (maximum 50 mV deviation for $f_{\text{light}} \approx 10$ MHz with respect to the reference without light).

The DiXT probability is measured in a very short time window (1 ns) from the trigger time. In high DCR conditions, there is a significant probability that two random pulses occur very close in time such that their overlap fulfils the DiXT detection condition. The occurrence of

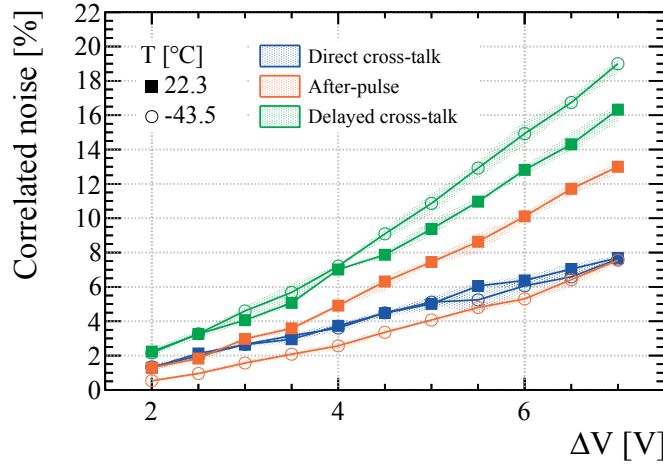


Figure 4.8 – Correlated noise at room temperature and at -40°C for an H2017 SiPM. The uncertainty band corresponds to the min-max difference between the three tested channels. The AP probability is measured with a threshold of 0.25 PE.

random dark pulses in a time interval Δt follows a Poisson process where the λ parameter is given by $\lambda = \Delta t \cdot f_{\text{DCR}}$. Therefore, after the primary pulse, the distribution of secondary pulse arrival time is expected to be characterised by a $e^{-t \cdot f_{\text{DCR}}}$ decay. Figure 4.9 shows an example of such distribution. From an exponential fit, the expected number of dark pulses in the DiXT time window can be computed and subtracted to the number of detected DiXT events. This procedure was tested with non-irradiated H2017 and H2014 detectors over a wide range of operation voltages and with random light illumination up to $f_{\text{light}} = 15 \text{ MHz}$. The obtained DiXT is compatible with the measurement without illumination within less than 10%. A 10% relative uncertainty is therefore adopted for the DiXT measurement of irradiated detectors.

The results for irradiated H2017 SiPMs is displayed in figure 4.10. No trend in the dependence of the DiXT probability as a function of irradiation level can be extracted. The difference between each curve is compatible with the 1%-variation expected from one device to another.

4.2.5 Qualitative comparison with other works

In this section, we shortly describe and compare the other characterisation methods of references [87, 88, 89] based on waveform analysis. In these works, the tested SiPMs feature high DCR (0.1 – 10 MHz) due to the large surface. To cope with the high frequency of random pulses, different strategies providing robustness and precision are reported.

A fast acquisition system very similar to our setup is used in [87] where 1 ms-long waveforms are recorded with a random trigger. The measurement of correlated noise is based on the analysis of two distributions: pulse amplitude and time interval between consecutive pulses. A special algorithm called *differential leading edge discriminator* (DLED) [90] is used to filter the slow tail of pulses^f. It enables to suppress overlap and assign correct amplitude to all pulses

^f The DLED algorithm was originally developed and optimised for timing measurements with SiPMs coupled to scintillators.

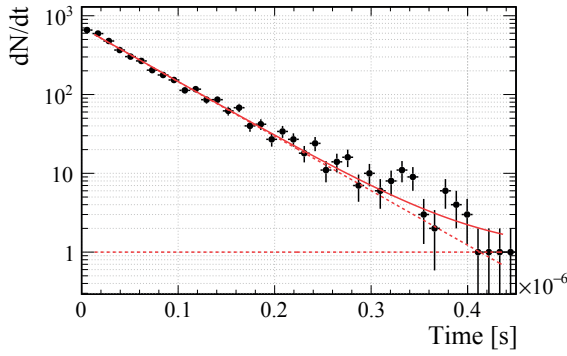


Figure 4.9 – Distribution of the time difference between two consecutive random pulses in the case of high DCR.

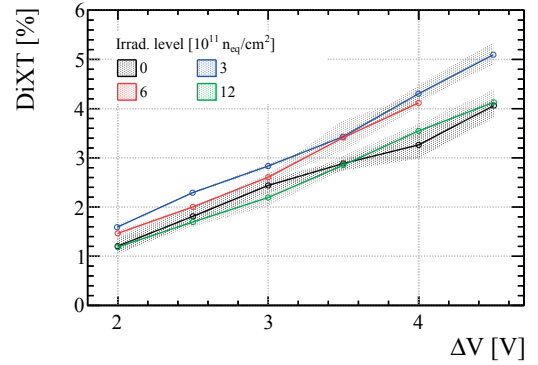


Figure 4.10 – DiXT (corrected for the DCR contribution) as a function of ΔV for irradiated H2017 detectors at -40°C . The uncertainty band corresponds to the min-max difference between three channels.

even in the case of short time delays. From the amplitude distribution, the total DCR and the DiXT probability are computed. On the other hand, the time interval distribution is fitted using a Poissonian model to describe the random generation of DCR pulses. The deviations from the model, visible at small time interval, can be counted and are attributed to DeXT and AP. Pulse shape and gain are determined using the original waveform, before filtering.

In [88], the reduced bandwidth and low sampling rate of the setup (125 MHz, 250 MS/s) does not allow to observe the fast pulse component. Waveforms of $4\ \mu\text{s}$ duration in response to a fast, low intensity light pulse are recorded. The offline waveform processing is rather complex and includes a moving average algorithm for smoothing. For pulse detection, a zero-pole cancellation is implemented in order to retain only the fast rising edge. The DCR and DiXT probability are obtained from the number of random pulses present before the light pulse and their amplitude distribution. The AP probability is computed using pulses delayed in time with respect to the light while DeXT is not considered. The complicated processing and analysis are validated using a simulation.

Reference [89] focuses on the measurement of DiXT to test different generation models. Using an analogous setup as ours, long waveforms in the dark ($400\ \mu\text{s}$) and short ones under low light illumination ($200\ \text{ns}$) are recorded. The analysis is optimised to measure accurately the pulse height. The detection of peaks involves a zero-pole cancellation and only well resolved peaks are considered ($> 20\ \text{ns}$ time separation). Cuts on amplitude allow in addition to reject APs. The baseline before each pulse is fitted with an exponential function and the peak height is computed using the extrapolation of the fit to the peak time. Large statistic is acquired in order to reduce the uncertainty on the measurement of multiple simultaneous cross-talks.

Our setup and method have been developed and optimised to characterise SiPMs with pronounced fast component and low DCR: acquisition system with high bandwidth and sampling rate, minimisation of ringing, EMI shield. The discrimination between correlated noise types only requires sets of thresholds and time windows. This allows to measure the occurrence probabilities with very high precision also when the correlated noise is at the per cent level.

The uncertainty only arises from the statistical error which is determined by the number of acquired waveforms. Missed pulses due to the amplitude and time thresholds can be accounted using the comprehensive analysis of time and amplitude distribution of noise.

The setup is equipped with a cooling system which allows to characterise large-surface SiPMs. This is illustrated in appendix B where recent 1×1 and $3 \times 3 \text{ mm}^2$ devices are tested and the influence of DCR is kept below 4%. As discussed previously, our method is however limited in the case of very high DCR such as in irradiated devices. For the measurement of delayed correlated noise, we suggest to employ the method described in [87] using long waveforms and the distribution of time interval between consecutive pulses. For detectors with very low DeXT and AP probability, the uncertainty on the measurement will be dominated by the fit to the Poissonian model.

4.3 Gain measurement

The gain is independent on the primary source of the avalanche (optically or thermally generated e - h pair) and can therefore be measured with either light or dark noise. It is proportional to ΔV and can be expressed in units of elementary charge as $G = \Delta V \cdot (C_d + C_Q) / e$. In the following we use $G/\Delta V$ which has the dimension V^{-1} and only depends on the detector capacitance $C_d + C_Q$. The latter is dominated by C_d which is the pixel capacitance proportional to the pixel active surface and inversely proportional to the avalanche region thickness. The measurement of C_d allows to compare the avalanche region thickness of different devices and technologies. Two independent methods to determine the gain are explained.

Voltage pulse time-integration The gain can be obtained from the charge delivered by single photon pulses as $G \cdot e = \int I dt$. With the waveform analysis presented in section 4.2, we can evaluate this charge from a numerical integration of the voltage pulses $\int U dt$ after selection of single-pulse events. The gain is computed as $G = [1/(R_{\text{load}} \cdot G_{\text{Amp}} \cdot e)] \cdot \int U dt$, where R_{load} is the preamplifier input impedance and G_{Amp} is the gain of the acquisition chain. In order to avoid any systematic error, G_{Amp} must be calibrated. For the fast H2017 signals, it proved difficult to calibrate G_{Amp} to a good level of precision because the system's input bandwidth is non-linear with signal amplitude and speed. As a result, we use this method only for relative gain measurement for example to compare the gain between devices having comparable pulse shape.

Current and pulse-frequency measurement The most accurate gain measurement is based on the dark current I and the pulse frequency f :

$$I = f \cdot \mathbb{E}(Q), \quad (4.3)$$

where $\mathbb{E}(Q)$ is the expectation value of the pulse charge. In the absence of DiXT and AP, it is simply given by $G \cdot e$. The probability of having n DiXTs is expected to follow the Borel distribution from equation (2.6) with the parameter λ being found from equation (4.1). Therefore,

taking DiXT into account, the actual expectation value of the charge, is, in units of $G \cdot e$:

$$\frac{\mathbb{E}(Q)}{G \cdot e} = \sum_{n=0}^{\infty} (n+1) \cdot P_{\text{Borel}}(n) = 1 + \overbrace{\sum_{n=1}^{\infty} n \cdot P_{\text{Borel}}(n)}^{\mathbb{E}(Q_{\text{DiXT}})/(G \cdot e)} = 1 + w_{\text{DiXT}} \cdot p_{\text{DiXT}}, \quad (4.4)$$

where $\mathbb{E}(Q_{\text{DiXT}})$ is defined as the expectation value of the charge from DiXT events and w_{DiXT} is a weight attributed to DiXT pulses such that $\mathbb{E}(Q_{\text{DiXT}})/(G \cdot e) = w_{\text{DiXT}} \cdot p_{\text{DiXT}}$. At low DiXT probability, it is a good approximation to use $w_{\text{DiXT}} = 1$. The error introduced by this simplification grows rapidly with p_{DiXT} . For $p_{\text{DiXT}} = 10\%$ and $p_{\text{DiXT}} = 20\%$ a calculation using the Borel model shows that $w_{\text{DiXT}} = 1.20$ and 1.45 respectively.

The pulse frequency is measured with a statistical function on the digital oscilloscope. We employ a statistical method counting peaks in a large interval of $100 \mu\text{s}$ with an adjusted threshold. Note that, calculated in this way, f_{DCR} contains all the delayed cross-talks but only a small fraction of the after-pulses, since most of the APs are produced early and therefore with small amplitude. A correction for the contribution of the small APs to the current can be computed from the mean lifetime and recovery time.

Note that the assumption of a linear relationship $I \propto G$ is only valid for a restricted operation range. The so-called incomplete quenching effect, related to a too low R_Q value or high ΔV operation, leads to an additional current.

4.3.1 Results for an H2017 detector

The contribution of DiXT and after-pulse to $\mathbb{E}(Q)$ can be accurately determined from the waveform analysis introduced in section 4.2. For the H2017 detector, some simplification can be done due to the low p_{AP} and p_{DiXT} . The effect of AP is neglected and, given that $p_{\text{DiXT}} < 10\%$ up to $\Delta V = 8\text{V}$, we use the approximation $w_{\text{DiXT}} = 1$. The gain is found to be perfectly linear up to $\Delta V = 8\text{V}$. For the same device as the one presented in section 4.2.2, we find $G/\Delta V = (1.02 \pm 0.01) \cdot 10^6 \text{ V}^{-1}$ which is in perfect agreement with the value calculated from the recovery time. We observe a small difference between devices of the first and second lot produced by the manufacturer: $G/\Delta V = (1.09 \pm 0.02) \cdot 10^6$ and $(1.02 \pm 0.02) \text{ V}^{-1}$, respectively.

4.3.2 Relative gain of irradiated detectors

To measure the absolute value of the gain for irradiated devices, the current and pulse-frequency method is not applicable. Counting the number of pulses on the oscilloscope fails due to the overlap of random dark pulses. The relative gain measurement based on numerical integration of the waveforms is however still valid. The difficulty with this method at high DCR is that clean events with a single dark count are rare. By plotting the distribution of charge, several peaks corresponding to the number of dark pulses present in the waveform are observed. The charge of 1 PE-pulses ($Q_{1 \text{ PE}}$)[§] is precisely determined from a fit of the first peak in the distribution with a Gaussian function. Figure 4.11 shows the charge distribution as

[§] Note that, in the waveform analysis, $Q_{1 \text{ PE}}$ from the numerical integration has unit $[\text{V} \cdot \text{s}]$. The charge in $[\text{C}]$ can be obtained by $Q_{1 \text{ PE}}/R_{\text{load}}$.

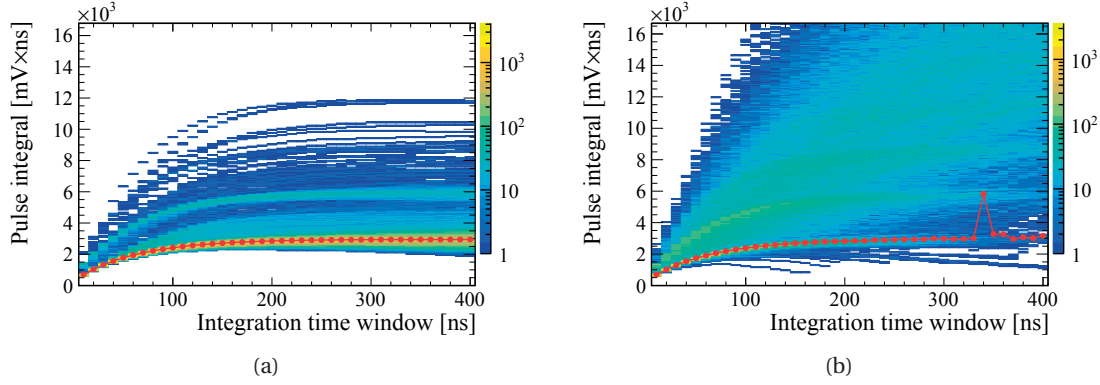


Figure 4.11 – Pulse integral as a function of integration time τ_{int} for an H2017 detector at $\Delta V = 3.5\text{V}$ without (left) and with (right) continuous light injection ($f_{\text{light}} \approx 13\text{ MHz}$). The 1 PE-charge in red is calculated for each τ_{int} from a fit of the first peak in the charge distribution.

a function of the integration time window τ_{int} . The precision on the determination of $Q_{1\text{ PE}}$ can be improved using short τ_{int} .

The validation of this technique was performed with non-irradiated H2017 and H2014 detectors operated between $\Delta V = 1.5$ and 4.5V illuminated with random light with f_{light} up to 15 MHz . The method does not introduce any systematic error due to the high DCR. The relative uncertainty on the charge value is obtained to be 3%.

The results for irradiated H2017 devices are shown in figure 4.12 for two different τ_{int} . Using $\tau_{\text{int}} = 10\text{ ns}$, the $Q_{1\text{ PE}}$ can be determined up to the highest irradiation level tested. For longer τ_{int} , too many dark pulses are present in the time window at $12 \cdot 10^{11}\text{ MeV n}_{\text{eq}}/\text{cm}^2$ and $Q_{1\text{ PE}}$ cannot be computed. The slope of $Q_{1\text{ PE}}$ as a function of ΔV , found from a fit with a linear function, is proportional to $G/\Delta V$. We observe a reduction of $G/\Delta V$ larger than 5% which cannot be explained by the expected variations from one device to another (typically below 2%). A very small dependence on the irradiation level is seen (5, 6 and 7% reduction for $3, 6$ and $12 \cdot 10^{11}\text{ MeV n}_{\text{eq}}/\text{cm}^2$).

4.4 Photon detection efficiency

The measurement of the absolute PDE requires a precise determination of the gain and the correction for correlated noise. In the following, two independent methods providing the PDE as a function of wavelength and ΔV are described and the corrections discussed. The first one uses the photodetector's current under illumination and requires the determination of the gain. The second method is based on counting the pulses in a similar way as for the gain measurement method described in section 4.3. It is well suited for small-area devices (low f_{DCR}). The measurement method based on the current is preferred for high f_{DCR} devices because it is not affected by the overlap of random pulses.

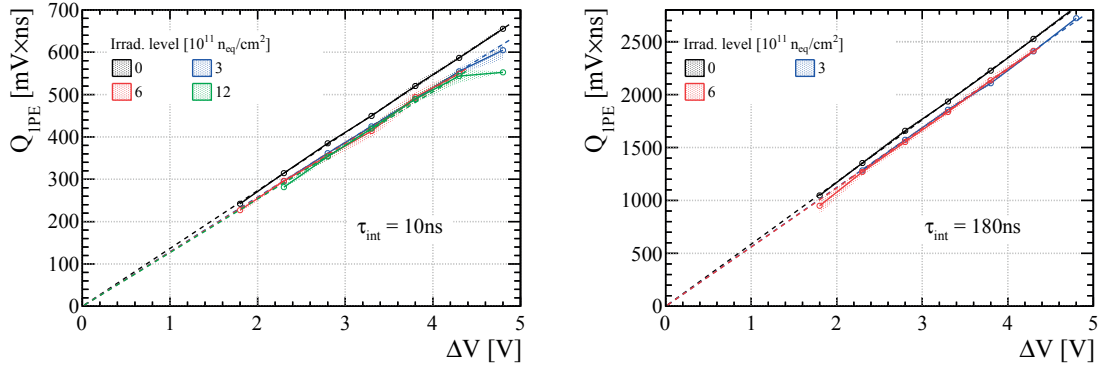


Figure 4.12 – Single-photon pulse integral as a function of ΔV for irradiated H2017 detectors at -40°C measured with an integration time of $\tau_{\text{int}} = 10$ (left) and 180 ns (right), compared with a non-irradiated detector operated in the same conditions. A fit is performed with a linear function of the form $Q_{1\text{PE}} = \alpha \cdot \Delta V$ (dashed lines). The uncertainty band corresponds to the min-max difference between three channels.

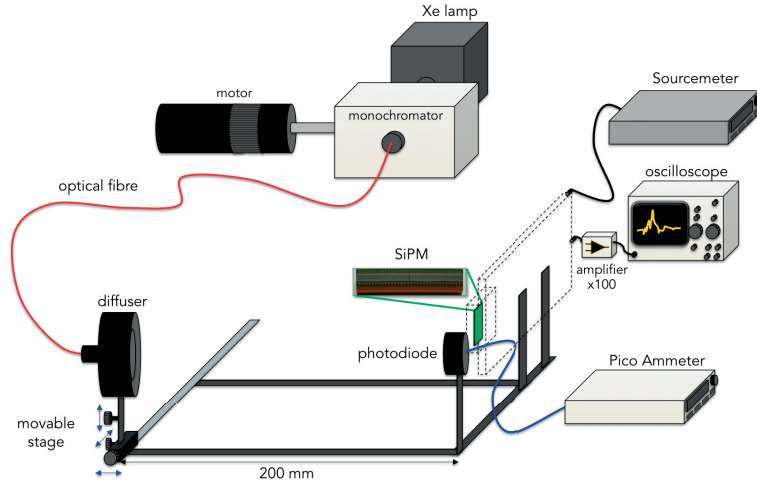


Figure 4.13 – Sketch of the PDE measurement setup. Image from [91].

4.4.1 Measurement setup

A schematic view of the PDE measurement setup is displayed in figure 4.13. We use a continuous light source composed of a Xe lamp and a monochromator controlled by a step motor. The monochromator allows to select a narrow wavelength region (± 1 nm) of the Xe lamp spectrum (from 200 nm to 750 nm). The light is injected into an optical fibre (550 μm diameter) using a collimator. The light beam is made homogeneous using a light diffuser. The calibration of the luminous power surface density P_{lum} is made by a calibrated photodiode sensitive in the range of 160 to 900 nm. Its current is measured by a picoampere-meter^{*h*}. The adjustment of the light intensity is made such as to provide sufficient optical power to the photodiode for the calibration and to avoid saturation of the SiPM.

The relationship between P_{lum} and the rate of incident photons (R) is: $P_{\text{lum}} = (R/A) \cdot (hc/\lambda)$,

^{*h*} Keithley 6485

where A is the sensitive area, h is the Planck constant, c the speed of light and λ the wavelength. The luminous power density can also be calculated from the measured photodiode's current using the relation $I = S \cdot A \cdot P_{\text{lum}}$, where S is the radiant sensitivity, given by the photodiode calibration. The radiant sensitivity is related to the quantum efficiency as $QE = S \cdot (hc)/(\lambda \cdot e)$. In our setup with a distance of 200 mm and the surface of the photodiode $A = 83.3 \text{ mm}^2$, the resulting P_{lum} is in the range of 1.2 to 5.0 pW/mm² depending on the wavelength. The maximum variation in the uniformity of the light intensity at the SiPM was found to be 1% over the active surface. The light beam can be displaced on a xy -positioning stage and the position with maximal intensity is used as reference.

To test detectors with small pixels, the PDE measurement can be performed in an EMI-box in order to reduce the noise. In this case, only a relative PDE measurement is done due to space constraints. The light is transported with an optical fibre inside the box and motorised linear stages allow for the alignment between the diffuser and the detector (adjustment of the position to the peak luminous power).

4.4.2 Method based on the current

The measured current I_{recorded}^* ^{*i*} of an SiPM in a light beam is the sum of the photocurrent I_{light}^* and the dark current, I_{dark}^* . Both contributions can be corrected for any type of correlated noise by a correction factor $(1 - r_{\text{curr}})$. DeXT contributes to the current with pulses of 1 PE and AP with a fraction of 1 PE pulses. To correct for the variable amplitude of AP, we define the weight w_{AP} such that $w_{\text{AP}} \cdot p_{\text{AP}}$ is equal to the total charge released from AP (w_{AP} and p_{AP} depend on the detection threshold). DiXT contributes to the current with one or several additional 1 PE-charges. As discussed in section 4.3, we can attribute a weight w_{DiXT} to p_{DiXT} in order to account for multiple DiXTs.

The correction for the correlated noise is accurate for high ΔV where correlated noise probabilities are above 10%, only if higher order correlated noise is taken into account (e.g. AP of DiXT and AP of DeXT). In the waveform analysis the higher order corrections are calculated for this purpose (see for example figure 4.3b). The average charge $w_{\text{h.o.}}$ in such pulses and the probability $p_{\text{h.o.}}^{\text{curr}}$ of their occurrence are made available. The relation between the current measured on the SiPM and the different noise contributions are expressed by the following equation:

$$I^* = I \cdot [1 + (p_{\text{DeXT}}) + (1 \cdot w_{\text{DiXT}} \cdot p_{\text{DiXT}}) + (w_{\text{AP}} \cdot p_{\text{AP}}) + (w_{\text{h.o.}} \cdot p_{\text{h.o.}}^{\text{curr}})]. \quad (4.5)$$

Equation (4.5) is valid for a current produced either by light or by dark noise. By inverting this relation, we find the current produced by light via the correction factor r_{curr} :

$$I_{\text{light}} = I_{\text{light}}^* \cdot (1 - r_{\text{curr}}). \quad (4.6)$$

The recorded current must still be corrected by the dark current. The final expression for the

^{*i*} In the following, quantities that also contain a contribution from correlated noise are marked with an asterisk.

photocurrent is:

$$I_{\text{light}} = (I_{\text{recorded}}^* - I_{\text{dark}}^*) \cdot (1 - r_{\text{curr}}), \quad (4.7)$$

where I_{recorded}^* and I_{dark}^* are measured respectively with injected light and in the dark. Finally, using equation (4.7), the SiPM gain G and the ratio of the active surface of the calibrated photodiode A_{PD} to the one of the SiPM A_{SiPM} , the PDE can be computed as:

$$\text{PDE} = \text{QE}_{\text{PD}} \cdot \frac{I_{\text{light}}}{G \cdot I_{\text{PD}}} \cdot \frac{A_{\text{PD}}}{A_{\text{SiPM}}}. \quad (4.8)$$

The correction factor r_{curr} is obtained from the waveform analysis results as:

$$r_{\text{curr}} = \frac{N_{\text{delayed pulses}}}{N_{\text{ev}} + N_{\text{delayed pulses}}} + (w_{\text{AP}}^{0.6} - 1) \cdot p_{\text{AP}}^{0.6} + w_{\text{DiXT}} \cdot p_{\text{DiXT}}, \quad (4.9)$$

where $N_{\text{delayed pulses}}$ is the number of delayed pulses exceeding the threshold, N_{ev} is the total number of waveforms recorded and the superscript 0.6 indicates that the threshold of AP detection is set to 0.6 PE. The first term in equation (4.9) includes all delayed noise (DeXT, AP and higher order DeXT and AP). The APs are counted as 1 PE pulses. With the second term, we correct for the variable amplitude of APs and account for the ones which have not reached the threshold. The weight $w_{\text{AP}}^{0.6}$ must be calculated using τ_{rec} and τ_{AP} . For the H2017 device that was presented in section 4.2.2 ($\tau_{\text{rec}} = 84$ ns and $\tau_{\text{AP}} = 22$ ns), we find $w_{\text{AP}}^{0.6} = 7.2$. Note that higher order APs are not corrected for their small amplitude which leads to an overestimation of r_{curr} . This effect scales as $(p_{\text{AP}}^{0.6} + p_{\text{DeXT}}) \cdot p_{\text{AP}}^{0.6}$ and is in general small because most of the APs have amplitude smaller than 0.6 PE. The third term enables to account for DiXT and its variable charge, as it was already discussed in section 4.3. In case of high DiXT probability, the weight w_{DiXT} can be calculated to correct for the large charge of multiple DiXTs, assuming that they follow the Borel distribution. For the H2017 detectors, the weight can be approximated by 1 since DiXT has low probability. The expression for r_{curr} does however not account for DiXT on delayed pulses. The expected error is of the order of 0.5% for a total correlated noise probability of 10%.

4.4.3 Method based on the pulse frequency

The second method for PDE measurement uses a low pulse frequency injected from the light source such that random overlap of pulses is rare and therefore cannot significantly affect the precision on the frequency determination. We record the frequency of pulses f_{recorded}^* at a threshold of 0.6 PE. It is the sum of the light induced pulses f_{light}^* and dark pulses f_{dark}^* . These quantities contain contributions from the correlated noise as:

$$f^* = f \cdot \left(1 + p_{\text{AP}}^{0.6} + p_{\text{DeXT}} + p_{\text{h.o.}}^{\text{freq}}\right), \quad (4.10)$$

where f is the frequency of detected primary pulses (light induced or dark count) and $p_{\text{h.o.}}^{\text{freq}}$ is the probability for higher order delayed correlated noise to occur. The frequency of primary

photons f_{light} is therefore computed as:

$$f_{\text{light}} = f_{\text{light}}^* \cdot (1 - r_{\text{freq}}) = (f_{\text{recorded}}^* - f_{\text{dark}}^*) \cdot (1 - r_{\text{freq}}), \quad (4.11)$$

where the parameter r_{freq} is the fraction of pulses due to delayed correlated noise. The DiXT pulses are only counted as one pulse and do not require any correction. Precise values for r_{freq} are obtained from the waveform analysis. It is computed as:

$$r_{\text{freq}} = \frac{N_{\text{delayed pulses}}}{N_{\text{ev}} + N_{\text{delayed pulses}}}. \quad (4.12)$$

The PDE of the SiPM can be calculated as:

$$\text{PDE} = \text{QE}_{\text{PD}} \cdot \frac{f_{\text{light}}}{I_{\text{PD}}/e} \cdot \frac{A_{\text{PD}}}{A_{\text{SiPM}}}. \quad (4.13)$$

4.4.4 Sources of systematic and statistical errors

In both the current and the frequency methods, a source of systematic uncertainty on the PDE is the calibration of P_{lum} . The photodiode calibration has a 1% precision leading to a 1% uncertainty. In addition, the accuracy of the positioning of the photodiode and the SiPM in the light beam introduces the second major uncertainty. Along the beam axis, assuming $d = 200 \pm 2$ mm, a 2% uncertainty is obtained. In the perpendicular plane, the beam non-homogeneity yields a systematic error of 1% for a position accuracy of 0.5 mm.

The systematic uncertainty introduced by r_{curr} for the current-based PDE, as already discussed, is dominated by DiXT-related higher order pulses which are neglected (multiple DiXTs, DiXT on delayed pulses). It increases with p_{DiXT} and ΔV . At $p_{\text{DiXT}} = 10\%$, the systematic uncertainty is estimated to be 2%. In the frequency approach, r_{freq} is not affected by any systematic error. Both r_{curr} and r_{freq} have however an associated statistical uncertainty due to the limited number of events taken for the waveform analysis. For $N_{\text{ev}} = 5000$ recorded, the uncertainty is below 0.5%.

A relevant fraction of the error for the current-based PDE is introduced by the gain measurement. With the method discussed previously, the gain is determined with an accuracy of 1%. Furthermore, assuming that the temperature is stabilised to 0.5°C over the full measurement period, the gain fluctuation results in an additional uncertainty of approximately $1\%^j$.

For the measurement points with low pulse frequency (low light intensity), an uncertainty arises from the small SiPM current which is present for the gain and PDE measurements. In total, the uncertainty is estimated to be $\sim 6.0\%$ for the current and $\sim 3.5\%$ for the frequency approach.

^j For H2017 detectors operated at $\Delta V = 3.5$ V, using $K_T = 59 \text{ mV}/^\circ\text{C}$ in equation (2.2), a change in temperature of 0.5°C results in a relative gain change of 0.8%.

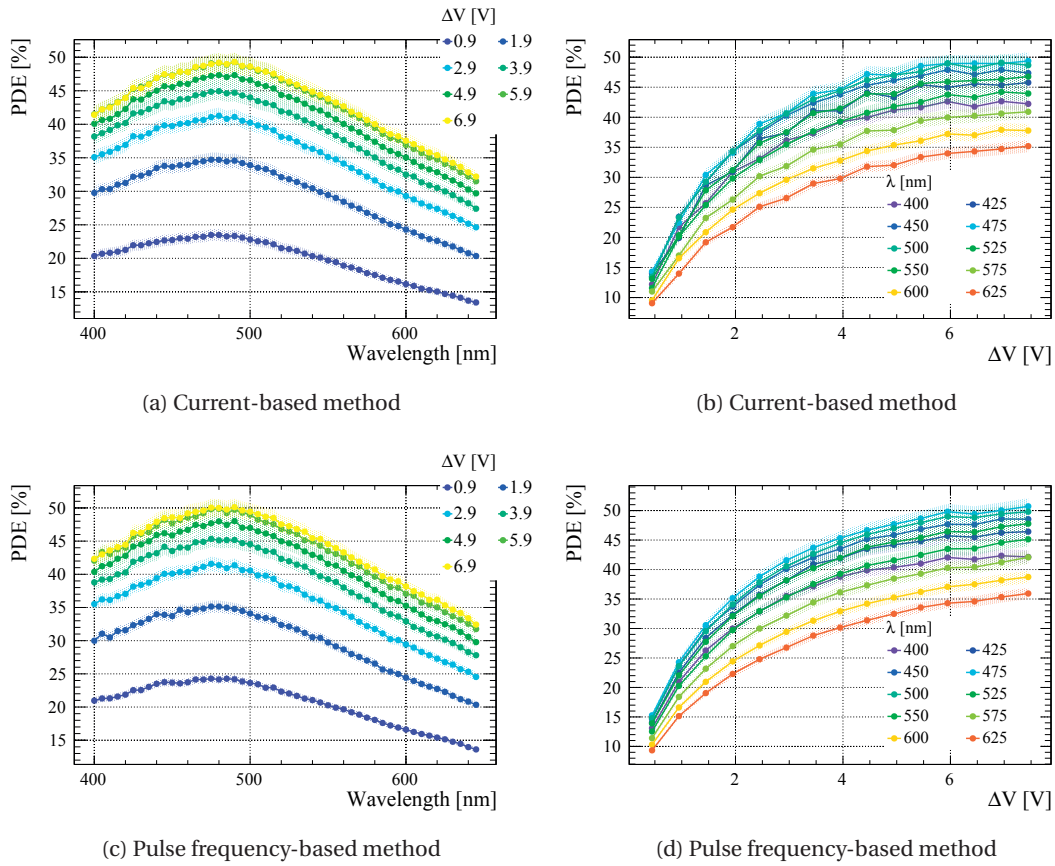


Figure 4.14 – PDE as a function of wavelength (left) and ΔV (right) for an H2017 detector. The results are obtained with the method based on current (top) and pulse frequency (bottom). The curves from the current method are affected by fluctuations which are due the measurement of the current. The smaller fluctuations visible for the frequency method confirm the reduction of the overall uncertainty for this approach.

4.4.5 Results for an H2017 detector

The PDE as a function of wavelength and ΔV for an H2017 detector is shown in figure 4.14. The two methods yield compatible results. The PDE reaches a plateau at high ΔV , as expected from the saturation of the charge carrier ionisation rate at high electric field.

The ΔV -dependent PDE curves can be well described by exponential functions as [52]:

$$\text{PDE}(\Delta V) = \text{PDE}_{\max} (1 - e^{-\Delta V/a}). \quad (4.14)$$

In the PDE (see equation (2.4)), the only ΔV -dependent factor (for a fully depleted device) is the avalanche triggering probability P_{01} . Therefore, the factors in the above fit function can be interpreted as follows: PDE_{\max} is the product of the quantum efficiency and the geometrical fill factor whereas the second term corresponds to P_{01} , assuming that it approaches 100% at high ΔV . Many publications from SiPM manufacturers do not show a complete saturation in the ΔV -dependent PDE which is due to an underestimation of the contribution from correlated noise.

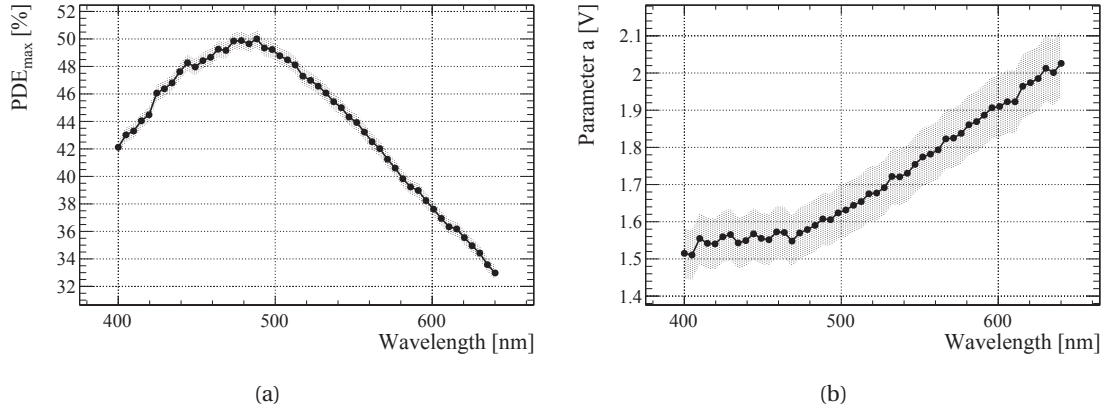


Figure 4.15 – Results of the ΔV -dependent PDE fitted with an exponential function of the form of equation (4.14).

The results of the fit are displayed in figure 4.15. The maximum value reached by PDE_{max} is approximately 50% which is lower than the 60% expected from the QE ($\gtrsim 80\%$) and the fill factor ($\gtrsim 65\%$). Hence, the result infers some transmittance losses due to the epoxy layer (reflections). The P_{01} factor is described by an exponential characterised by the parameter a . As shown in figure 4.15b, a increases with the wavelength which indicates that the plateau is reached at higher ΔV . This behaviour can be explained by the larger absorption length of photons at longer wavelength. For a device with p -on- n structure, the holes are the dominant source for the avalanche triggering for red light. The ionisation rate of holes reaches saturation at higher electric field compared to electrons.

4.5 Current-voltage measurements

Current-voltage (IV) measurement is a very fast, simple and robust method for characterising SiPMs. For devices with high f_{DCR} (from irradiation or large active area) where a continuous overlap of pulses is present, the pulse counting method fails while the IV measurement still provides valid results. Measuring the IV curve gives access to R_Q , V_{BD} and $f_{DCR}(\Delta V)$. This method does not require any high bandwidth data acquisition system and can therefore be implemented with standard test equipment. We use a source meter together with a multiplexer system^k to automate the measurements for multichannel devices. To avoid self-heating during the measurement, the voltage range needs to be limited.

4.5.1 Breakdown voltage

Reference [92] presents a method to determine V_{BD} from IV measurements. It is based on the assumption of a polynomial current increase starting at V_{BD} : $I(V_{bias}) = \alpha \cdot (V_{bias} - V_{BD})^\epsilon$ where α and ϵ are constants that determine the shape of the IV curve. Under this assumption, the

^k Keithley 2612B and Keithley 3706A-NFP

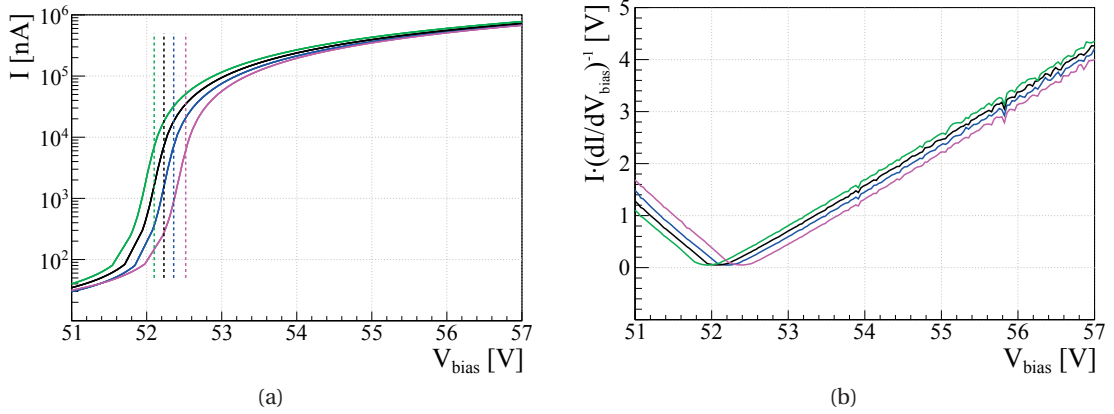


Figure 4.16 – IV curve in reverse direction (left) and parameter of equation 4.15 computed from the IV (right) for four H2017 detectors. The breakdown voltage obtained from this measurement is indicated with the vertical dashed lines on the IV curve.

following quantity varies linearly with the over-voltage:

$$\left[\frac{d \ln(I)}{d V_{\text{bias}}} \right]^{-1} = I \cdot \left(\frac{dI}{d V_{\text{bias}}} \right)^{-1} = \frac{(V_{\text{bias}} - V_{\text{BD}}^I)}{\epsilon} \propto \Delta V, \quad (4.15)$$

where V_{BD}^I denotes the breakdown voltage value obtained with this method. This quantity is fitted with a linear function with ϵ and V_{BD}^I left as free parameters. The fit is typically performed in the range [0.5, 1.5] V above V_{BD} where the linear assumption holds. Illustration of this procedure is shown in figure 4.16. The low current in this ΔV -range allows to neglect the effect of self-heating due to heat dissipation. We observe in addition a non-zero current below V_{BD} depending on dV/dt due to the charging of the detector capacitance ($I = C \cdot dV/dt$). This limits how fast the IV scan can be performed. Continuous illumination of the detector allows for faster and more precise measurements without affecting the value found for V_{BD}^I .

This V_{BD} measurement method was applied to H2017 samples in the quality assurance procedure. Overall, the V_{BD}^I of all measured channels is between 51.0 and 52.6 V with min-max variation within a 128-channel array below 0.7 V. It is also seen that this method yields different results compared to the method based on the gain (from pulse amplitude $V_{\text{BD}}^{\text{Amp}}$ or pulse charge $V_{\text{BD}}^{\text{Int}}$). We observe a 320 ± 10 mV offset between V_{BD}^I and $V_{\text{BD}}^{\text{Int}}$. In [93], similar differences are reported and are attributed to a shift between the p - n junction turn-on and turn-off voltage.

The setup is used to measure the temperature dependence of V_{BD} (coefficient K_T of equation (2.1)). The V_{BD} determination from IV measurements is very robust, fast and fully automated. A large number of channels was measured with the automated testing system using the multiplexer in order to obtain K_T . The V_{BD} is measured between -50°C and room temperature and a linear fit of V_{BD}^I as a function of temperature is performed. We obtain $K_T = 59 \pm 2$ mV/K for H2017 detectors.

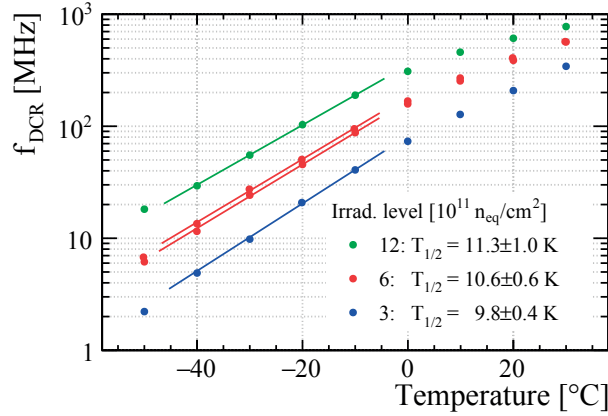


Figure 4.17 – DCR as a function of temperature for irradiated H2017 detectors at $\Delta V = 3.5$ V. The characteristic coefficient for DCR reduction ($T_{1/2}$) is measured from a fit with an exponential function in the range $[-40, -10]^\circ\text{C}$.

4.5.2 Dark count rate

Using the gain obtained in section 4.3, f_{DCR} can be computed with the relation $I = f_{\text{DCR}} \cdot G \cdot e \cdot (1 + p_{\text{DiXT}})$. The f_{DCR} found in this way is the total rate of pulses present in the dark (random and correlated). We introduce a correction for DiXTs which do not generate additional pulses. The IV measurement is best suited for the determination of $T_{1/2}$ since the IV scan is fast and can be completely automated for multichannel devices. The DCR as a function of temperature is shown in figure 4.17 for irradiated H2017 detectors. The coefficient $T_{1/2}^{\text{rad}}$ is extracted from a fit with an exponential function (see equation (2.3)) in the range $[-40, -10]^\circ\text{C}$. In the higher temperature range, the DCR deviates from the exponential trend due to the recovery time of the pixels. $T_{1/2}^{\text{rad}}$ is found to be consistent for different ΔV and irradiation levels. During our R&D to find the best suited SiPM technology for the SciFi tracker, we have selected technologies with the lowest f_{DCR} at -40°C . The prototypes from Hamamatsu have consistently yielded an identical $T_{1/2}^{\text{rad}}$ leading to an acceptable f_{DCR} . For other manufacturers (e.g. KETEK), we have observed that the deviation from the exponential trend holds down to -40°C which causes too large f_{DCR} .

4.5.3 Quench resistor

The IV curve in the forward direction $[-1, 0]$ V shows the typical shape of a forward biased silicon p - n junction. For higher voltages the current is limited by R_Q and shows an almost linear characteristic. The IV curve is fitted with a linear function in the region $[-3.5, -1]$ V. The slope dV/dI is related to the quench resistor of each microcell as: $R_Q = N_{\text{pixels}} \cdot (dV/dI)$. The result depends on the interval used for the fit because the p - n junction introduce a small non-linearity. For the H2017 QA samples, the quench resistor is measured to be 510 ± 50 k Ω . The temperature dependence is found to be -3 ± 1 k $\Omega/^\circ\text{C}$ which is significantly higher than the expectation from reference [51] for Hamamatsu thin metal films and cannot be explained without knowing the details of the implementation.

For multichannel devices, IV scan is a convenient way to verify the connectivity of all channels. For the LHCb SciFi tracker, our industrial subcontractors have performed an approximate R_Q measurement using a multiplexer after the last assembly steps to ensure that all channels are connected.



5 SiPM multichannel array characterisation

In this chapter, we introduce precision measurement techniques for the characterisation of SiPM multichannel arrays and discuss in details the read-out electronics. A measurement setup based on a short fibre module was developed and enables the determination of the gain, breakdown voltage, PDE and noise cluster rate of irradiated SiPMs.

5.1 Light yield measurement setup

The setup, shown in figure 5.1, consists of a fibre module prototype from the BGV detector. It is 34 cm long and comprises five layers of fibres with a mirror. The module includes a cooling system where the SiPMs are operated at -40°C . An electron-gun [94] is used to produce signal in the fibres. It is a small β -spectrometer with a β -emitting ^{90}Sr source and a solenoid coil for energy selection. In addition, it is equipped with a trigger system which is composed of three 1 mm square plastic fibres coupled to two single-channel SiPMs. By measuring the energy spectrum at the output, the energy loss of the electrons in the trigger fibres was estimated to be 200 keV. Electrons with kinetic energy $E_{\text{kin}} = 1 \text{ MeV}$ are selected for the measurements leading to a trigger rate of 300 Hz. The electron-gun is mounted on an xy -moving table which allows to inject signal uniformly over all SiPM channels. The data taking consists in a scan across all read-out channels. During this procedure, the electrons may escape the acceptance of the system resulting in an inefficiency which is expected to show a contribution of zero-signal detection.

5.2 Read-out of multichannel arrays

For the read-out of the SiPM arrays, we employ multichannel integrated front-end ASICs designed for SiPMs. These chips provide charge preamplification, pulse shaping and in certain cases also trigger functionality. Their most important characteristics are the amplifier noise compared to 1 PE, the dynamic range and its linearity, the integration and shaping times τ_{int} and τ_{shaping} .

We have used the following chips: VATA64 [95], SPIROC [96], Beetle [97] and PACIFIC [79]. VATA64 and SPIROC are designed for the read-out of SiPMs; they have a linear response with

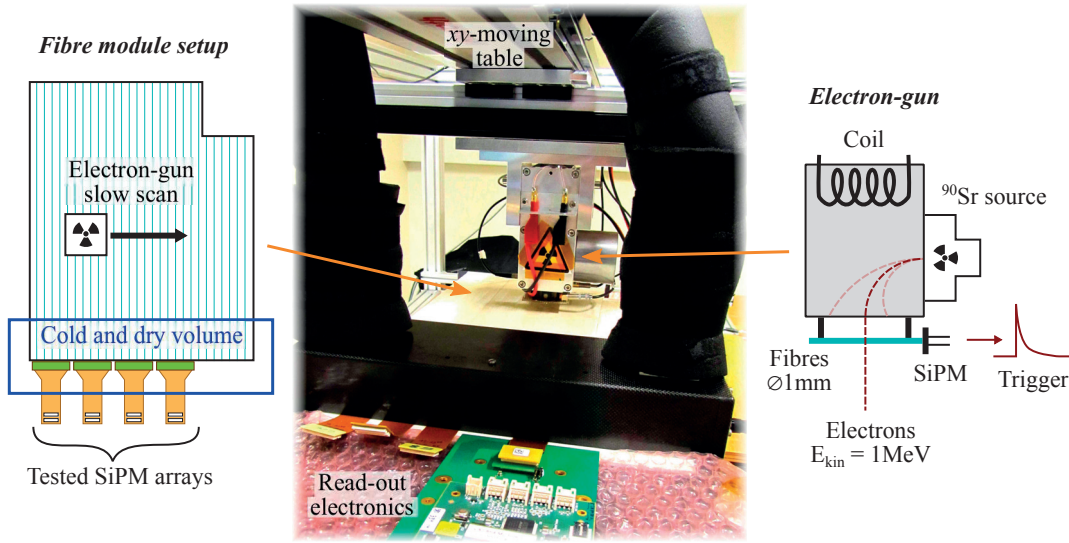


Figure 5.1 – Schemes and picture of the light yield measurement setup and the electron-gun.

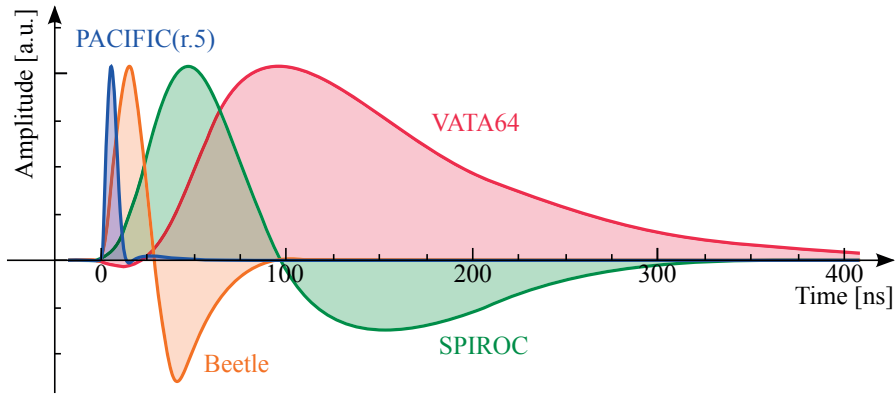


Figure 5.2 – Pulse shaping of different ASICs measured at the analogue output. The measurements were performed with injection of SiPM pulses (VATA64, Beetle and SPIROC) or obtained from a simulation (PACIFIC).

input signal charge and a shaping time of $\tau_{\text{shaping}} > 100$ ns (tunable) and $\tau_{\text{shaping}} \approx 70$ ns, respectively. The Beetle chip is used for the read-out of silicon strip detectors in LHCb. It is used for the first time for SiPM read-out in the BGV detector. The front-end electronics includes a passive attenuator circuit based on an RC -filter to adapt the SiPM output signal to the Beetle preamplifier dynamic range. The chip has a shaping time of $\tau_{\text{shaping}} \approx 25$ ns. We observe a non-linear response with respect to the input signal. The PACIFIC is an ASIC specifically developed for the LHCb SciFi tracker. The amplitude is encoded in a 2-bit information corresponding to three thresholds. It is the input to the clustering algorithm described in section 3.1.2. The integration time is $\tau_{\text{int}} = 25$ ns and the shaping time is $\tau_{\text{shaping}} \approx 10$ ns. The pulse shaping for each chip is shown in figure 5.2.

With the VATA64, SPIROC and PACIFIC, the SiPM bias voltage can be adjusted individually for each channel. It is controlled by a digital-to-analogue converter (DAC) and provides an offset voltage at the preamplifier input of each channel. For precision measurements, VATA64 and

SPIROC are the preferred implementations because of their large dynamic range and linear response.

The data from the front-end electronics is acquired in different modes: we measure subsequently the electronic noise, the SiPM noise, the SiPM response to light and finally the signal from charged particles crossing the fibre module. To measure the noise, a random trigger is used and the SiPM is non-biased or biased. For signal measurement, light pulses from an LED or a laser are injected into the SiPM and a synchronous trigger is provided to the read-out. The response of SciFi modules to particles is measured with the electron-gun. The analogue signal from the front-end is transmitted to the data acquisition electronics where it is digitised using an analogue-to-digital converter (ADC). The acquisition modes are discussed in the following.

Pedestal The signal of a non-biased SiPM (or biased at $V_{\text{bias}} < V_{\text{BD}}$) is an important information about the electronic noise present in the system. The signal is typically larger than zero and follows a distribution where the width corresponds to the noise. The mean value is called the *pedestal*. In the other acquisition modes, the pedestal is used to define the zero amplitude and is subtracted from the measured signals.

Dark With the SiPM biased and a random trigger, the dark noise spectrum of the SiPM is measured. If the mean time between dark pulses is much longer than the shaping time, the dark spectrum is almost identical to the pedestal spectrum, as shown in blue in figure 5.3a. At events with a dark count integrated, the amplitude can be positive or negative depending on the sampling time. With large differences in integration time for the front-end ASICs, the dark spectrum does not only depend on the DCR but also on the shaping. A step structure can be observed due to multiple dark pulses in the integration interval. Figure 5.3a shows the measurements performed with the same SiPM but different levels random noise introduced by a continuous light source.

Low light injection Recording the amplitude spectrum of low intensity light pulses reveals the quantified character of the photons. As shown in figure 5.4, the spectrum exhibits peaks (called photoelectron peaks) which correspond to 0, 1, 2,... photons detected. To obtain good peak separation, low electronic noise is necessary. The increase in width for every subsequent peak is due to the non-uniformity in gain between pixels. The distribution of the number of detected photons is approximately Poissonian. The correlated noise (in particular direct cross-talk) introduces deviations from the Poissonian expectation. After-pulse and delayed cross-talk contribute with amplitudes smaller than 1 PE because of their time delay. In the example of figure 5.4 using VATA64, τ_{shaping} is sufficiently long to integrate all APs and DeXTs and the time delay does not play an important role. The events with amplitude falling between the PE peaks are caused by APs with amplitude below 1 PE. With VATA64 and SPIROC, a good linearity of the PE peak position is observed. The *ADC gain* (G_{ADC}) is measured as the mean value of the peak separation and is expressed in the unit of ADC/PE.

Particle injection A typical amplitude spectrum obtained with particle injection into a fibre module is shown in figure 5.3b. At a triggered event, the electronics reads out all SiPM channels. Since the particle creates scintillation light in a small region (cluster), only a few channels receive a significant signal. This explains the large number of zero signal in the spectrum. The

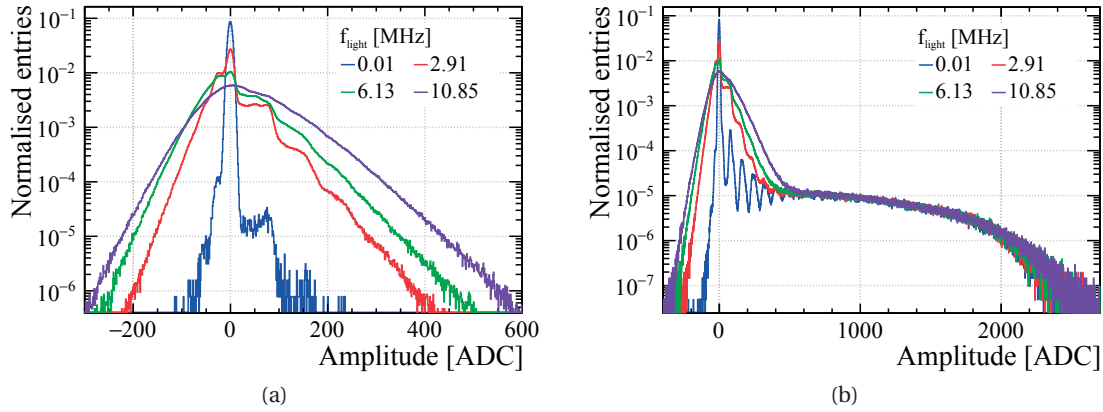


Figure 5.3 – Typical amplitude spectrum of a short fibre module obtained in the dark (left) and with electrons (right) using an H2017 detector and SPIROC electronics. The injection of random light using a continuous light source illustrates the effect of noise.

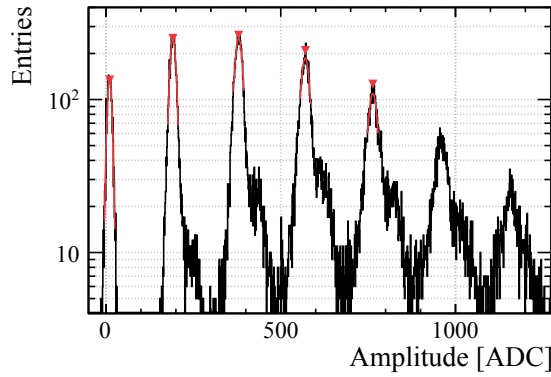


Figure 5.4 – Example of photoelectron spectrum taken with an H2017 detector read out by VATA64. The peaks can be fitted with a Gaussian function in order to find the ADC gain.

small amplitudes are also very frequent because the channels have higher probability to be at the edge of a cluster than in the centre. The PE peaks are visible and can be used to measure the ADC gain. If the DCR is high, the spectrum is dominated by the random noise and the PE peaks are suppressed.

5.3 Breakdown voltage and ADC gain

An alternative technique to the methods described in chapter 4 for the measurement of V_{BD} is based on the low light spectrum recorded with VATA64 or SPIROC. The ADC gain is measured as the mean peak separation in the PE spectrum as shown in figure 5.4. This procedure can be repeated at different V_{bias} points to determine the breakdown voltage. The value obtained with this method is called V_{BD}^{G} . Using VATA64 and SPIROC electronics, the obtained V_{BD}^{G} for H2017 detectors is in good agreement with $V_{\text{BD}}^{\text{Int}}$ found from the SiPM pulse charge.

For systems with integration time $\tau_{\text{int}} < \tau_{\text{long}}$, the ADC gain depends on the pulse shape due to a missing fraction of the slow pulse component. Thus, detectors with the same intrinsic gain

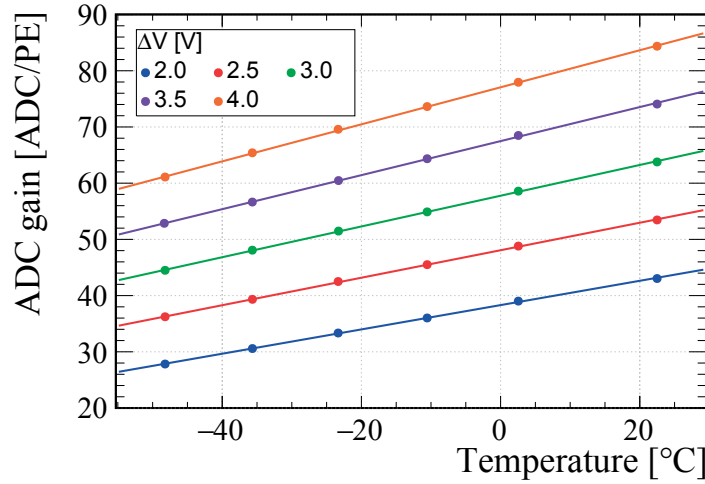


Figure 5.5 – ADC gain as a function of SiPM temperature and ΔV read out by SPIROC.

but different pulse shape can have a different ADC gain. Since R_Q is temperature-dependent and τ_{long} depends on R_Q , the ADC gain of a given device at constant ΔV changes with temperature. We observe an increase with temperature because the pulse shape becomes faster (τ_{long} decreases with temperature). For the H2017 detector with SPIROC electronics, a significant change of the ADC gain with temperature is seen ($\sim 0.3 \text{ ADC/PE/}^\circ\text{C}$ at $\Delta V = 3.5 \text{ V}$), as presented in figure 5.5.

5.3.1 Results for irradiated H2017 detectors

Using the short fibre module introduced in section 5.1, the ADC gain and the V_{BD}^G can be measured for irradiated SiPMs operated at -40°C . The light pulses are injected through the mirror into the fibre module. The SPIROC is used for the read-out because of its short shaping time preventing random overlap of dark pulses.

Effect of high DCR on amplitude spectrum Figure 5.6a displays the low light amplitude spectrum recorded by a non-irradiated detector with continuous light illumination. The increased tail on the left side of each PE peak can be explained by the partial recovery of the pixels due to a relatively long LED pulse (10-15 ns). This effect is enhanced at high DCR. We observe in addition a decrease of the ADC gain with increasing noise level with a linear relative change as a function of f_{light} up to $f_{\text{light}} = 3 \text{ MHz}$ ($\delta G_{\text{ADC}}/G_{\text{ADC}} \lesssim 3\%$). The cause is a change of V_{bias} due to a limitation of the read-out electronics^a. For higher f_{light} , the peaks are smeared out by the left tail of the peaks and the relative change in ADC gain increases non-linearly. In the linear regime up to $f_{\text{light}} = 3 \text{ MHz}$, we can compute a correction coefficient for V_{bias} as a function of f_{light} .

ADC gain and V_{BD}^G measurement The PE spectrum for irradiated SiPMs read out by SPIROC is shown in figure 5.6b. Single photon detection is possible up to the highest irradiation level

^a We observe an increase of the DAC voltage offset due to the large bias current ($f_{\text{DCR}} = 3 \text{ MHz}$ is approximately equivalent to $250 \mu\text{A}$ for an 128-channel array H2017).

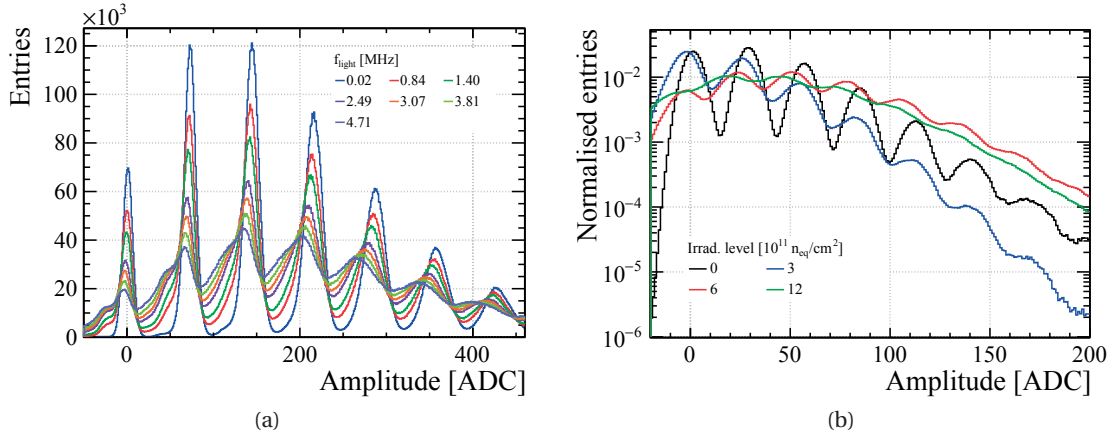


Figure 5.6 – Influence of the random noise on an amplitude spectrum measured with SPIROC. The tested SiPMs are non-irradiated (left) and irradiated (right) H2017 detectors. Random noise is introduced on the non-irradiated SiPM using a continuous light source. Irradiated SiPMs are operated at -40°C and $\Delta V = 2.0\text{V}$.

tested. This enables the measurement of the ADC gain and the breakdown voltage for each individual channel. Considering the effect induced by the high DCR on V_{bias} , the measurement was performed at low ΔV in order to limit the bias current. V_{BD}^G is computed by a fit of the ADC gain as a function of V_{bias} , where the correction for V_{bias} is applied. The obtained average V_{BD}^G is compared with the measurements performed before irradiation. We observe differences below $\pm 200\text{ mV}$ and conclude therefore that no significant change in V_{BD} is induced by irradiation. [98]

The ADC gain of irradiated detectors is displayed in figure 5.7 and shows results compatible with a reduction in the SiPM gain after irradiation. By comparing with the non-irradiated detector, we estimate a decrease in $G/\Delta V$ of 4, 7 and 11% for the irradiation levels 3, 6 and $12 \cdot 10^{11} \text{ 1 MeV n}_{\text{eq}}/\text{cm}^2$, respectively. A reduction between 5 and 7% was already measured with the pulse integral method discussed in section 4.3.2. The disagreement between the reduction factors from the two methods does not allow us to conclude on specific values for the dependence of the gain on the irradiation level. It is nevertheless reasonable to assume that the gain changes by less than 10% after irradiation to $6 \cdot 10^{11} \text{ 1 MeV n}_{\text{eq}}/\text{cm}^2$.

5.4 Light yield of a short fibre module

The light yield of the short fibre module was measured with different versions of SiPM. The measured values are corrected for correlated noise, varying between devices and operation conditions (ΔV). After correction, the light yield can be used to compare the PDE of the tested SiPMs. At high DCR, the probability that noise pulses occur within the electronics shaping time is significant and therefore the contribution of DCR must be taken into account. We have used this method to determine the PDE in cases where the method of section 4.4 fails. This comprises PDE at low temperature and PDE of irradiated SiPMs.

An accurate determination of the pedestal and the ADC gain is required for the application of

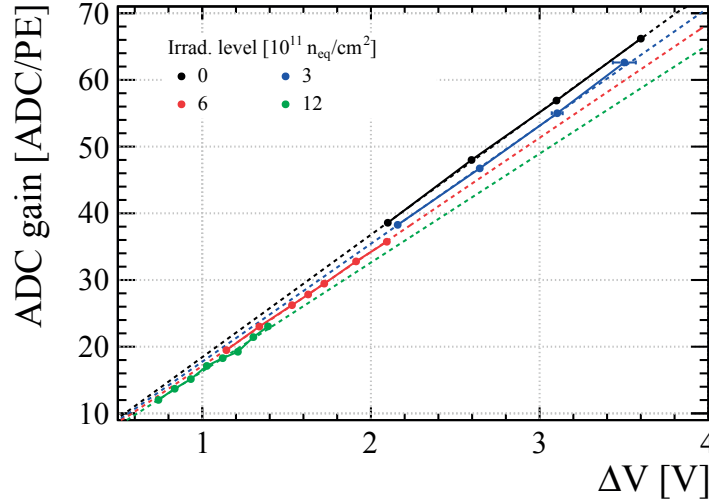


Figure 5.7 – ADC gain as a function of ΔV for irradiated SiPMs operated at -45°C and read out by SPIROC.

the clustering. The pedestal is determined from a dedicated measurement whereas the ADC gain can be computed from the data acquired with electrons using the visible PE peaks in the amplitude spectrum. To reduce statistical uncertainties, the data from the 128 channels of the tested SiPM are combined to measure the ADC gain. Similarly, the light yield is obtained from cluster sum distribution superimposed for all channels.

5.4.1 Correction for the DCR contribution

The average contribution of DCR to the light yield is factorised in three terms:

$$\overline{N_{\text{DCR}}} = \mu \cdot P_{\text{free}} \cdot l. \quad (5.1)$$

The factor μ is the average number of PEs due to noise in the shaping time interval. In a simple Poisson model considering the electronics shaping as a square function with width τ_{shaping} , it is given by $\mu = \tau_{\text{shaping}} / \tau_{\text{DCR}} = \tau_{\text{shaping}} \cdot f_{\text{DCR}}$. To account for the actual pulse shaping, we use a dark spectrum measurement where the mean value is used for the factor μ . In a light yield measurement, the signal is the sum of the detected photons and the noise. Pixels fired by light reduce the noise contribution by a factor P_{free} with respect to the measurement taken in the dark. Since the signal cluster is several channels wide, the contribution of DCR is increased by the average size of clusters l .

5.4.2 Light yield at -40°C

The light yield was measured with an H2017 detector operated over a wide ΔV -range at room temperature and at -40°C . The read-out is performed with VATA64 configured with a long shaping time $\tau_{\text{shaping}} \approx 300$ ns. To correct the light yield values for the contribution of correlated noise, we compute the mean additional charge in the same way as the factor r_{curr} in

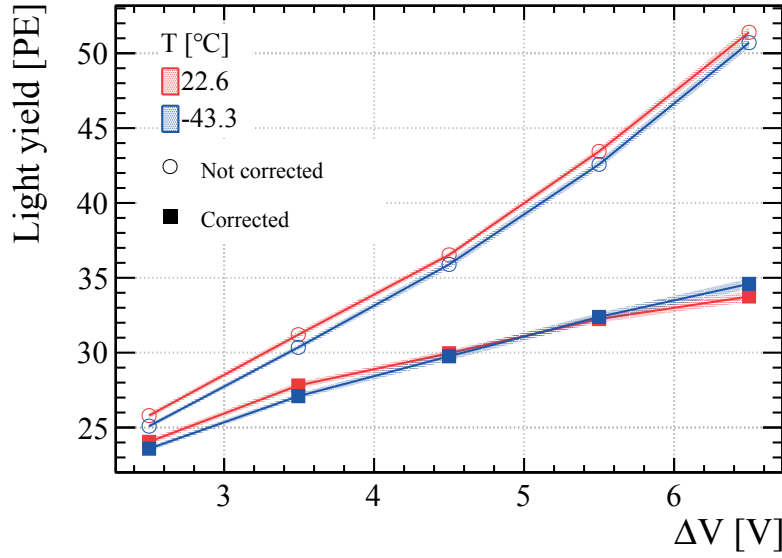


Figure 5.8 – Light yield of the short fibre module as a function of ΔV measured with an H2017 detector and VATA64 electronics at room temperature and at -40°C . The two sets of curves represent the light yield before (circles) and after (squares) correction for the correlated noise.

the PDE measurement described in section 4.4.2. Using the results obtained in section 4.2.3, we compute r_{curr} and apply the correction on the light yield. Note that the contribution from DCR is negligible due to the low f_{DCR} . The light yield, before and after the correction, is shown in figure 5.8. The two curves after correction are compatible within $\pm 2\%$ and, therefore, we conclude that the PDE, integrated over the emission spectrum of the fibres, does not change substantially over the measured temperature range.

5.4.3 Light yield with irradiated H2017 detectors

To measure the PDE of irradiated detectors, we compare the light yield of non-irradiated and irradiated SiPMs operated simultaneously in identical conditions. The error on the light yield (combining the data of 128 channels) introduced by non-uniformities in the fibre mat was measured to be 3% using a reference SiPM array placed at all test positions. To validate the procedure for irradiated detectors, the test is performed using the non-irradiated SiPM and random pulses produced by a continuous light source. The light yield measurement comprises two steps: the scan with the electron-gun and a measurement in the dark to calculate the corrections.

Signal conversion to PE We have observed a shift of the pedestal at large bias current which is explained by a change in the DC level at the SPIROC input. This effect can be suppressed up to a bias current of $10\ \mu\text{A}$ per channel by a recalibration during the measurement with electrons. For larger currents, the error remains below 1 PE. The ADC gain measurement from the PE peaks in the electron spectrum is possible for the detectors irradiated at 3 and $6 \cdot 10^{11}\ \text{1 MeV n}_{\text{eq}}/\text{cm}^2$. We observe a reduction of the ADC gain with respect to the non-irradiated detector of approximately 5%, compatible with the measurement from low light injection. For the detector irradiated to $12 \cdot 10^{11}\ \text{1 MeV n}_{\text{eq}}/\text{cm}^2$, the gain values from the

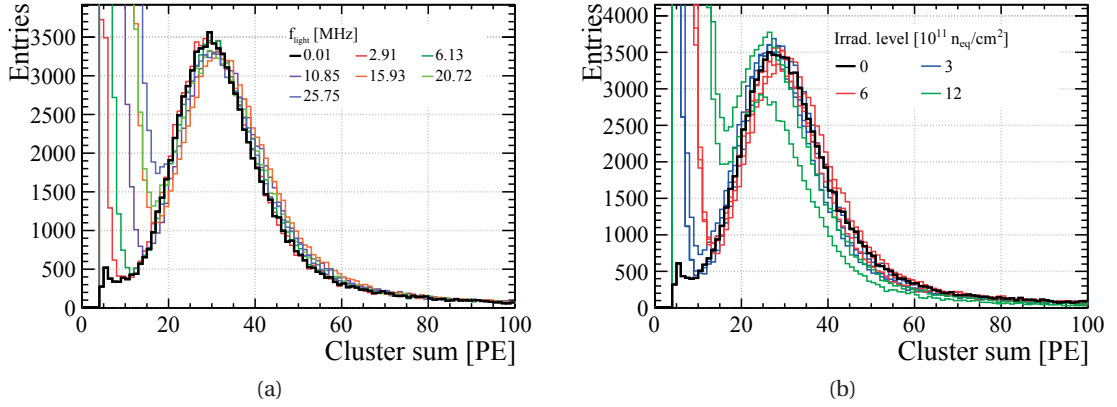


Figure 5.9 – Cluster sum distribution for electrons injected in the fibre module measured with a non-irradiated (left) and irradiated (right) H2017 detectors at $\Delta V = 3.5V$ and SPIROC read-out. The large number of clusters with small sum is due to noise and is enhanced by the scanning procedure.

$6 \cdot 10^{11} \text{ 1 MeV n}_{\text{eq}}/\text{cm}^2$ device are used for the clustering algorithm.

Validation of the method The cluster sum distribution measured for a non-irradiated detector illuminated with continuous light is shown in figure 5.9a. We find a light yield of 29.6 PE with no significant changes at the different noise levels.

The clusters situated close to the MPV of the distribution (sum of 30 ± 1 PE) have an average size of $l = 3$ channels. In a first approximation, the number of photons per channel is $N_{\text{PE}/\text{ch.}} = 10$. The fraction of available pixels is approximately given by $P_{\text{free}} = (N_{\text{pixels}} - N_{\text{PE}/\text{ch.}})/N_{\text{pixels}} = 90.5\%$. Using a dark spectrum taken at each noise level, we can evaluate μ and obtain the average contribution from the DCR using equation 5.1. The light yield values from figure 5.9a, corrected for DCR, are all within $\pm 3\%$ of the value measured without additional noise. The interpretation is that the large increase in DCR does not bias the results and the method can be applied up to $f_{\text{DCR}} = 25 \text{ MHz}$ ($70 \text{ MHz}/\text{mm}^2$). The uncertainty on the measurement is $\pm 3\%$.

Irradiated SiPMs The light yield with irradiated H2017 SiPMs was measured between $\Delta V = 2.0$ and $4.5V$ and at -40°C . The cluster sum distribution at $\Delta V = 3.5V$ is displayed in figure 5.9b. Up to the highest neutron fluence, the distribution shows a clear MPV peak well separated from the noise at low values. For the devices irradiated to 3 and $6 \cdot 10^{11} \text{ 1 MeV n}_{\text{eq}}/\text{cm}^2$, the light yield corrected for the DCR contribution is compatible with the non-irradiated detector within $\pm 4\%$ which is within the expected uncertainties (mat non-uniformity, DCR correction). For the devices irradiated to $12 \cdot 10^{11} \text{ 1 MeV n}_{\text{eq}}/\text{cm}^2$, a 3% difference in light yield is observed at $\Delta V = 2V$ which is compatible with an unchanged PDE. At higher ΔV , a large difference is seen (up to 20% reduction at $\Delta V = 4V$) which can be explained by the limitations introduced by the front-end electronics (V_{bias} shift, pedestal shift, DCR correction).

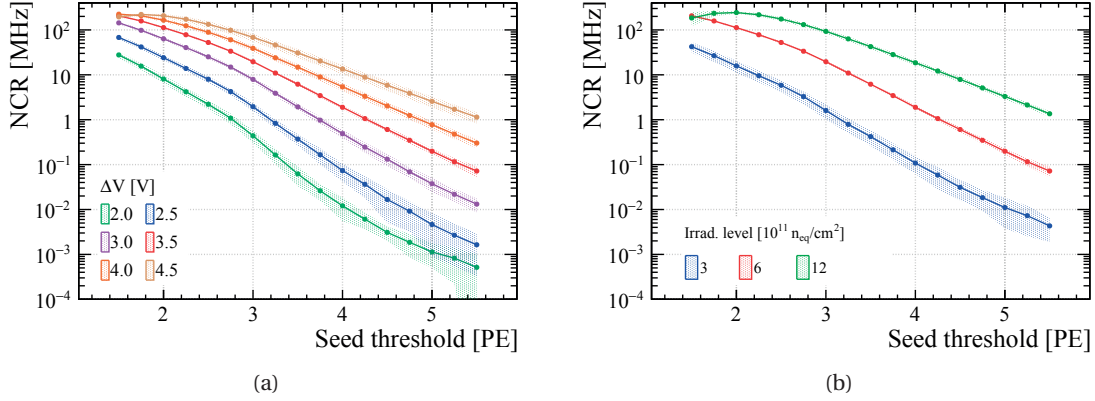


Figure 5.10 – Noise cluster rate of H2017 detectors, recorded with SPIROC, plotted as a function of seed threshold. Results for the devices irradiated to $6 \cdot 10^{11} \text{ 1 MeV } n_{\text{eq}}/\text{cm}^2$ (left) and for three different irradiation levels at fixed $\Delta V = 3.5 \text{ V}$ (right). The error bands correspond to the min-max difference between all tested devices. The neighbour (sum) threshold is set to seed $- 1 \text{ PE}$ (seed $+ 2 \text{ PE}$).

5.5 Noise cluster rate

Using the fibre module setup, irradiated H2017 detectors are tested in the dark at -40°C for the measurement of the noise cluster rate (NCR). For a 128-channel SiPM array read out at 40 MHz (LHC bunch crossing frequency), it is given by:

$$f_{\text{NCR}} = \frac{N_{\text{NC}}}{N_{\text{ev}}} \cdot 40 \text{ MHz} \quad (5.2)$$

where N_{NC} is the number of noise clusters and N_{ev} is the number of events. The NCR strongly depends on the clustering thresholds, the DCR, the correlated noise and the electronics shaping time.

5.5.1 Measurements with SPIROC

The NCR decreases exponentially with the clustering thresholds as shown in figure 5.10. At the low thresholds and high irradiation level, we observe a saturation of the rate due to the merging of noise clusters.

In figure 5.11, the NCR of different irradiated SiPMs is plotted as a function of the DCR. To separate the influence of DCR and correlated noise on the NCR, we draw the lines of constant ΔV which is equivalent to constant correlated noise. For DCR above 10 MHz, the separation between the lines is small which indicates that, for the generation of clusters, the random overlap of dark pulses in the shaping time dominates over correlated noise. Decreasing the DCR, the separation increases which shows that the influence of correlated noise becomes more important. The NCR expected in the absence of correlated noise is estimated from a simulation. Assuming a square integration window of $\tau_{\text{int}} = 40 \text{ ns}$ and a Poisson distributed number of dark pulses in 128 channels, we simulate noise clusters and

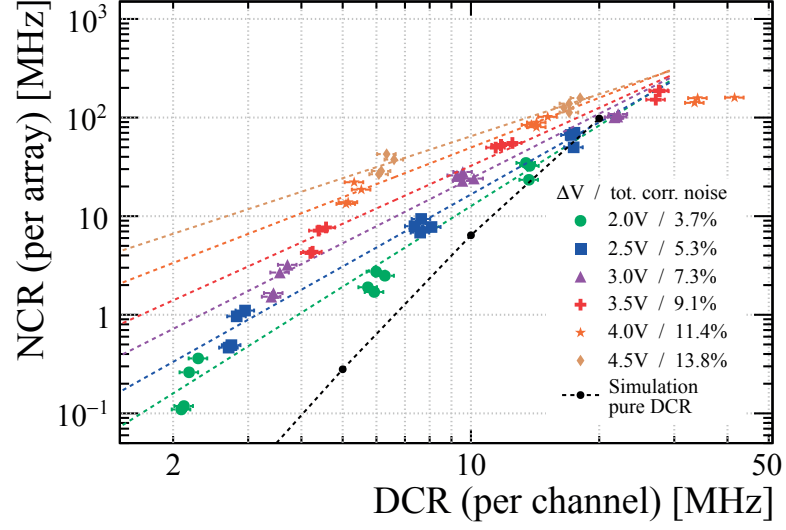


Figure 5.11 – Noise cluster rate as a function of DCR at different ΔV for irradiated H2017 SiPMs. At each ΔV , a fit with a function of type $f_{\text{NCR}} = \alpha \cdot (f_{\text{DCR}})^\beta$ is performed.

compute their probability. As shown in the figure, the reduction in NCR at low DCR is much steeper than in the presence of correlated noise. These results demonstrate that the correlated noise, even at occurrence probability below 10%, is a non-negligible source of noise clusters. With shorter integration time as in the PACIFIC, we expect the correlated noise to be the dominant source.

5.5.2 Simulation based on SPIROC measurements

Using the dark measurements taken with SPIROC, we have performed a noise cluster simulation. It is based on the generation of an array of 128 signals from the dark spectrum. A cross-talk between neighbouring channels is also simulated. For each PE generated in one channel, we give a probability $p_{\text{Ch.XT}}$ that it creates another PE in the left and right channels. Performing this simulation for detectors irradiated at 3, 6 and $12 \cdot 10^{11} \text{ 1 MeV n}_{\text{eq}}/\text{cm}^2$, we find that a cross-talk in the order of 2% is necessary to reproduce the rate and size of noise clusters. The cross-talk increases with ΔV ; we observe $p_{\text{Ch.XT}} = 1 - 2\%$ at $\Delta V = 2.5\text{V}$, $p_{\text{Ch.XT}} = 2\%$ at $\Delta V = 3.5\text{V}$ and $p_{\text{Ch.XT}} = 3\%$ at $\Delta V = 4.5\text{V}$. It does however not depend on the irradiation level.

5.5.3 Simulation based on waveform measurements

We developed a simulation for the estimation of the noise cluster rate at different integration time lengths. It is based on waveforms from irradiated detectors operated at -40°C recorded over $50 \mu\text{s}$ (100 ps resolution) using the setup introduced in section 4.2.1. The dark spectrum for different τ_{int} can be extracted from the numerical integration of short segments of the waveform with duration τ_{int} . The integral values are scaled with respect to the 1 PE-charge measured in the pulse shape analysis. To form noise clusters, the dark spectrum is used to generate an array of 128 random signals and the clustering algorithm is applied. In this procedure,

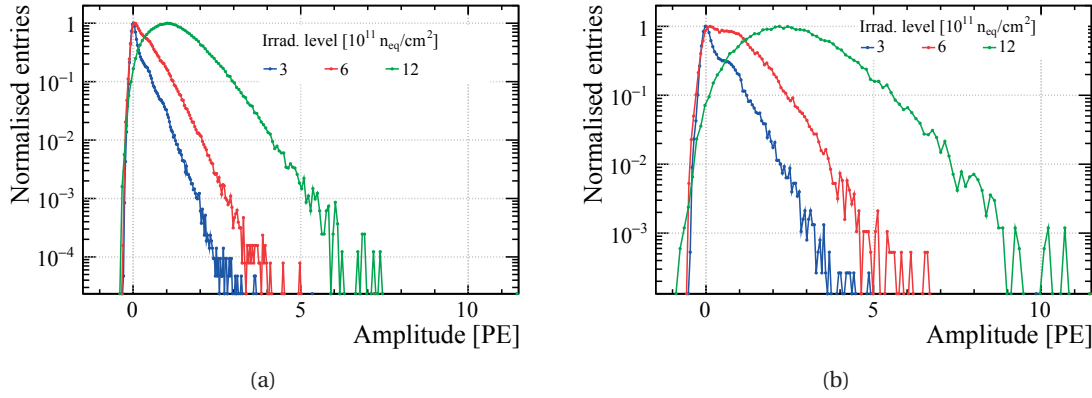


Figure 5.12 – Dark spectrum for irradiated detectors operated at $\Delta V = 2.5\text{ V}$ and -40°C obtained from a numerical integration of long waveforms with $\tau_{\text{int}} = 20\text{ ns}$ (left) and $\tau_{\text{int}} = 100\text{ ns}$ (right).

cross-talk between channels is added to the random signals, as discussed previously.

The setup allows to bias either a single channel or all channels of the SiPM array. We notice a significant increase in DCR (30% at $\Delta V = 5.0\text{ V}$) when all channels are biased. This can be explained by the generation of photons in the avalanches and their reflection at the optical surface. No change in DCR is however seen with a black absorber placed on the SiPM entrance window. In the measurements acquired with the SPIROC and the fibre module where the SiPM entrance window is in contact with the fibres (similar refractive indexes), reflections can be neglected. To compare the results, we use the data with a single channel biased.

The dark spectrum obtained for irradiated detectors and two different integration time lengths is shown in figure 5.12. At an irradiation level of 6 and $12 \cdot 10^{11} \text{ MeV n}_{\text{eq}}/\text{cm}^2$, the random overlap of the slow pulse component leads to a significant baseline fluctuation. The resulting shift in the pulse integral spectrum can be typically in the order of a few PEs. In contrast, the measurements with SPIROC show a small shift (below 1 PE) of the baseline (pedestal) to the negative region (see section 5.4.3). Hence, the negative part of the SPIROC shaping (see figure 5.2) enables to suppress the slow SiPM pulse component and to avoid significant baseline shifts. In the following, we restrict our discussion to the lowest irradiation level where the absence of baseline shift enables the comparison with the SPIROC^b. Note that in the PACIFIC read-out, the pole-zero cancellation is adjusted to filter the slow pulse component preventing this random overlap. On the contrary, with the VATA64 chip, the long shaping time and the absence of negative part in the shaping result in very large baseline shift.

The comparison of the dark spectrum at $3 \cdot 10^{11} \text{ MeV n}_{\text{eq}}/\text{cm}^2$ from the waveform integration and the SPIROC measurement, displayed in figure 5.13, shows a satisfactory agreement with an integration time between $\tau_{\text{int}} = 40$ and 100 ns . The matching fails however at high amplitude which can be explained by the contribution of the shaping time in the SPIROC measurement.

^b To extend this method to the higher irradiation levels, we suggest to use a filtering method such as the one described in [87] or in [88, 89] (see discussion in section 4.2.5). Filtering can be either implemented in hardware or in the offline processing.

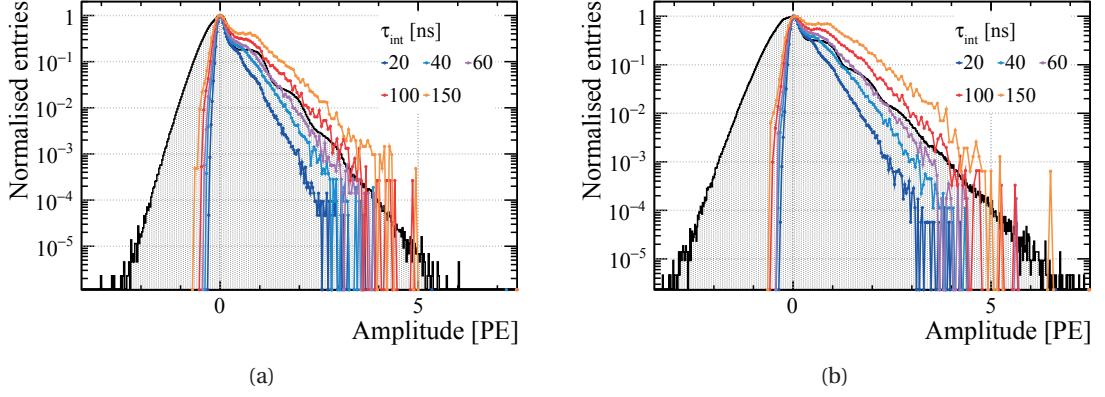


Figure 5.13 – Comparison between the dark spectrum of a detector irradiated to $3 \cdot 10^{11} \text{ 1 MeV } n_{\text{eq}}/\text{cm}^2$ at $\Delta V = 2.5 \text{ V}$ (left) and $\Delta V = 3.5 \text{ V}$ (right) obtained from numerical integration of waveforms and from measurements with SPIROC (shown in black).

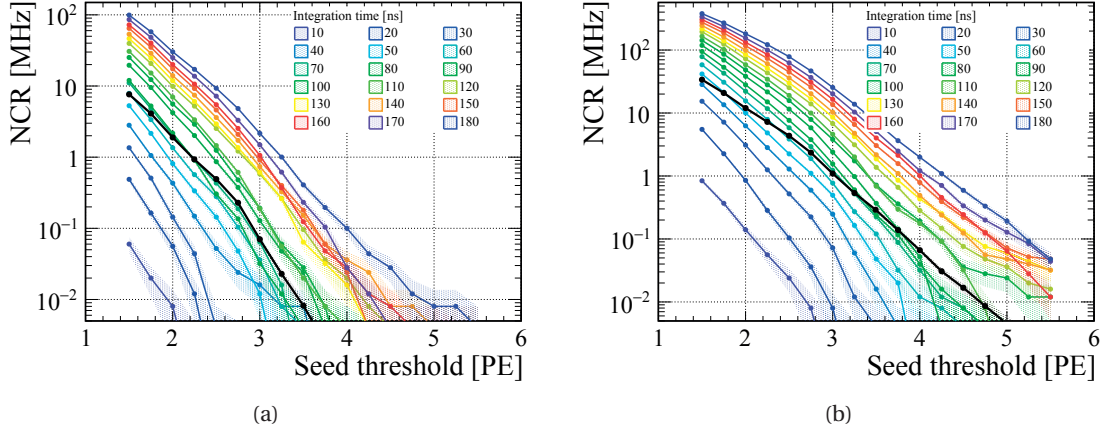


Figure 5.14 – Noise cluster rate as a function of seed threshold for a detector irradiated to $3 \cdot 10^{11} \text{ 1 MeV } n_{\text{eq}}/\text{cm}^2$ operated at $\Delta V = 2.5 \text{ V}$ (left) and $\Delta V = 3.5 \text{ V}$ (right) obtained from the simulation and compared to the SPIROC measurement (in black). In the simulation, a cross-talk between channels of 1% (2.5 V) and 2% (3.5 V) is added.

We simulated noise clusters for different integration time lengths and different clustering thresholds. As shown in figure 5.14, we observe a good agreement with the SPIROC at $\Delta V = 2.5 \text{ V}$ for an integration time of 60 to 70 ns. At $\Delta V = 3.5 \text{ V}$, the exponential decrease is more pronounced in the simulation than in the measurement as expected from the mismatch between the dark spectra at high amplitudes. Figure 5.15 shows that the NCR has a strong dependence on the integration time. In the region from $\tau_{\text{int}} = 50$ to 10 ns, the NCR drops by several orders of magnitude. This emphasizes the importance of the integration time length for the operation of irradiated detectors. At $\Delta V = 3.5 \text{ V}$, the estimated NCR is below 1 MHz for $\tau_{\text{int}} < 40 \text{ ns}$ for a seed threshold of 2.5 PE.

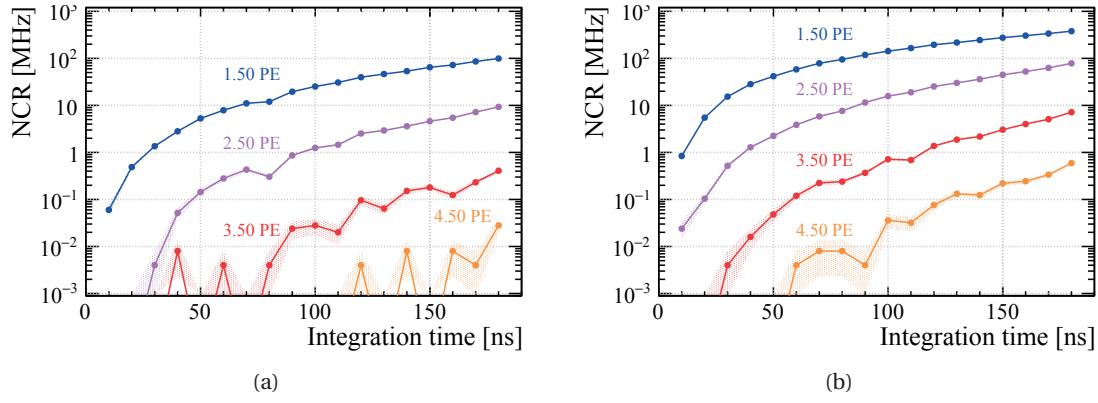
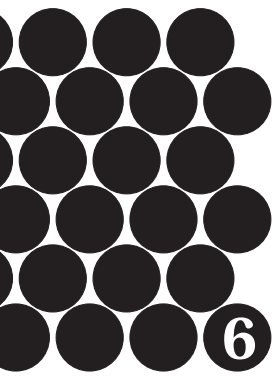


Figure 5.15 – Noise cluster rate as a function of integration time for a detector irradiated to $3 \cdot 10^{11} \text{ 1 MeV n}_{\text{eq}}/\text{cm}^2$ operated at $\Delta V = 2.5\text{V}$ (left) and $\Delta V = 3.5\text{V}$ (right) obtained from the simulation with a cross-talk between channels of 1% and 2%, respectively. The NCR is calculated for different clustering thresholds (seed threshold indicated on the figure).



6 Scintillating fibre tracker for LHC beam monitoring

The beam gas vertex (BGV) detector is a beam monitor under development for the high-luminosity LHC [99]. It aims at providing non-disruptive beam profile measurements with 5% resolution within 1 minute to allow monitoring the beam during the accelerator energy ramp and life cycle. It is based on the measurement of the tracks originating from inelastic beam-gas interactions and the reconstruction of the vertices. During the early R&D period of the LHCb SciFi tracker, a demonstrator based on the SciFi technology was developed and installed at the LHC. It instruments only one of the proton beams and comprises eight SciFi tracker modules which have been developed and constructed by EPFL and RWTH Aachen. [100, 101, 102]

In this chapter, we give an overview of the detector principle and design. The optimisation of the read-out electronics is presented in detail. The results of the characterisation of a fibre module at a test beam are summarised. Recent developments on the data analysis for the measurement of the beam size have led to promising results. A summary of the measurement techniques used in the current detector is given in appendix C.

6.1 The beam-gas vertex demonstrator

The reconstruction of beam-gas vertices for the measurement of beam characteristics and the calibration of luminosity was first performed at LHCb using residual or injected gas in the VELO detector [103, 104, 105]. In the light of the results, it was decided to develop a dedicated instrument for the accelerator providing real-time beam profile measurements with single-bunch resolution. The beam size results from the emittance, which is a property of the beam, as well as the β -function and the dispersion from the magnets, which strongly depend on the position in the accelerator. With the knowledge of the β -function and the dispersion, the beam size measurement allows to calculate the emittance, an important performance parameter of the LHC.

As shown in figure 6.1 and 6.2, the BGV demonstrator, installed in November 2015 at point 4, comprises a gas tank placed in the beam trajectory and two tracking stations. The tank is filled with neon which provides an interaction rate of approximately 100 Hz per bunch in nominal conditions. The gas pressure can be tuned to accommodate the luminosity and the beam energy. One transversal wall of the tank serves as exit window for the particles produced by the

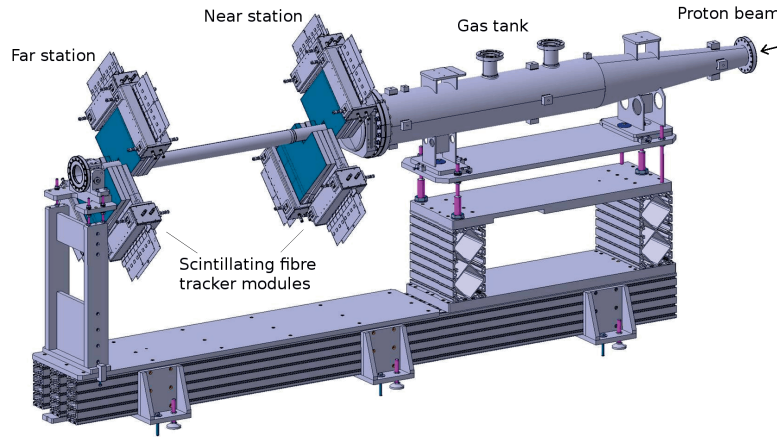


Figure 6.1 – Schematic view of the BGV demonstrator. Image from the BGV collaboration.

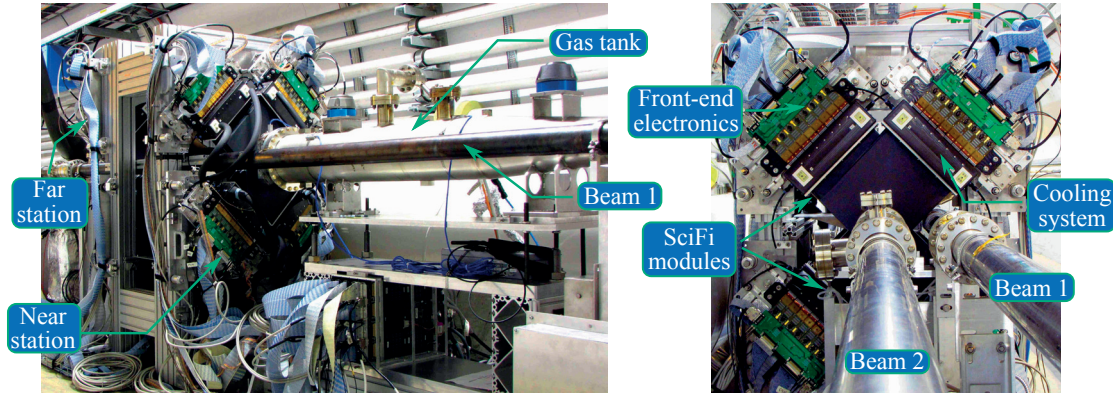


Figure 6.2 – Pictures of the BGV detector after installation in November 2015. Side view including the gas tank (left) and front view of the far station (right).

interactions. Its material and design are optimised in order to minimise the effect of multiple scattering. The tracks are measured by two stations separated by 1 m and comprising two pairs of SciFi modules placed above and below the beam pipe. Within a pair, the modules' fibres are oriented perpendicularly in order to obtain the two-dimensional track coordinate. The modules themselves consist of two detection planes with a stereo angle of 2° which allows for ghost hit rejection. The active area is $260 \times 340 \text{ mm}^2$ per plane with a $97 \times 97 \text{ mm}^2$ cut-out at one of the corner. The cut-out enables to enhance the coverage for tracks close to the beam pipe. The fibre mats are made with 4 or 5 layers and are equipped with a mirror. The material budget of a module (two detection planes) is $X/X_0 = 0.94$ and 1.05% for 4- and 5-layer mats, respectively, where the active material (fibres) represent $X/X_0 = 0.56$ and 0.67% . [100, 101]

The trigger is provided by the coincidence of two scintillator stations located just after the second tracking station and 3 m downstream. To ensure that the triggered particles originate from the gas target, a veto station is implemented upstream of the tank. The trigger subsystem allows to evaluate the relative bunch intensity and the ghost charge fraction (i.e. the charge at nominally empty bunches) with systematic errors in the order of 0.3% . [101]

The fibre modules are made of the Kuraray SCSF-78MJ fibres, identical to the LHCb SciFi, and

are read out by 128-channel SiPM arrays of type H2014 [106] with a total of 16k channels. The simulation of the expected radiation environment predicts an ionising dose of 16 Gy/year at the photodetectors location [107]. The cumulated dose is monitored using PIN diodes [82] that are placed close to the SiPMs on the modules and is measured to be 75 Gy in June 2018 [108]. In order to reduce the DCR, the SiPMs can be operated cold (down to -40°C) using a cooling system based on a liquid circulating chiller [109, 110]. To achieve homogeneous response among all SiPMs, a selection based on the breakdown voltage was made and groups of four devices were attached to the same bias voltage. For the V_{BD} determination, we used the method described in section 5.3 with VATA64 electronics. The average spread of the mean- V_{BD} among groups of four SiPMs is generally below 0.1 V ($\delta G/G < 3\%$ at $\Delta V = 3.5\text{V}$)^a.

The conceptual design of the modules concerning fibre planes, dimensions, mechanical support and cooling was developed at EPFL in view of the LHCb SciFi project. The manufacturing was split between RWTH Aachen and EPFL. The front-end read-out electronics was developed at EPFL. The assembly of the module components including mirror gluing, SiPM alignment, light shielding and front-end electronics mounting was performed at EPFL. A scan of the light yield was carried out for all modules using the electron-gun setup introduced in section 5.1. Forty-three broken channels due to disconnected or shorted channels on the front-end board or on the SiPM flex cable assembly were detected which corresponds to less than 0.3% of all read-out channels.

6.2 Fibre module read-out

The electronic read-out of the BGV SciFi modules is based on the Beetle ASIC developed for the silicon strip detectors of LHCb. This chip allows for a 40 MHz read-out synchronous to the LHC bunch structure. The output of the chip is implemented as four analogue links (A-links) with analogue amplitude encoding of the data and pseudo-digital encoding of the header information (4 headers and 32 channel samples). The A-link data is transmitted to a repeater board placed close to the detector before transmission over 60 m cables. The data is sent to the TELL1 acquisition board [111] where it is digitised with a 10 bit ADC. One BGV fibre module (2048 channels) is read out by 16 SiPMs, 16 Beetle chips, one repeater board and one TELL1.

The Beetle chip was designed to receive small signals ($22 \cdot 10^3$ electrons/MIP) from silicon strip detectors. A new front-end board was designed to adapt the larger SiPM signals (in the range of 10^7 electrons/MIP) to the Beetle dynamic range. For each channel, the board contains an RC-circuit providing an attenuation factor of 300.

Extensive studies of all noise and signal distortion introduced in the read-out chain have been performed [3, 112]. This leads to correction algorithms that have been implemented in the data processing FPGA of the TELL1. In addition to the pedestal (discussed in section 5.2), two other sources of noise were identified. The header information present in each A-link influences the neighbouring channel samples by an inter-symbol cross-talk. The observed effect is a significant change of the baseline in the two first transmitted data channels. Common

^a In five cases, the spread is however larger (up to 0.6 V, $\delta G/G < 17\%$ at $\Delta V = 3.5\text{V}$). The SiPMs were nevertheless assembled together because of schedule constraints.

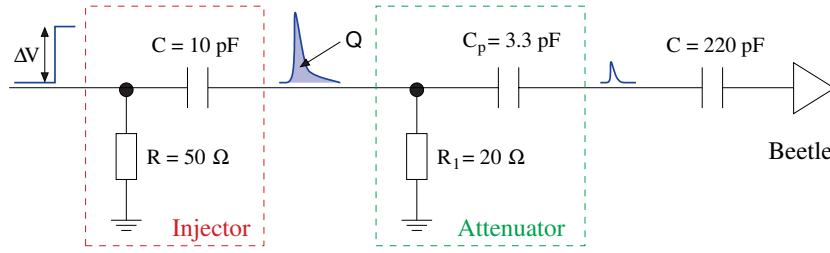


Figure 6.3 – Signal injector circuit connected to one input channel of the Beetle board.

mode noise is another effect introduced by the read-out chain. It is observed as a shift of the baseline of an A-link on an event per event basis due to electromagnetic interferences. The corrections for the BGV fibre modules are described in more details in [113]. We observe a cross-talk between channels due to a small capacitive coupling between neighbouring signal transmission lines on the front-end PCB. We present here the validation of a correction algorithm with offline data analysis and discuss shortly the implementation of the zero-suppression in the TELL1 data processing.

6.2.1 Characterisation of the front-end electronics

A charge injector board with 128 channels was developed in order to characterise the read-out electronics (see figure 6.3). The injector consists of an RC -circuit with $R = 50\ \Omega$ and $C = 10\ \text{pF}$. With a fast voltage step ΔU , a charge comparable in time and amplitude to an SiPM pulse is produced. The charge generated for each photon detected in an H2014 SiPM at $\Delta V = 3.5\ \text{V}$ is $Q = G \cdot e \approx 0.55\ \text{pC}$ whereas the injector produces $Q/\Delta U = C = 10\ \text{pC/V}$. Therefore a 550 mV step at the injector produces a charge equivalent to ten photons.

The pulses from SiPM and injector have different spectral content. The injector leads to a single exponential decay with $\tau = R \cdot C = 0.5\ \text{ns}$ whereas SiPM pulses comprise a fast and slow component with $\tau_{\text{short}} < 1\ \text{ns}$ and $\tau_{\text{long}} = 22\ \text{ns}$. Due to the frequency dependence of the attenuator on the front-end board, the response of the electronics is different for an SiPM or an injector pulse, as shown in figure 6.4a. The response of the Beetle was measured for different injection amplitudes. As seen in figure 6.4b, large saturation is present for signals with amplitude above 10 PE.

6.2.2 Channel cross-talk

We observe a correlation between signals of nearby channels on the front-end PCB. The correlation is directional, i.e. a signal cross-talk produced in channel y due to channel x does not imply the same effect from y to x . As explained in figure 6.5, this type of cross-talk is due to the capacitive coupling of routing lines where a $300\times$ attenuated signal is transmitted next to a non-attenuated one. We define the *aggressors* and the *victims* as the channels that give and receive a correlation, respectively. We introduce a correlation factor measured by:

$$\chi_{\text{aggressor} \rightarrow \text{victim}} = \frac{A(\text{victim})}{A(\text{aggressor})}, \quad (6.1)$$

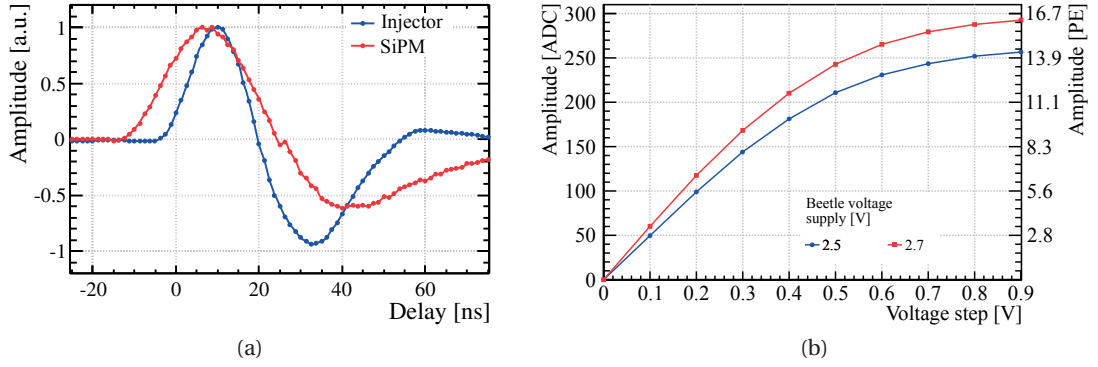


Figure 6.4 – BGV front-end electronics response. Pulse scan measured at the Beetle output for signal injected with SiPM and injector board (left). Pedestal-subtracted signal for different injected pulse amplitudes (right). The right-axis gives the equivalent number of PE.

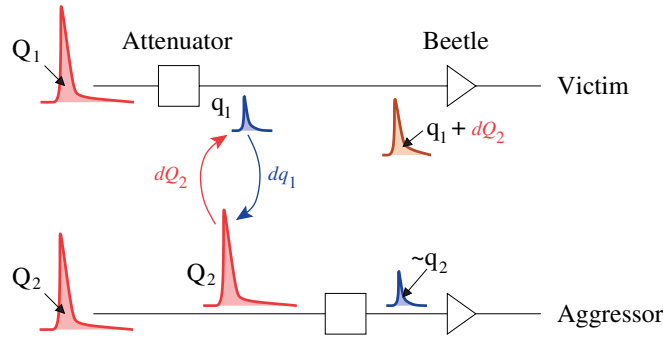


Figure 6.5 – Principle of cross-talk between two read-out channels. The raw input signals $Q_{1,2}$ are attenuated at distinct locations on the PCB. The electrical coupling between the lines leads to a cross-talk between the attenuated signal q_1 and the raw signal Q_2 . The contribution dQ_2 from the non-attenuated signal yields a significant additional charge to q_1 .

where A is the signal amplitude^b upon injection in the aggressor channel. An example of an injection test is shown in figure 6.6a.

We classify the observations in two categories: left- and right-correlations. A systematic correlation of approximately -25% with the direct left neighbour arises due to an inter-symbol cross-talk between the channels in the serialised A-link data. As shown in figure 6.6b, the correlation factor is independent of the aggressor amplitude. Right-correlations are observed between distant channels and are due to the capacitive coupling between adjacent lines on the front-end PCB. The cross-talk dQ to a victim increases linearly with the aggressor charge Q . However, due to the Beetle saturation, the output is not proportional to the input charge at high signal. This results in a non-constant correlation coefficient as shown in figure 6.6b.

We have measured the correlation from injection tests using $\Delta U = 200$ mV in all channels of several front-end boards. We observe a repetition period of eight channels for the right-correlations which is explained by the geometrical repetition pattern of the attenuators on the front-end board. In the measurements, the left-correlations were caused by a non-ideal cable

^b Signals are corrected for the pedestal, the header influence and the common mode noise.

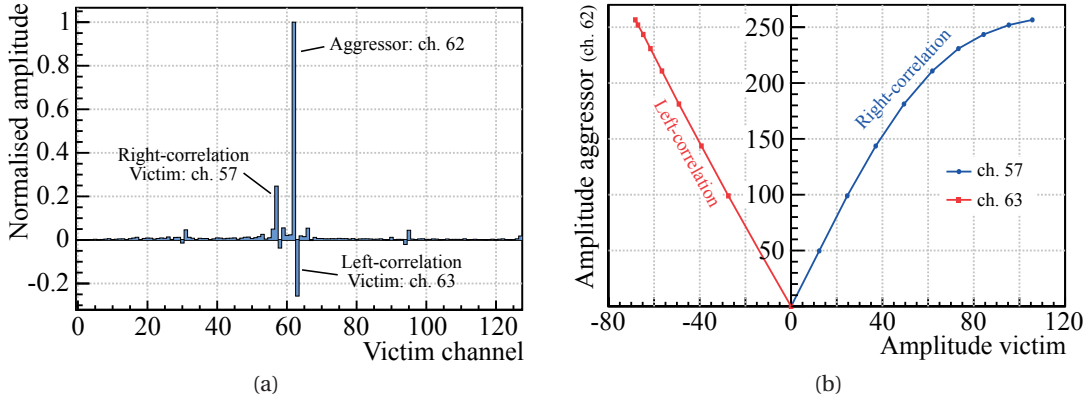


Figure 6.6 – Channel correlation revealed by injection in a single channel of a front-end Beetle board (left) and measurement of the correlation as a function of the injection amplitude (right).

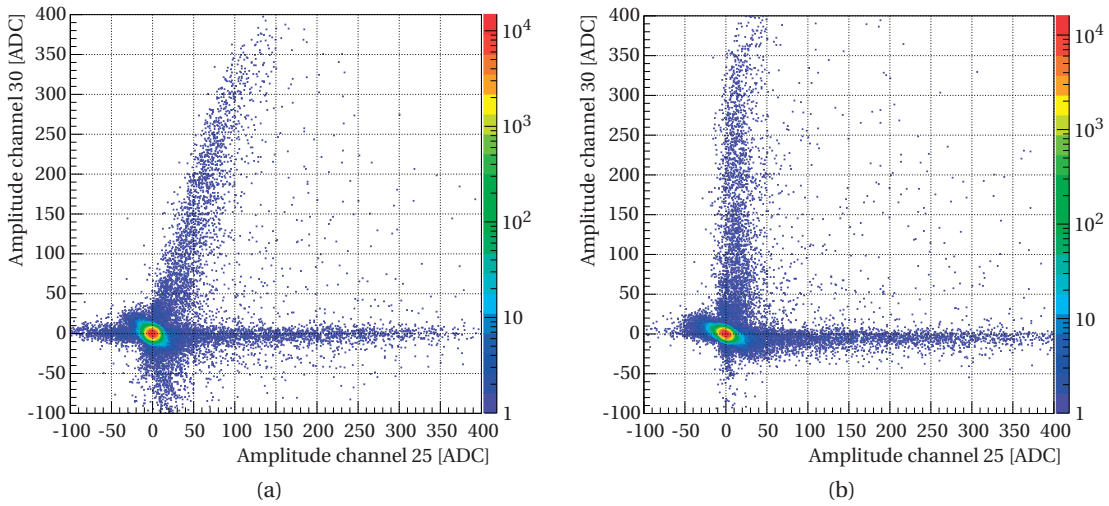


Figure 6.7 – Correlation between signals from two distant channels measured with electrons injected in a fibre module. Before (left) and after (right) correction for the right-correlation.

compensation which was corrected in the BGV detector. For right-correlations, a correction algorithm is implemented as:

$$A(\text{victim}) \longrightarrow A(\text{victim}) - x_{\text{aggressor} \rightarrow \text{victim}} \cdot A(\text{aggressor}). \quad (6.2)$$

Note that using a constant correlation factor, the correction is insufficient for high aggressor signal. For validation, the algorithm was applied to data from fibre modules taken with the electron-gun setup. The effect of right-correlation is shown in the example of figure 6.7a where a high signal in channel 30 gives always rise to a non-zero signal in channel 25. After applying the correction (figure 6.7b), the influence of channel 30 is significantly reduced. In the following sections, the effect of channel correlation on clusters will be discussed.

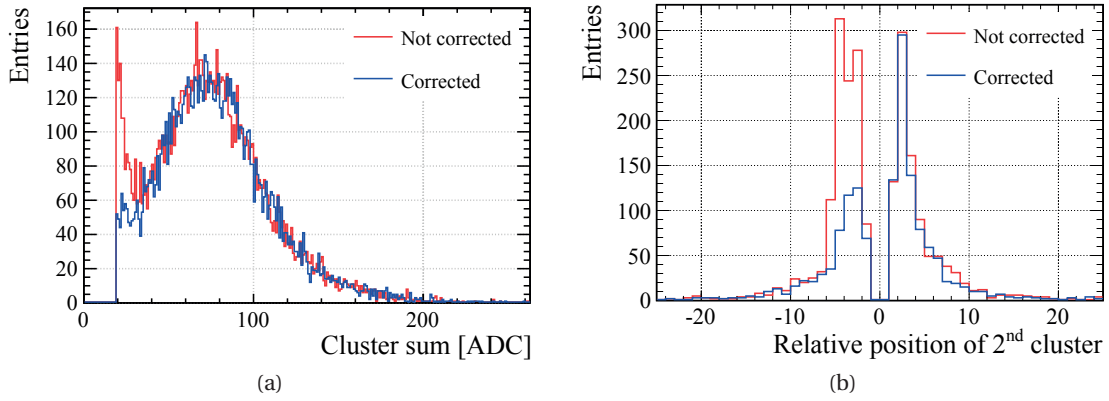


Figure 6.8 – Impact of the channel correlation correction on the distribution of cluster sum (left) and of secondary cluster position (right). The measurement was taken with the electron-gun setup on a BGV module with 4 fibre layers and SiPMs at $\Delta V = 3.5\text{ V}$.

6.2.3 Zero-suppression implementation in the TELL1

The data processing implemented in the TELL1 for the read-out of the VELO [114] was adapted for the BGV fibre modules to perform in real-time the raw data corrections and the clustering. The corrections for the pedestal, header influence and common mode noise do not need any modification with respect to the VELO implementation. Some algorithms such as FIR filter and channel reordering were removed and the polarity of the signals was inverted. A simple processing for the correction of right-correlations was implemented taking into account correlations above 10%. Such large correlations occur only between certain channels as $\text{ch}+3 \rightarrow \text{ch}$ and $\text{ch}+5 \rightarrow \text{ch}$. For each read-out channels, we introduce two configurable coefficients $x_{\text{ch}+3 \rightarrow \text{ch}}$ and $x_{\text{ch}+5 \rightarrow \text{ch}}$ and the correction is applied as:

$$A(\text{ch}) \longrightarrow A(\text{ch}) - x_{\text{ch}+3 \rightarrow \text{ch}} \cdot A(\text{ch}+3) - x_{\text{ch}+5 \rightarrow \text{ch}} \cdot A(\text{ch}+5). \quad (6.3)$$

The clustering algorithm of the VELO and the SciFi are almost identical. The spill-over bit in the VELO clustering was changed into a hard cut corresponding to the cluster sum. The cluster position is encoded in an $(11 + 3)$ -bit information providing the channel number and an inter strip position precision of $1/8$ corresponding to $31\text{ }\mu\text{m}$. Figure 6.8a presents the cluster sum distribution of a 4-layer BGV module measured in the laboratory with the electron-gun setup. Figure 6.8b shows the position distribution of secondary clusters relative to the primary cluster. Secondary clusters can arise in the setup from multiple scattering or bremsstrahlung of the electron at the exit of the electron-gun. In addition, right-correlations also generate clusters three or five channels away from the primary cluster. These ghosts have typically low sum and are efficiently removed by applying the correction for right-correlation. Note that the remaining asymmetry in the position distribution is due to left-correlations which are not taken into account.

The clustering thresholds in the BGV detector were optimised to provide a high hit detection efficiency. To obtain a uniform response, the seed and neighbour thresholds can be adjusted for each channel separately while the sum threshold for groups of 64 channels. We chose

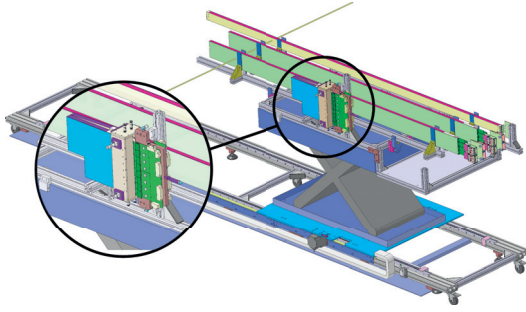


Figure 6.9 – Schematic view of the mounting of the BGV module (zoom) on the xy -moving table allowing to perform scans in the beam.

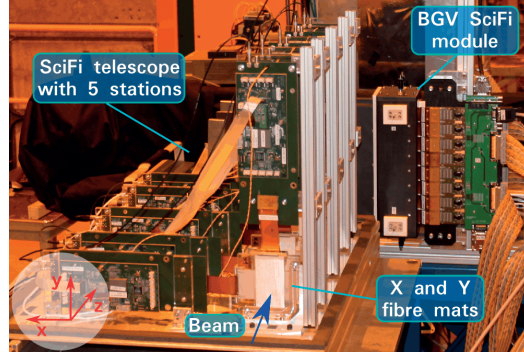


Figure 6.10 – Picture of the setup with the SciFi telescope placed upstream of the BGV fibre module.

to adjust the thresholds per SiPM (128 channels) to provide a uniform distribution of noise clusters from DCR. In the nominal operation conditions of 2017 (SiPMs at $T = -10^\circ\text{C}$ and $\Delta V = 3.5\text{V}$), setting the thresholds to approximately 1.5-2.0 PE (seed threshold) leads to 1.5 noise clusters per module (2048 channels, two detection planes) and per event. This level of noise does not impede the pattern recognition whereas the low thresholds ensure a high detection efficiency, as it is demonstrated in section 6.3.4.

6.3 Characterisation of a fibre module at test beam

A 4-layer fibre module was tested in the experimental setup of the LHCb SciFi tracker test beam at SPS in November 2015. The goal of the measurement campaign was to determine the hit resolution and detection efficiency. In this section, we summarise the analysis methods and the main results. More details are given in [115].

6.3.1 Experimental setup

The module is mounted on an xy -table as shown in figure 6.9, allowing to inject the beam at different positions. The two sides have fibres oriented straight and with 2° -rotation compared to the horizontal (called 0° - and 2° -side, respectively). The setup includes a telescope used to reconstruct the track of particles and made of five tracking stations with x and y measurements based on short scintillating fibre mats [116]. It is placed approximately 20 cm upstream of the BGV module as shown in figure 6.10.

The beam is composed of a mixture of 180 GeV/c pions, protons and muons. The deflection angle from multiple scattering is well described by a Gaussian function with increased tails for large scattering angles. Inside the telescope, the beam only crosses fibre mats with a total thickness of $X/X_0 \approx 3\%$. The transverse deviations resulting from multiple scattering are in the order of $4\text{ }\mu\text{m}$ in the telescope and $6\text{ }\mu\text{m}$ extrapolated to the BGV module. The fibre module represents a total thickness of $X/X_0 \approx 1\%$ leading to transverse deviations below $1\text{ }\mu\text{m}$ between the two planes. Multiple scattering is therefore negligible for the foreseen measurements given the expected resolution of SciFi modules ($50\text{ }\mu\text{m}$). The beam was tuned

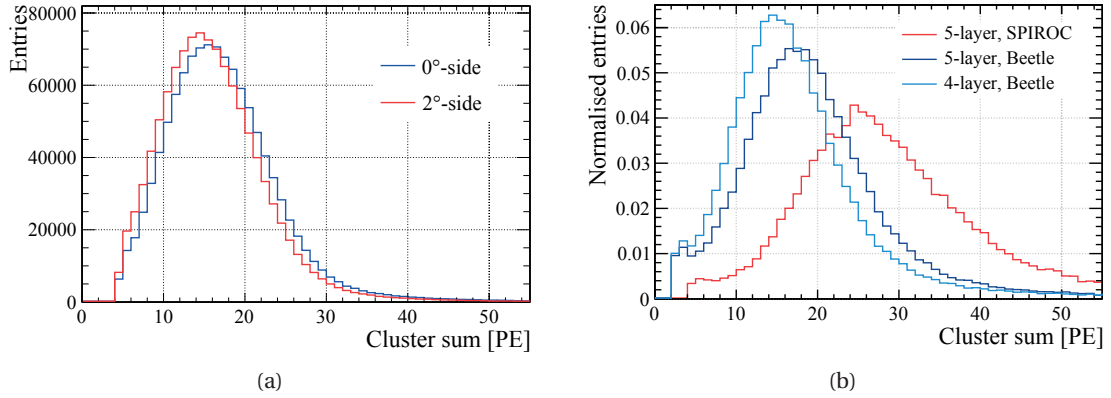


Figure 6.11 – Cluster sum distribution for BGV fibre modules with SiPMs operated at $\Delta V = 3.5$ V. Distribution obtained at the test beam for the two module sides (left) and in the laboratory with the electron-gun setup for 4- and 5-layer modules with Beetle and SPIROC read-out (right).

to a width of approximately 1 cm and scans over the module were performed.

6.3.2 Light yield

The cluster sum distribution measured for each detection plane at $\Delta V \approx 3.5$ V is shown in figure 6.11a. We measure a light yield of 15.6 and 14.6 PE for the 0°- and 2°-side, respectively. No significant difference in the cluster size was observed. The light yield in the different beam injection regions varies between 13 and 18 PE which results from several factors. For the longitudinal scan, a variation of 10% is expected (light attenuation). The SiPM temperature variations during different runs and the breakdown voltage spread between SiPMs with common bias (up to 0.5 V) lead to $\sim 10\%$ relative change in PDE. Non-uniform light yield of the fibre mats and mirror were also seen. Figure 6.11b shows the cluster sum measurement performed in the laboratory with the electron-gun setup. The light yield for 4- and 5-layer modules is 14.4 and 16.8 PE, respectively. As a consequence of the Beetle saturation, the light yield does not scale with the number of layers. The result obtained with the SPIROC, shown in the same figure, is 25.3 PE and demonstrates that the Beetle measurement is dominated by saturation effects. The light yield measured in the laboratory and at the test beam is almost identical. However, we observe a significant difference in the cluster size: low energy electrons typically spread over one channel more than high energetic particles where large saturation is observed.

6.3.3 Hit resolution

The resolution is calculated from the residual which is the distance between the position of the hit measured on the BGV module and the impact point of the track which is provided by the telescope. Over many events, the distribution of residuals is the convolution of the hit and track position distributions. Both are supposed Gaussian with sigma σ_{hit} and σ_{track} equal to the resolution on their measurement. The residual distribution is well described by a Gaussian

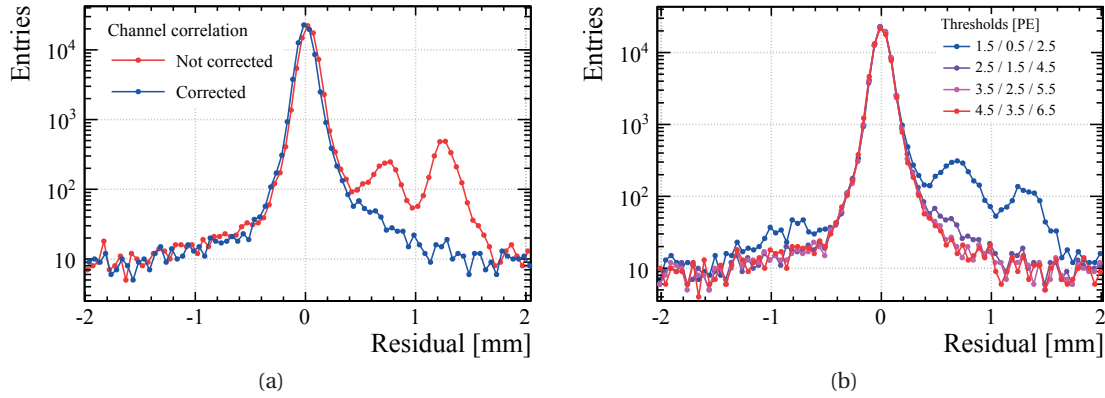


Figure 6.12 – Example of residual distribution for the 0° -side. Effect of the right-correlations (left) and of the clustering thresholds (right).

with sigma:

$$\sigma_{\text{residual}} = \sqrt{\sigma_{\text{hit}}^2 + \sigma_{\text{track}}^2}. \quad (6.4)$$

The hit resolution of the SciFi telescope detection layers was measured to be $33 \mu\text{m}$ and the track resolution $16 \mu\text{m}$. After extrapolation to the position of the BGV module, we calculate the resolution of the impact point to be:

$$\text{at the } 0^\circ\text{-side: } \sigma_{\text{track}} = 44 \pm 1 \mu\text{m} \quad \text{at the } 2^\circ\text{-side: } \sigma_{\text{track}} = 41 \pm 1 \mu\text{m}. \quad (6.5)$$

The alignment between the BGV module and the telescope was performed offline by minimising the σ_{residual} using as optimisation parameters x and y displacements as well as a rotation angle in the xy -plane. Figure 6.12 displays an example of the residual distribution with different parameters. The distribution is composed of a Gaussian peak and long tails which are caused by large scattering angles or delta electrons produced in the setup. The effect of right-correlations (figure 6.12a) is the production of ghost clusters close to the hit from the particle. The ghosts are concentrated at distance 0.75 and 1.25 mm from the hit corresponding to a distance of 3 and 5 channels, respectively. The application of the correction removes the majority of the ghosts. The distribution remains slightly asymmetric after correction due to an insufficient correction for high signals. The width of the Gaussian central peak is however not affected by right-correlations. In figure 6.12b, the residual (after correction for the channel correlations) is shown as a function of the clustering thresholds. The ghost clusters due to insufficient correction for right-correlations are visible at low thresholds.

To find the hit resolution, a fit of the central peak is performed with a Crystal Ball function. This allows to cope with enhanced asymmetric tails on the left and the right due to multiple scattering and channel correlation. The Gaussian component in the centre is taken as a reference for σ_{residual} (see figure 6.13). Averaged over all collected data and using thresholds $\text{seed}/\text{neigh}/\text{sum} = 2.5/1.5/4.5$ PE, σ_{residual} is:

$$0^\circ\text{-side: } \sigma_{\text{residual}} = 58 \pm 1 \mu\text{m} \quad 2^\circ\text{-side: } \sigma_{\text{residual}} = 59 \pm 2 \mu\text{m}, \quad (6.6)$$

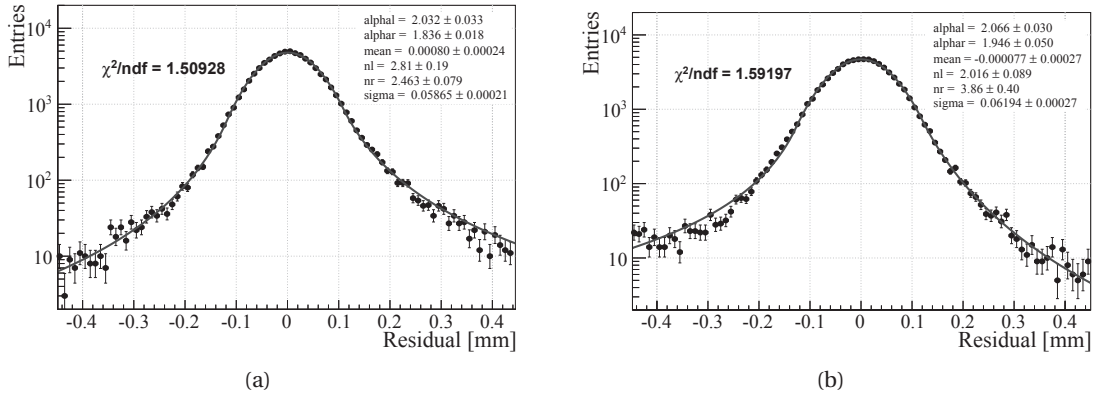


Figure 6.13 – Residual distribution fitted with a Crystal Ball function for the 0°-side (left) and the 2°-side (right) of the fibre module.

where the uncertainty includes the standard deviation over all acquired data and the errors of the fit. Using the estimated track resolution, σ_{hit} is computed for each side:

$$0^\circ\text{-side: } \sigma_{\text{hit}} = 38 \pm 3 \mu\text{m} \quad 2^\circ\text{-side: } \sigma_{\text{hit}} = 43 \pm 4 \mu\text{m}. \quad (6.7)$$

The resolution varies with the clustering thresholds and is found to be optimal at 2.5/1.5/4.5 PE. At low thresholds, the random fluctuations in the edge of the cluster introduce position fluctuations whereas at high thresholds, the deterioration of the resolution is due to cut signals.

6.3.4 Hit detection efficiency

An event is considered as efficient when a cluster is detected in the BGV module at a small distance (seed distance) from the impact point of the track. The hit detection efficiency ϵ_{hit} is calculated as the ratio of the number of efficient events to the total number of events. In order to minimise the effect of events with large scattering angles, the seed distance is set to 1.25 mm ($\approx 20 \cdot \sigma_{\text{residual}}$). An example of result for the hit detection efficiency as a function of cluster thresholds is shown in figure 6.14. A drop of efficiency is visible in the non-sensitive areas. Over all collected data, we find ϵ_{hit} to be:

$$\begin{array}{lll} 0^\circ\text{-side: } \epsilon_{\text{hit}} = 98.3 \pm 0.4\% & 2^\circ\text{-side: } \epsilon_{\text{hit}} = 97.8 \pm 0.4\% & \text{at 2.5/1.5/4.5 PE,} \\ \epsilon_{\text{hit}} = 98.7 \pm 0.4\% & \epsilon_{\text{hit}} = 98.7 \pm 0.4\% & \text{at 1.5/0.5/2.5 PE.} \end{array} \quad (6.8)$$

Figure 6.15 presents the efficiency as a function of light yield for different cluster thresholds. Using the low thresholds 1.5/0.5/2.5 PE, the efficiency is constant for a light yield between 13 and 18 PE. For a similar light yield, the small difference in efficiency between the two module sides can be due to small variations in cluster size.

In the BGV detector, as discussed in section 6.2.3, the thresholds are set between 1.5 and 2.0 PE (seed threshold) leading to an acceptable noise level (1.5 noise clusters per module and per

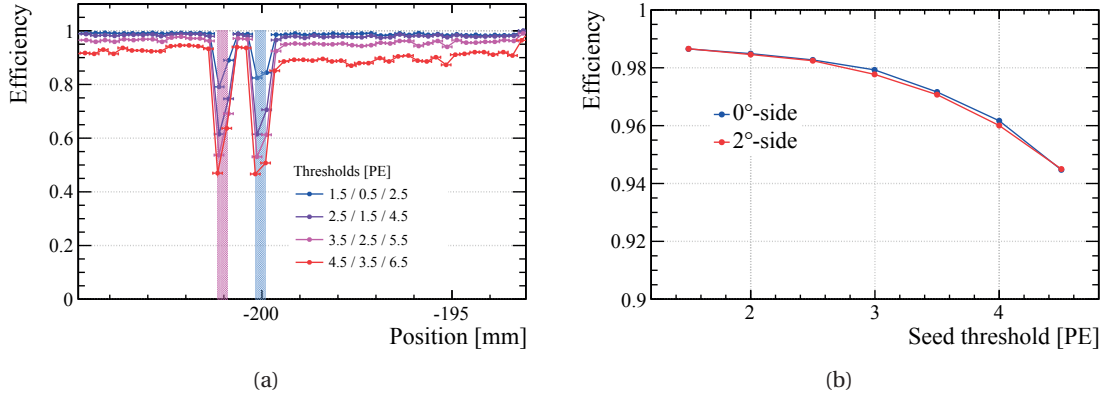


Figure 6.14 – Hit detection efficiency as a function of position (left) and cluster thresholds (right). The hatched zones depict the position of a dead channel (purple) and an SiPM gap (blue). In the right plot, the average efficiency is computed (excluding non-sensitive areas).

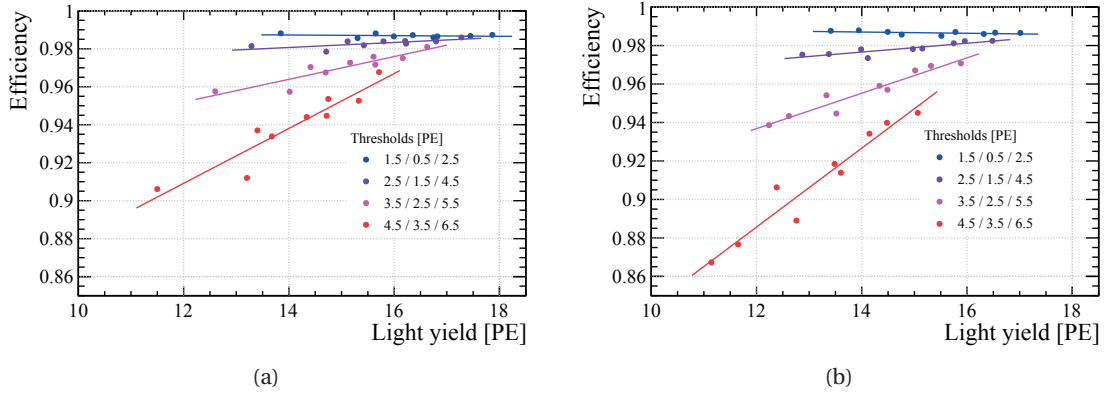


Figure 6.15 – Hit detection efficiency as a function of the light yield for different cluster thresholds for the 0°-side (left) and the 2°-side (right).

event). The measurements presented here demonstrate that the 4-layer modules can reach hit detection efficiency above 98% using the same threshold values. The efficiency expected for the 5-layer modules is even higher given the increased light yield.

6.3.5 Hit detection efficiency in non-sensitive areas

The hit detection efficiency drops at non-sensitive areas in the fibre mats or the photodetectors. In the SiPMs, gaps are present in the middle of an array between the two silicon dies (die gap, 250 μm), between two adjacent arrays (SiPM gap, 400 μm) and at disconnected channels on the front-end board or the SiPM flex (dead channel, 250 μm). Each detection plane (26 cm wide) of the module is composed of fibre mats of 6.5 cm width placed next to each other. The longitudinal cut of each mat and their positioning leads to a non-sensitive area (mat gap, $\gtrsim 400 \mu\text{m}$) coinciding with the SiPM gap.

Figure 6.16 shows a zoom on the hit detection efficiency profile in the non-sensitive areas of the module for two different sets of thresholds. In the centre of gaps, the efficiency drops

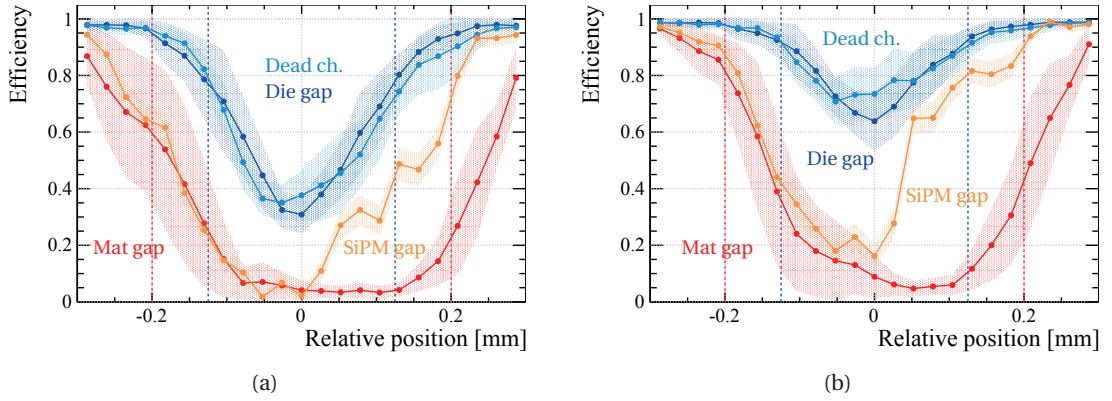
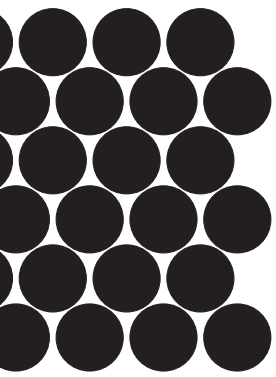


Figure 6.16 – Hit detection efficiency in non-sensitive areas for cluster thresholds of 2.5/1.5/4.5 (left) and 1.5/0.5/2.5 PE (right). The error bands includes the statistical error and the standard deviation between all gaps scanned. The position of the non-sensitive areas is indicated with the vertical lines.

to 35 and below 5% for 250 μm - and 400 μm -wide gaps, respectively, using thresholds of 2.5/1.5/4.5 PE. In average over the whole gap, it is approximately 70% for die gaps and dead channels whereas it is 40% for SiPM gaps and below 20% for mat gaps. The very low efficiency in mat gaps is due to broken fibres at the edge of the mats which leads to a low light yield. Using lower cluster thresholds of 1.5/0.5/2.5 PE, we observe a significant increase in efficiency except for the mat gaps.

In the BGV detector operation, the SiPMs are cooled to a temperature between -10 and -40°C . Due to the thermal expansion, we expect that the size of the gaps between silicon dies and between adjacent SiPMs increases by up to 50 μm with respect to room temperature.



Conclusion and outlook

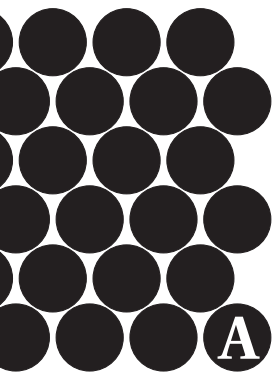
Through this PhD work, I studied many aspects of the SciFi technology for applications in radiation environment. For this purpose, I developed characterisation methods for SiPMs suitable for irradiated devices as well as the instruments required to test SciFi modules in high energy particle beams. These developments have been performed in the context of the LHCb SciFi tracker which is the first large-scale application of the technology, where scintillating fibres are read out by SiPMs, in a harsh radiation environment.

For the operation of the SciFi tracker, many requirements are in contradiction, such as low mass and mechanical stability or high hit detection efficiency and low noise cluster rate after irradiation of the fibres and photodetectors. The tracker is based on scintillating fibres with high light yield and large attenuation length read out by SiPM arrays featuring high photon detection efficiency and low correlated noise. The selected photodetector, produced by Hamamatsu Photonics (HPK) has shown sufficient radiation hardness and reduced correlated noise as a result of a long collaborative R&D effort. Single photon detection remains possible after irradiation to $6 \cdot 10^{11} \text{ 1 MeV n}_{\text{eq}}/\text{cm}^2$ which represents the expected accumulated radiation at the end of lifetime of the SciFi tracker for the LHCb experiment after the upgrade. The measurement methods that we developed allow to reach high precision for the characterisation of irradiated SiPMs. The results show no significant change in optical cross-talk, gain and photon detection efficiency. We measure a small reduction in gain (below 10%) whereas we can exclude changes in cross-talk up to $12 \cdot 10^{11} \text{ 1 MeV n}_{\text{eq}}/\text{cm}^2$ and in PDE up to $6 \cdot 10^{11} \text{ 1 MeV n}_{\text{eq}}/\text{cm}^2$. These results, together with the outcome of several fibre module characterisation campaigns with high energy particles, give confidence that the tracker design for LHCb can fulfil the high hit detection efficiency required.

Application of SciFi technology is already demonstrated by the BGV detector for the measurement of the LHC beam profile. I have contributed to this project through the design, fabrication, characterisation and installation of the tracking modules as well as the commissioning and optimisation of the read-out. The detector provides now promising results on the LHC beam profile which supports the implementation of new detectors with similar concept in the high-luminosity LHC and other accelerators. The evaluation and design of this detector has also given valuable insight for the large scale LHCb SciFi.

The SciFi technology has reached a level of maturity opening the possibility of new applications

for particle tracking over large surface with high granularity providing a spatial resolution in the order of $50\text{ }\mu\text{m}$. It can be tailored to provide a fine timing information which offers the potential to improve pattern recognition at high detector occupancy and suppress accurately the noise from irradiated SiPMs. The time resolution is limited by the low number of detected photons and the relatively long decay time of the scintillator. To achieve timing resolution below 1 ns , it is beneficial to reduce the decay time maintaining a high scintillation yield and increase the number of fibre layers.



A LHCb SciFi tracker module characterisation

The performance of long fibre modules was evaluated throughout the R&D phase of the SciFi tracker during several test beam campaigns. The measurements include light yield, hit resolution and hit detection efficiency. In parallel, fibre irradiation studies have been carried out in order to ensure that the required performance can be achieved up to the 50 fb^{-1} integrated luminosity. This chapter gives a summary of the most relevant results obtained with 6-layer fibre modules. More details can be found in reference [117] which contains a comprehensive description of all measurements performed in the early R&D phase (2015).

A.1 Experimental setup

The test beam campaigns took place at CERN and at DESY in Hamburg. At CERN, we use the test facility at the North Area of the SPS. The beam is generated by the 450 GeV/c protons from the SPS directed to a target. It contains protons (60%), pions (30%) and muons (10%) with a selected momentum of 180 GeV/c. It is emitted in 5 – 10 s spills with a flux of $10^5 - 10^6$ particles per second. At DESY, the beam is produced by the DESY II synchrotron. It is composed of electrons with an energy that can be chosen between 1 to 6 GeV. To reconstruct the track and enable the efficiency and resolution measurements, the experimental setup includes external beam telescopes: the TimePix telescope from the LHCb VELO Upgrade project [118], the AMS ladders from the AMS experiment [119] and a SciFi-based telescope developed at EPFL [116]. They provide an estimated resolution at the position of the modules between 10 and 16 μm . The details of the experimental setups used in the different test beam campaigns are listed in table A.1. In 2015 and 2016, the measurements were carried out at CERN whereas the most recent measurements were performed at DESY.

A.2 Light yield and attenuation length

The results on the light yield and the fibre attenuation length rely on measurements performed in 2015 at SPS with high energetic particles and with 6-layer modules read out by H2014 detectors at $\Delta V = 3.5 \text{ V}$. The light yield was determined at different positions in order to evaluate light attenuation in the fibres, as shown in figure A.2. The cluster sum distribution for particles injected close to the mirror has an average of 15.8 PE. The light yield as a function of

Appendix A. LHCb SciFi tracker module characterisation

Table A.1 – Test beam configurations used for the characterisation of LHCb SciFi modules at CERN SPS (2015-2016) and DESY (2017). The H2016-HRQ SiPM denotes the first prototype of the H2017.

Period Location	Fibre mats	SiPMs	Electronics	Beam telescope
May 2015 SPS	5- and 6-layer	H2014	SPIROC	AMS ladders and VELO Timepix3
Nov 2015 SPS	6-layer (irrad.) and 8-layer			VELO Timepix3 and SciFi telescope
Nov 2016 SPS	2×6-layer (irrad.)			VELO Timepix3
Feb 2017 DESY	6-layer (non- and irrad.)	H2016-HRQ	SPIROC and PACIFIC (v.4)	SciFi telescope
Aug 2017 DESY		H2016-HRQ and H2017		

the distance x between the injection point and the read-out side follows a sum of a short and a long exponential:

$$N(x) = N_{\text{short}} \cdot e^{-x/\Lambda_{\text{short}}} + N_{\text{long}} \cdot e^{-x/\Lambda_{\text{long}}}. \quad (\text{A.1})$$

The short component has typical attenuation length Λ_{short} in the order of 10 cm and is due to photons travelling on helical paths inside the fibres. To compare different fibre technologies during the R&D phase, the attenuation length Λ_{long} of the long component was used. It is determined from a fit of the light yield above 1 m distance from the SiPM with a single exponential function. Note that the fit function used in figure A.2 is modified to account for the mirror reflectivity. The attenuation length is found to be $\Lambda_{\text{long}} = 3.1$ m, a value slightly smaller than measured for single fibres (3.2 to 3.8 m).

Detailed measurements of the light yield and the cluster size with various beam injection angles have been performed and can be found in reference [117]. An important remark is that very wide clusters are observed (size > 4) which is not expected from the fibre mat geometry and can be explained by the cross-talk between fibres. The test beam results (cluster sum and cluster size distributions) match well with the SciFi tracker simulation assuming a total effective cross-talk probability from one fibre to its neighbours in the order of 20%.

Using the latest SiPM version H2017, the light yield changes according to the improvements in PDE and correlated noise. The light yield obtained with H2017 in the more recent test beam campaigns is however not taken as reference since the electrons at DESY undergo considerable multiple scattering. The average cluster sum measured with H2017 and the electron beam is 18.5 PE which represents a 17% increase. Instead, from laboratory measurements with a ^{90}Sr source, an increase of approximately 10% is expected between H2014 and H2017.

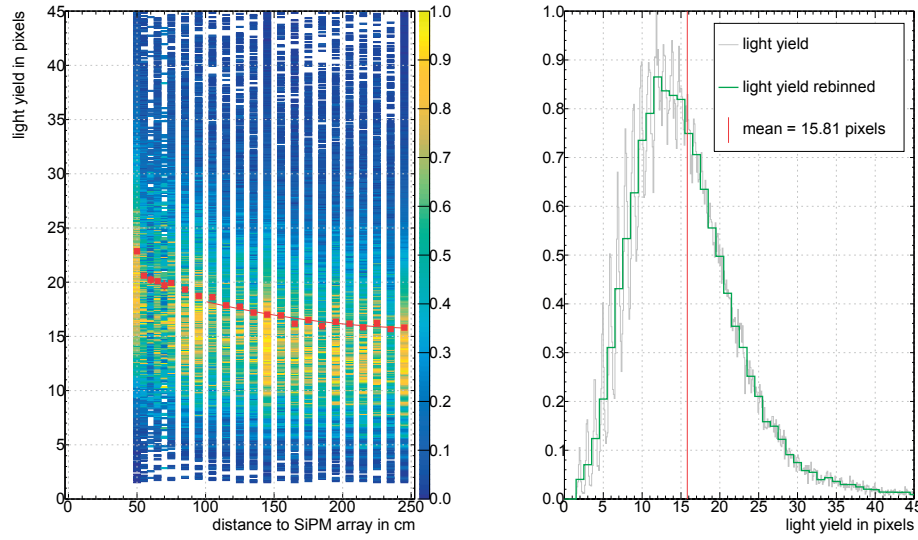


Figure A.2 – Cluster sum distribution of a 6-layer mat equipped with a mirror and read out by H2014 detectors at $\Delta V = 3.5V$ as a function of the distance to the SiPM side (left) and projection of the slice closest to the mirror (right). The red points (left) and the red line (left) denote the mean cluster sum. Graphs from [117].

A.3 Hit resolution

The SPS test beam facility with high energetic particles offers the best conditions for the evaluation of the spatial resolution. The reference results are therefore taken from the 2015 test beam with H2014 detectors. In the more recent campaigns at DESY with H2017 SiPMs, multiple scattering of the electrons influences the measurement. The change of SiPM version is not expected to have a large impact on the hit resolution given that the channel width is the same.

The resolution is calculated from the residual which is the distance between the position of the hit measured on fibre module and the impact point of the track which is provided by the independent beam telescope. Over many events, the distribution of residuals is the convolution of the hit and track position distributions. Both are supposed Gaussian with sigma σ_{hit} and σ_{track} equal to the resolution on their measurement. The residual distribution is well described by a Gaussian with sigma:

$$\sigma_{\text{residual}} = \sqrt{\sigma_{\text{hit}}^2 + \sigma_{\text{track}}^2}. \quad (\text{A.2})$$

In practice, the residual is the only parameter that can be measured. The beam telescopes provide a track with resolution better than $18 \mu\text{m}$ which allows for a good sensitivity on σ_{hit} . Note that equation (A.2) does not account for the transverse deviations due to multiple scattering. This effect is more pronounced in setups using the VELO Timepix3 telescope where each plane represents approximately 2.6% of a radiation length [118]. The effect on the impact point from the extrapolation of the track is below $5 \mu\text{m}$. The expected hit resolution being

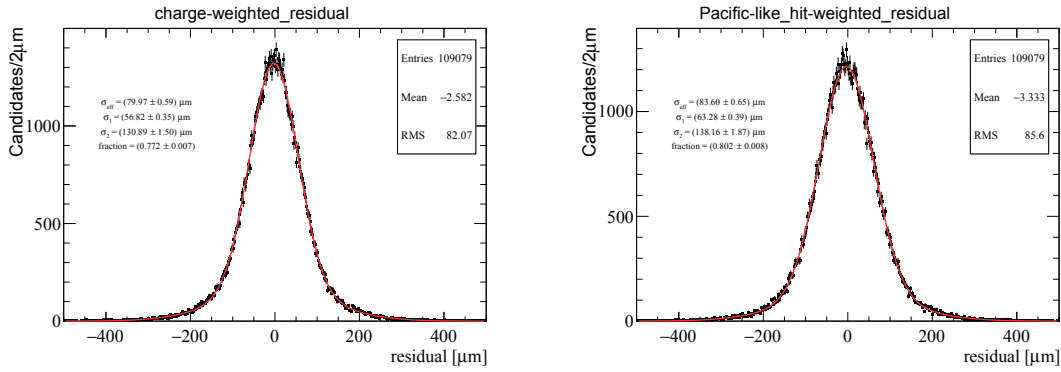


Figure A.3 – Residual distributions measured with a 6-layer mat, H2014 read-out and beam injection at the mirror. The hit position is determined from the clusters in two ways: barycentre of the signal amplitudes (left) and PACIFIC-like charge weighting (right). The sigma of the effective fit is $80.0 \pm 0.6 \mu\text{m}$ and $83.6 \pm 0.7 \mu\text{m}$, respectively. Graphs from [117].

around $80 \mu\text{m}$, the contribution of the track resolution and multiple scattering to σ_{residual} can be neglected.

The residual distribution measured at SPS is shown in figure A.3. Large scattering angles occurring in the setup and energetic delta rays make the distribution not exactly Gaussian introducing tails at large residual values. The distribution is described by the sum of two Gaussian functions. The width σ_{eff} of the effective fit is given by the squared sum of the widths of both Gaussian functions weighted by their fraction. A comparison between the residual obtained with the standard clustering of section 3.1.2 and the PACIFIC-like clustering is shown in figure A.3. In the PACIFIC-like clustering, the weights used for channel reaching the neighbour, seed and high threshold are respectively adjusted to 2, 4 and 12. It shows that the PACIFIC clustering algorithm does not introduce a significant deterioration in hit resolution.

A.4 Hit detection efficiency and spillover

The hit detection efficiency is determined by the ratio between the number of clusters correctly reconstructed in the SciFi module to the number of tracks predicted by the telescope. It depends on the clustering thresholds and on the maximum distance allowed between the cluster and the track position. The 2017 test beams were dedicated to the measurement of the efficiency with the latest SiPM H2017 and the PACIFIC chip (version 5). The results show that it meets the expectations from the measurements with SPIROC. Using clustering thresholds of $\text{seed}/\text{neigh}/\text{high} = 2.5/1.5/4.5$ PE, the hit detection efficiency at $\Delta V = 3.5$ V and beam injection near the mirror is 99.4 and 98.2% with SPIROC and PACIFIC, respectively. [120]

In the test beam, the spillover with the PACIFIC was observed to be approximately 25% in the next bunch crossing. It was proposed to change the shaper settings and introduce an undershoot in order to reduce the spillover for the final implementation. According to laboratory measurements, this reduces the spillover in the next bunch crossing to approximately 5%. [120]

A.5 Radiation effects on fibre module performance

Two types of degradation occur in the fibres due to the ionising radiation: reduction in the scintillation light yield due to damage to the fluorescent molecules and loss of transmission due to defects introduced in the fibre core. Several studies were performed with single fibres irradiated with protons at different dose and dose rates. No change in the scintillation yield was observed in the dose range of the LHCb SciFi whereas the fibre attenuation length is seen to be reduced. For high dose rate, it is seen that the fibre partially recovers its transparency through an annealing process. The annealing rate depends on the oxygen content of the environment. A simulation based on the irradiation studies allowed to draw a prediction for the expected permanent damage to the fibres in the SciFi tracker. The result is an approximately 30% reduced light yield for particles passing close to the beam pipe. More information on these studies can be found in references [66, 121].

Irradiation studies were also performed with fibre mats. Six-layer mats were irradiated in 2015 and 2016 with 24 GeV/c protons at the CERN PS IRRAD facility with a high dose rate [122] ^a. The dose is deposited over the full length of the mats but over only a fraction of its width. In the transverse direction, a 3 cm-wide section comprises a uniform irradiation. The resultant dose profile along the fibres resembles within $\pm 40\%$ the expected distribution for the modules close to the beam pipe at LHCb after 50 fb^{-1} . The mats were characterised in the laboratory with a ^{90}Sr source and during the test beams. The light yield measured at the mirror right after irradiation was reduced by more than 60%. It partially recovers over a time period of 20 days and levels off at approximately 37% of signal loss compared to before irradiation. In the edge of the irradiation section of the mats where the cumulated dose is lower and the dose rate was lower, the recovery period is seen to be shorter (below ten days). Note that a separate study has shown that the effect of irradiation on the mirrors is negligible. [120, 123]

No recent studies are presently available to confirm that fibre mats irradiated at low dose rate have the same signal loss. In reference [124] dating from 1992, it is shown that the permanent degradation of the transmittance of pure polystyrene is larger for a low dose rate in an environment containing oxygen than if the dose is delivered fast.

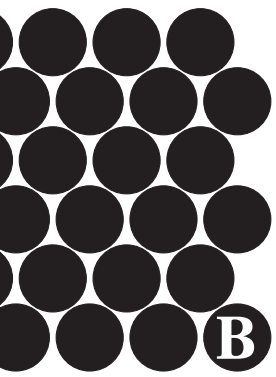
The reduced light yield after irradiation has an important impact on the hit detection efficiency. In the 2017 test beam, the latter was measured with beam injected close to the mirror and with the SPIROC read-out. The result is 91.2% at clustering thresholds of *seed/ neigh/ high* = 2.5/1.5/4.5 PE. With the PACIFIC read-out, it is 88.5%. This poses severe challenges to operate the most irradiated SciFi modules close to the beam pipe over the full detector lifetime. It is crucial to keep the SiPM dark noise as low as possible in order to allow for the lowest thresholds possible. On the other hand, the hit resolution is not affected by the loss in light yield.

The CERN group taking care of the fibre quality assurance has performed repeated attenuation length measurements on the same non-irradiated fibre samples over long time periods (< 19 months). It is seen that the attenuation length decreases with time due to fibre ageing. The reduced transparency caused by ageing was already observed for a particular type of fibres

^a In parallel, a 5-layer mat is being irradiated in the LHC tunnel with a much smaller dose rate close to the one that will be encountered in the experiment.

Appendix A. LHCb SciFi tracker module characterisation

with polystyrene core in reference [125]. It is attributed to a slow oxidation of the polystyrene. In the present case, the measurement period has not been sufficiently long to predict the effect on the operation of the SciFi during the next LHC run. A pessimistic extrapolation indicates that the permanent damage due to aging might reach the same level as the radiation damage.



B Characterisation of different SiPM types

Using the methods explained in chapter 4, we characterised various types of SiPMs. We give example of results for the first versions of SiPM developed for the LHCb SciFi tracker (Hamamatsu H2014 and H2015, KETEK) as well as for single-channel devices from Hamamatsu, FBK and SensL. More details and results on the different SiPM prototypes for the SciFi tracker can be found in [106, 126, 127].

B.1 Multichannel prototypes for the LHCb SciFi tracker

The H2014 detector is the first generation of Hamamatsu array with trenches. The channels have an active surface of $230\text{ }\mu\text{m} \times 1.5\text{ mm}$ and contain 96 pixels. The H2015 is the second generation of arrays with trenches and has an increased channel height with respect to the H2014 ($230\text{ }\mu\text{m} \times 1.625\text{ mm}$, 104 pixels per channel) and reduced non-sensitive areas. The quench resistor is implemented by a transparent thin metal film put on top of the pixel. Figure B.1 shows a microscope view of the pixel implementation in the Hamamatsu detectors. The geometrical aspect of the guard rings and the trenches is unchanged between the H2015 and the H2017.

The correlated noise composition of an H2014 and H2015 detector is shown in figure B.2. The high DiXT in H2014 is due to sub-optimal trench technology which was improved in

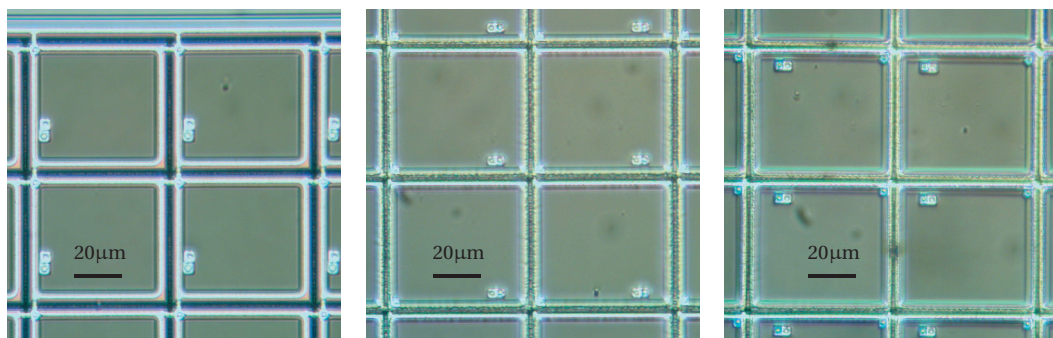


Figure B.1 – Comparison of the pixel implementation in the Hamamatsu SiPMs for the SciFi tracker: H2014 (left), H2015 (middle) and H2017 (right).

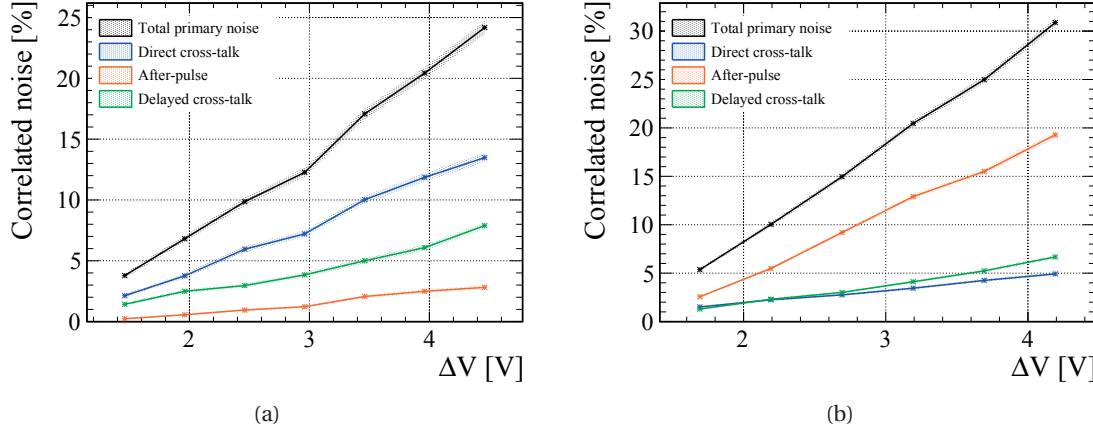


Figure B.2 – Correlated noise composition of H2014 (left) and H2015 (right) detectors. The AP probability is measured with a low threshold of 0.3 PE.

the next generation. The H2015 has a much reduced cross-talk but an increased after-pulse probability. In addition to the difference in occurrence probability, the correlated noise of H2014 is concentrated in the very first 10 ns following the primary avalanche whereas it is spread over a longer period for H2015. We measure $\tau_{AP} \approx \tau_{DeXT} < 10$ ns and $\tau_{AP} = 18$ ns and $\tau_{DeXT} = 21$ ns for H2014 and H2015, respectively.

The quench resistor for the two types is in the order of 200 k Ω . This value was initially chosen for the SciFi tracker in order to ensure a fast pixel recovery and to minimise spill-over effects from the long pulse component (τ_{rec} and τ_{long} are proportional to R_Q). A larger quench resistor value was proposed by Hamamatsu for the final SiPM design. As far as we can tell, the larger R_Q is one of the reasons for the strong reduction in the delayed correlated noise in H2017.

The pulse time constants are measured to be $\tau_{rec} = 24$ ns and $\tau_{long} = 25$ ns for the H2014 device and $\tau_{rec} = 32$ ns and $\tau_{long} = 31$ ns for the H2015. We observe in both cases that $\tau_{rec} \approx \tau_{long}$ which is compatible with the pulse shape model of section 2.3.3, in contrast to the H2017. Using the quench resistor measured from forward IV scans ($R_Q = 180$ and 217 k Ω), we obtain the model capacitance ($C_d + C_Q$) = 133 and 148 fF for H2014 and H2015, respectively.

The PDE of H2014 and H2015 detectors is shown in figure B.3. We observe identical PDE for the H2015 as for the H2017, as expected from the similar fill factor. The H2014 detector has a much reduced PDE due to the lower fill factor. The gain obtained using the method introduced in section 4.3 is $(0.90 \pm 0.02) \cdot 10^6$ and $(1.09 \pm 0.02) \cdot 10^6$ V $^{-1}$ for H2014 and H2015 detectors, respectively. The gain of the H2015 is identical to the value obtained for H2017 detectors. This shows that the pixel implementation technology is similar in both cases. In contrast, the lower gain in the H2014 can probably be explained by a different detector capacitance due to smaller pixel active area and thinner avalanche layer thickness. Comparing with the value that can be estimated from $G/\Delta V = \tau_{rec}/(R_Q \cdot e)$, we see a good agreement for the H2014 detector ($0.87 \cdot 10^6$ V $^{-1}$). For the H2015, we observe however a 15%-difference ($0.93 \cdot 10^6$ V $^{-1}$).

Many other prototypes from KETEK using different silicon wafer technology were tested. As an example, we give the results for a *wafer 7* operated at -15°C to reduced DCR. As shown in

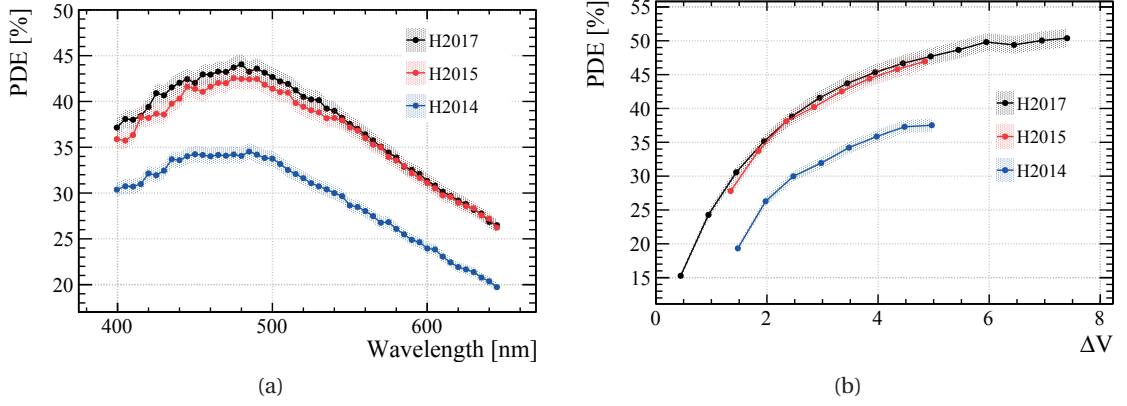


Figure B.3 – PDE as a function of wavelength with fixed $\Delta V = 3.5$ V (left) and ΔV with fixed wavelength $\lambda = 475$ nm (right) for H2014 and H2015 compared to the results obtained for the H2017 detector. The method based pulse frequency was used.

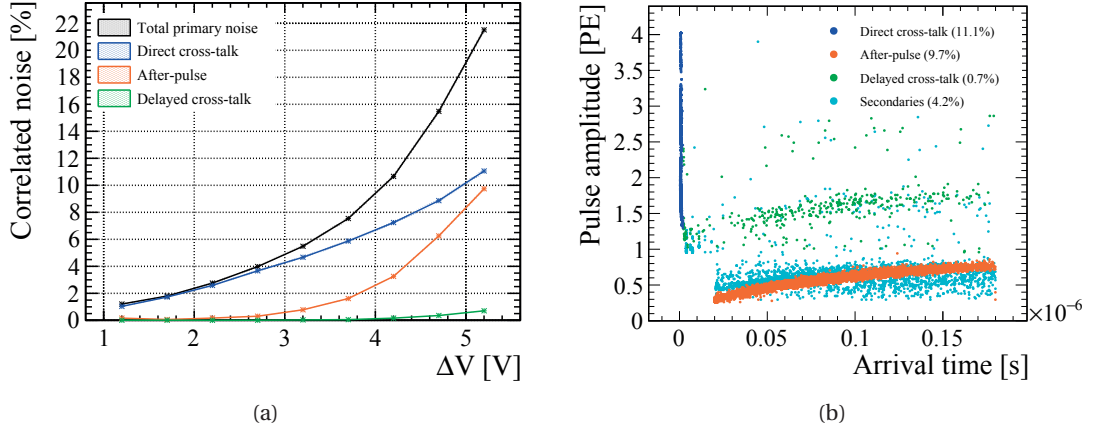


Figure B.4 – Correlated noise composition of a KETEK prototype at -15°C . Note that the AP probability is measured with a low threshold of 0.25 PE. The correlated noise amplitude as a function of arrival time is shown at $\Delta V = 5.2$ V (right).

figure B.4a, the performance in terms of correlated noise is comparable to H2014 and H2015 detectors. At $\Delta V < 4$ V, AP and DeXT are almost non-existent. The AP increases however rapidly for larger ΔV . It is interesting to note that, as shown in the diagram of figure B.4b, the pulses identified as DeXT are in fact APs with a DiXT and, consequently, the DeXT probability scales as $p_{\text{DeXT}} \sim p_{\text{DiXT}} \cdot p_{\text{AP}} \approx 1\%$. The APs are also much more spread in time than in Hamamatsu detectors and are characterised by a mean lifetime of $\tau_{\text{AP}} \approx 55 \pm 3$ ns, constant over different ΔV . In contrast to the results found for Hamamatsu devices and to the expectations from the pulse shape model, we measure large variations in τ_{long} and τ_{rec} for different ΔV . The long pulse time constant changes from $\tau_{\text{long}} = 118$ to 81 ns at $\Delta V = 1.3$ to 5.3 V. The recovery time varies also substantially from $\tau_{\text{rec}} = 146$ to 116 ns at $\Delta V = 3.3$ to 5.3 V. As for H2017 devices, we obtain different values for τ_{long} and τ_{rec} which is an additional contradiction to the model. Using the values found at $\Delta V = 3.3$ V and the quench resistor $R_Q \approx 500$ k Ω , we compute $C_d = 177$ fF and $C_Q = 115$ fF assuming $\tau_{\text{long}} = R_Q \cdot C_d$ and $\tau_{\text{rec}} = R_Q \cdot (C_d + C_Q)$.

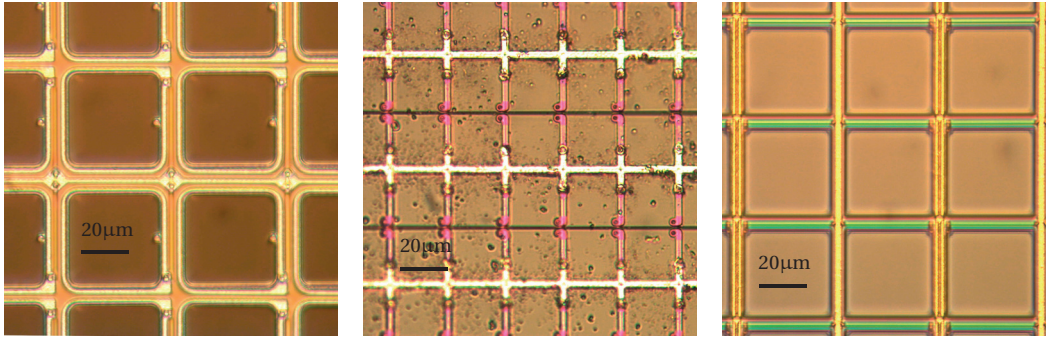


Figure B.5 – Comparison of the pixel implementation in single-channel devices from Hamamatsu (left), FBK (middle) and SensL (right).

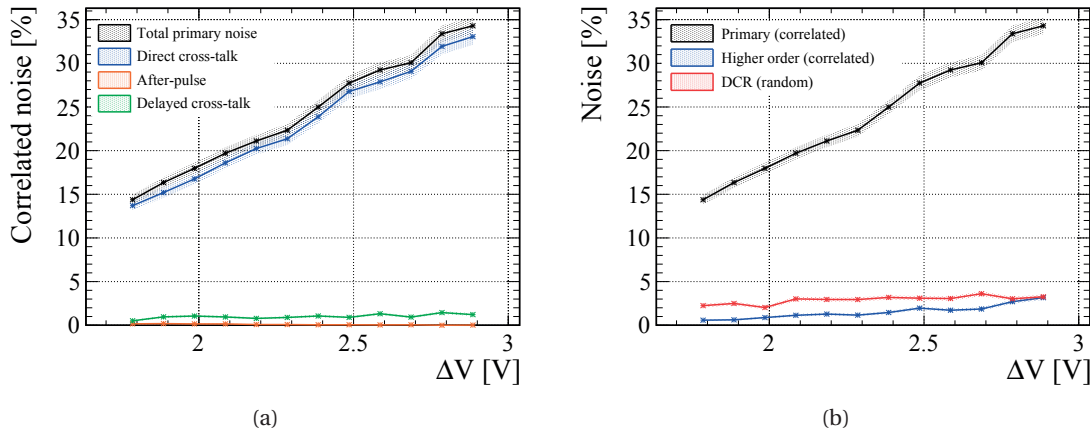


Figure B.6 – Correlated noise composition for a Hamamatsu single-channel device (S12572-050C) as a function of ΔV (left) and contributions from higher order correlated noise and DCR (right).

B.2 Single-channel devices

The waveform analysis of chapter 4 is very robust and can easily cope with a variety of device types (pixel size, total area). We tested single-channel devices available on the market from Hamamatsu, FBK and SensL. A microscope view of their pixel implementation is shown in figure B.5. The Hamamatsu detector (H) is a S12572-050C, $3 \times 3 \text{ mm}^2$ with 60×60 pixels of $50 \mu\text{m}$ size. The FBK is a $1 \times 1 \text{ mm}^2$ RGB-HD SiPM with 40×40 pixels of $25 \mu\text{m}$ size. The SensL is a $3 \times 3 \text{ mm}^2$ MicroES-SMA-30035-TSV-E32 with 5676 pixels of $35 \mu\text{m}$ size. The detectors are mounted on a PCB avoiding wire pins or cables to minimise serial inductance and the associated ringing. The measurements for the H and FBK are done at -15°C in order to reduce the DCR.

The correlated noise of these SiPMs is shown in figures B.6, B.7 and B.8. In the three cases, it is dominated by the DiXT and we observe almost zero AP probability. The influence of DCR is controlled and shown to be below 4% for the large area H device whereas it is almost negligible in the case of the FBK and SensL devices. The DiXT probability for the H is in very good agreement with the manufacturer's datasheet whereas it is lower than expected

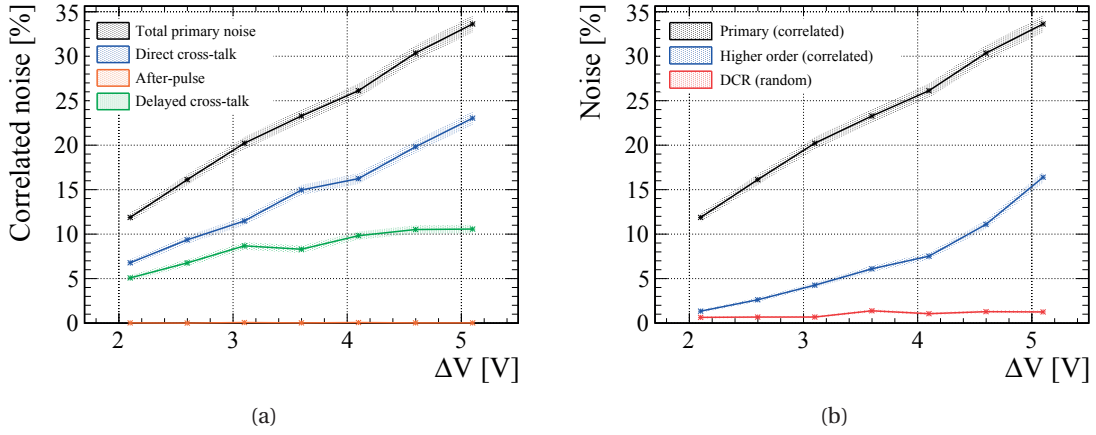


Figure B.7 – Correlated noise composition for an FBK single-channel device as a function of ΔV (left) and contributions from higher order correlated noise and DCR (right).

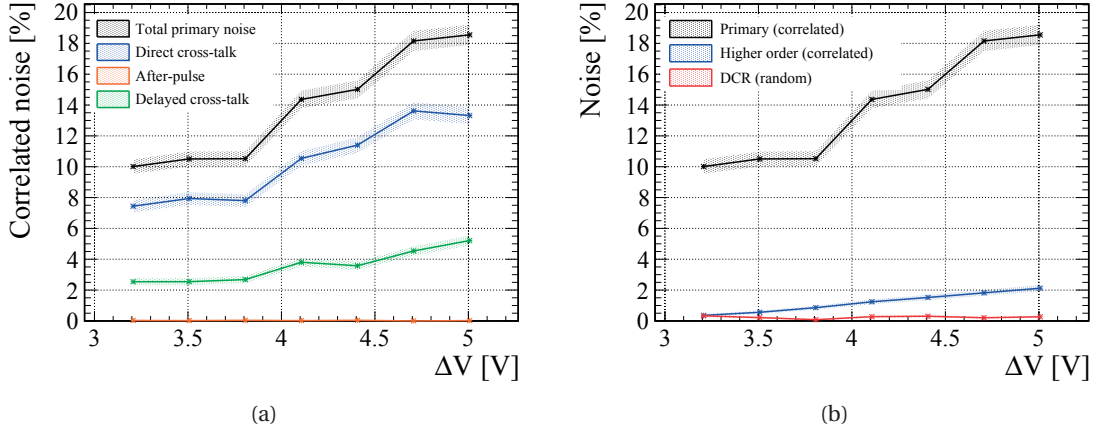
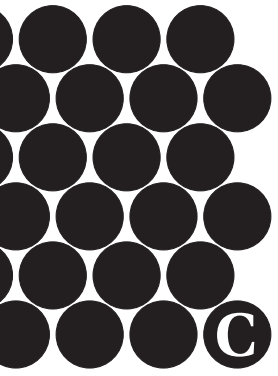


Figure B.8 – Correlated noise composition for a SensL single-channel device (MicroES-SMA-30035-TSV-E32) as a function of ΔV (left) and contributions from higher order correlated noise and DCR (right).

for the SensL device (no comparison found for the FBK 25 μm device). The absence of AP prevents the determination of the recovery time. We therefore assume that the SiPM model of section 2.3.3 is valid and take $\tau_{\text{rec}} = \tau_{\text{long}}$. In the pulse shape of the Hamamatsu detector, only the slow component is visible due to the reduced input bandwidth of the acquisition setup. We measure $\tau_{\text{long}} = 32$ ns and, using the quench resistor obtained from an IV curve $R_Q = 275$ k Ω , we can compute the capacitance to be $(C_d + C_Q) = \tau_{\text{long}} / R_Q = 116$ fF. This leads to an estimate for the gain as $G / \Delta V = \tau_{\text{long}} / (R_Q \cdot e) = 0.72 \cdot 10^6 \text{ V}^{-1}$ which is larger than the expected value provided by the manufacturer ($0.5 \cdot 10^6 \text{ V}^{-1}$).



© Beam size measurement techniques for the BGV detector

In the BGV, the measurement of the beam profile from data collected by the fibre modules involves different algorithms which have been developed since the design of the demonstrator. We give here a short summary of the analysis methods while more details and results can be found in [101, 102] as well as in an upcoming publication.

A 3D pattern recognition algorithm finds clusters belonging to the same track by assuming straight trajectories originating from the gas volume (see an event display example in figure C.1). It starts with clusters in the last detection layer of the far station and computes a window to search for a corresponding cluster in the first layer of the near station. The clusters in the other detection layers are subsequently added to the track using a similar procedure. To minimise the number of reconstructed tracks from random combinations, the tracks are required to include a cluster in each plane (8 clusters in total). Assuming a 99% efficiency for the planes (4- and 5-layer mats), which seems reasonable according to the test beam measurements, we obtain the track finding efficiency to be approximately 92%.

To find the beam profile, two methods are used. The vertex of a beam-gas interaction can be calculated as the intersection of all tracks found in the event. This method is currently under development and has not led to satisfactory results yet. The beam profile is obtained from the

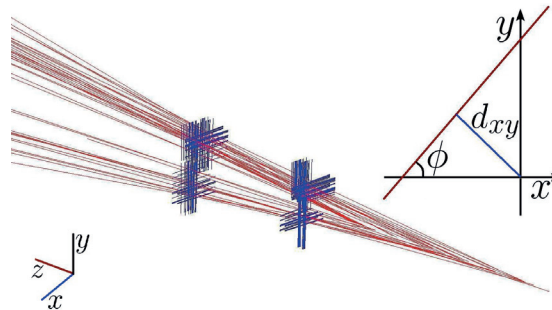


Figure C.1 – BGV event display using the LHCb software *Panoramix*. The blue lines represent the clusters from the fibre modules whereas the red lines are the reconstructed tracks. The insert shows how the azimuthal angle ϕ and the impact parameter d_{xy} are defined. Image from [101, 102].

distribution of vertices in the xy -plane. The other method for beam size measurement, called impact parameter correlation (IPC) method, is based on the correlation between tracks from the same vertex [128, 129]. The impact parameter d_{xy} (the distance of closest approach to the z -axis) and azimuthal angle ϕ of a track, as defined in figure C.1, are related to the primary vertex location (x_0, y_0) in the xy -plane as:

$$d_{xy} = x_0 \sin \phi - y_0 \cos \phi. \quad (\text{C.1})$$

Measuring d_{xy} as a function of ϕ for tracks generated by several beam-gas interactions, one can determine the average beam position $(x_{\text{beam}}, y_{\text{beam}})$ using equation (C.1). To measure the beam width σ_{beam} , we look at the covariance of d_{xy} from track pairs originating from the same vertex as a function of the ϕ angles:

$$\begin{aligned} \langle d_{xy,1}, d_{xy,2} \rangle &= \langle x, x \rangle \cdot \cos \phi_1 \cos \phi_2 + \langle y, y \rangle \cdot \sin \phi_1 \sin \phi_2 - \langle x, y \rangle \sin(\phi_1 + \phi_2) \\ &= \frac{1}{2} (\sigma_x^2 + \sigma_y^2) \cdot \cos(\phi_1 - \phi_2) + \frac{1}{2} (\sigma_x^2 - \sigma_y^2) \cdot \cos(\phi_1 + \phi_2) - \\ &\quad \langle x, y \rangle \sin(\phi_1 + \phi_2), \end{aligned} \quad (\text{C.2})$$

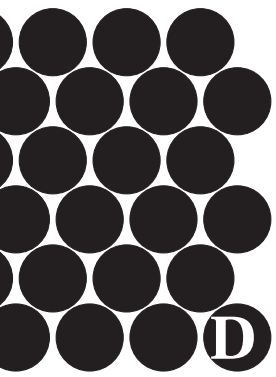
where the brackets $\langle \cdot, \cdot \rangle$ denote the covariance operator and σ^2 the variance. One can define a new coordinate system (u, v) , rotated by an angle α with respect to (x, y) , such that the covariance term cancels. It can be shown that, under the assumption that the measurement errors on d_{xy} from different tracks are uncorrelated, the only factors left are:

$$\langle d_{xy,1}, d_{xy,2} \rangle = \frac{1}{2} (\sigma_u^2 + \sigma_v^2) \cdot \cos(\phi_1 - \phi_2) + \frac{1}{2} (\sigma_u^2 - \sigma_v^2) \cdot \cos(\phi_1 + \phi_2 + 2\alpha). \quad (\text{C.3})$$

In the case of a circular beam, we have $\sigma_u = \sigma_v = \sigma_{\text{beam}}$ and the previous equation simplifies to:

$$\langle d_{xy,1}, d_{xy,2} \rangle = \sigma_{\text{beam}}^2 \cdot \cos(\phi_1 - \phi_2). \quad (\text{C.4})$$

It can be demonstrated that the σ_{beam} found with this method does not depend on the vertex resolution and z -position. It is a direct measurement of the beam width. Validation of the procedure and study of the systematic errors using Monte Carlo simulation and real measurements are ongoing. Very encouraging results have been obtained in 2017 after a long commissioning of all detector operation and read-out parameters. The beam width from the IPC method has been measured to be in the range expected from other beam diagnostics instruments. Also, for the first time, σ_{beam} has been measured during the energy ramp and the expected $1/\sqrt{E}$ dependence was confirmed.



D Cosmic particle tracker for outreach

The EPFL was open to the public on the week-end of 5 and 6 November 2016. In order to present the activities of our institute, we developed and constructed a cosmic particle detector demonstrator able to display the events in real-time. It integrates in addition some basic analysis functionality such as the distinction between typical particles observable at ground level. Muons, produced in the upper atmosphere by the interaction of primary cosmic rays with air, interact very little in the detector whereas electrons or electromagnetic showers produced mainly by the interaction of muons with the atmosphere or with the structure of buildings can lead to large energy deposition.

The detector is based on plastic scintillator bars ($35.0 \times 2.5 \times 0.5 \text{ cm}^3$) with an encrusted wavelength shifting fibre (1 mm diameter) read out by single-channel SiPMs ($1.2 \times 1.2 \text{ mm}^2$). The bars are covered with a white TiO_2 -loaded paint to increase the light yield. The tracker comprises ten detection layers with a sensitive area of $1.00 \times 0.35 \text{ m}^2$ which are placed inside a light-tight box filling a total volume of approximately $1 \times 1 \times 1 \text{ m}^3$. Five 0.5 mm-thick layers of Pb are placed between the detection layers in order to discriminate between muons and electrons. The read-out system based on the VATA64 electronics was developed. Only one main electrical connexion and a computer are required to operate the detector which makes it easily portable. An inside view of the detector is shown in figure D.1.

A software was developed for the data acquisition and real-time display. A graphical interface based on Python Qt allows for the control and the configuration. The signal expected from muons is straight trajectories with low energy deposited in each layer. For corresponding events, a very simple pattern recognition algorithm finds straight tracks and calculates the angle. Muon events are also used to calibrated the MIP signal for each scintillating bar. A large fraction of the events observed when the detector is placed below a thick concrete ceiling is characterised with an electromagnetic shower produced by high energy electrons. The energy deposited in this type of events is enhanced if the shower crosses the lead layers generating many additional low energy electrons. Examples of such events are shown in figure D.2. The event rate after filtering by the software is typically 0.5 Hz.

The development and the fabrication of the detector took one year. A master student worked during one semester on the calibration of the SiPMs and measurements on the scintillating bars, allowing for the validation of the detector design. An intern student developed the

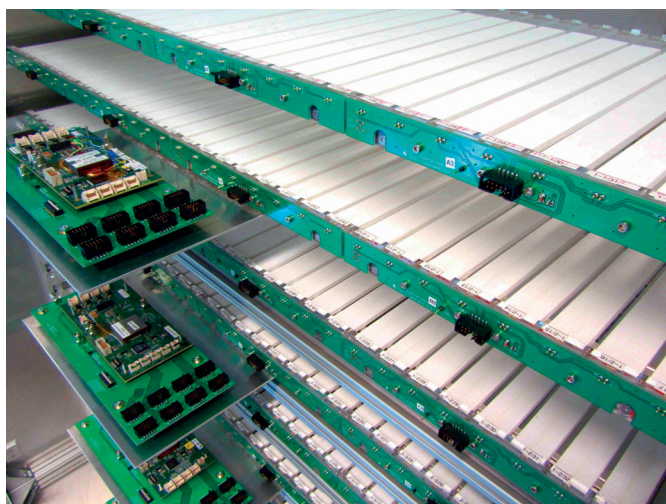


Figure D.1 – Picture of the cosmic tracker demonstrator. The detection layers are visible with the white scintillating bars.

graphical interface of the software and fabricated all scintillating bars in collaboration with the mechanical workshop during three months. Finally, the assembly of the detector and the read-out electronics took an additional two month period and involved the mechanical and electronics workshops as well as many other students.

The cosmic tracker was presented at the EPFL open days (2016) and at the EPFL's *salon des technologies et de l'innovation de Lausanne* (STIL, 2017 and 2018). The visitors of these different fairs include the general public but also students and innovation start-up managers. In all cases, presenting the tracker has been a good opportunity to initiate interesting discussions and present the activities of the laboratory as well as high energy physics in general.

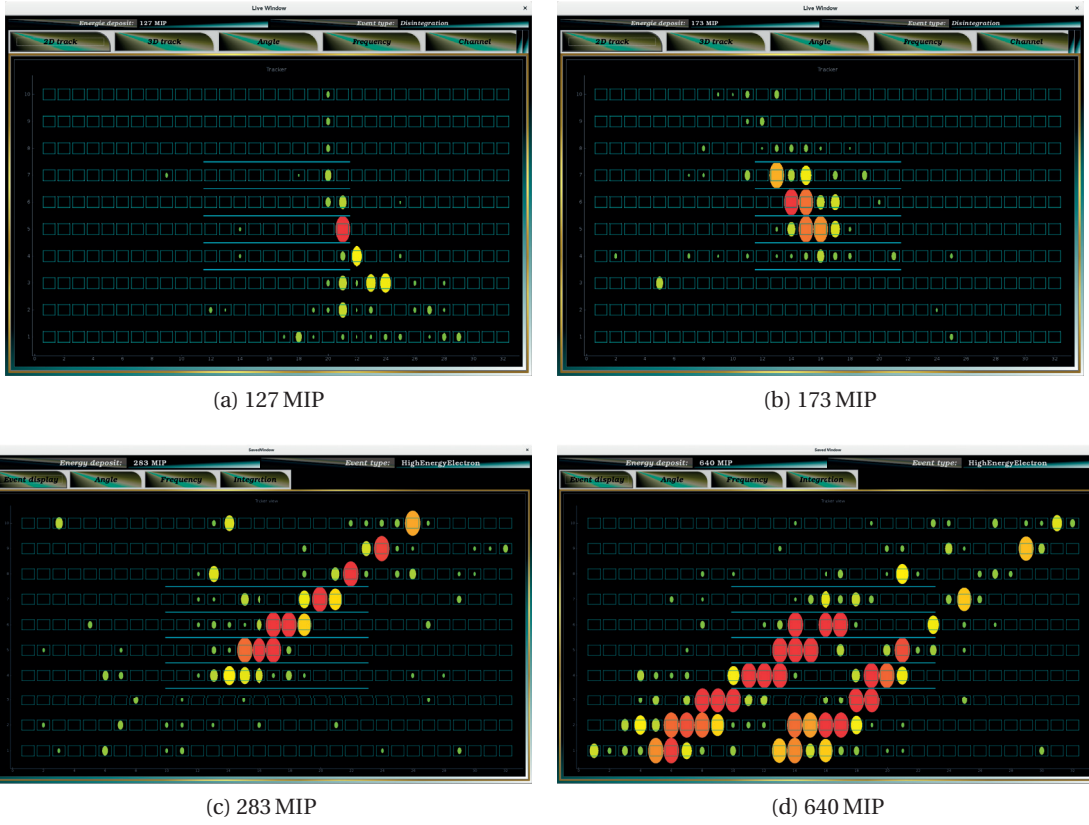
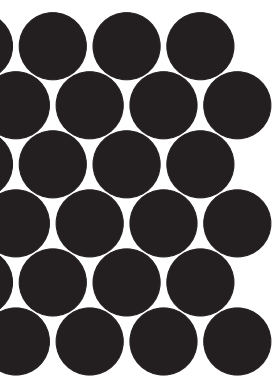


Figure D.2 – Cosmic particle tracker event display. The blue rectangles represent the scintillating bars whereas the horizontal light-blue lines (in the middle of the detector) indicate the position of the lead layers. The size and colour (from green to red) of the circles depict the signal amplitudes. Top left: One or a few electrons penetrating vertically and creating an electromagnetic shower in a lead layer that spreads at the bottom of the detector. Top right and bottom left: an electromagnetic shower created in the ceiling and being stopped by the lead. Bottom right: two simultaneous high energy showers that interact with the lead without being stopped. The deposited energy in units of MIP is indicated below the figures.



Bibliography

- [1] LHCb Collaboration, A. A. Alves, Jr. *et al.*, *The LHCb Detector at the LHC*, JINST **3** (2008) S08005.
- [2] LHCb Collaboration, R. Aaij *et al.*, *LHCb Detector Performance*, Int. J. Mod. Phys. **A30** (2015), no. 07 1530022, arXiv:1412.6352.
- [3] R. Aaij *et al.*, *Performance of the LHCb Vertex Locator*, JINST **9** (2014) 09007, arXiv:1405.7808.
- [4] LHCb Collaboration, *LHCb Silicon Tracker - Material for Publications*, <http://lhcb.physik.uzh.ch/ST/public/material/index.php>.
- [5] LHCb Outer Tracker Group, R. Arink *et al.*, *Performance of the LHCb Outer Tracker*, JINST **9** (2014), no. 01 P01002, arXiv:1311.3893.
- [6] LHCb Outer Tracker Group, P. d'Argent *et al.*, *Improved performance of the LHCb Outer Tracker in LHC Run 2*, JINST **12** (2017), no. 11 P11016, arXiv:1708.00819.
- [7] LHCb Collaboration, R. Aaij *et al.*, *Measurement of the track reconstruction efficiency at LHCb*, JINST **10** (2015), no. 02 P02007, arXiv:1408.1251.
- [8] LHCb Collaboration, *Letter of Intent for the LHCb Upgrade*, Tech. Rep. CERN-LHCC-2011-001, CERN, Geneva, 2011.
- [9] LHCb Collaboration, *LHCb VELO Upgrade Technical Design Report*, Tech. Rep. LHCb-TDR-013. CERN-LHCC-2013-021, CERN, Geneva, 2013.
- [10] LHCb Collaboration, *LHCb Tracker Upgrade Technical Design Report*, Tech. Rep. LHCb-TDR-015. CERN-LHCC-2014-001, CERN, Geneva, 2014.
- [11] LHCb Collaboration, *LHCb PID Upgrade Technical Design Report*, Tech. Rep. LHCb-TDR-014. CERN-LHCC-2013-022, CERN, Geneva, 2013.
- [12] LHCb Collaboration, *LHCb Trigger and Online Technical Design Report*, Tech. Rep. LHCb-TDR-016. CERN-LHCC-2014-016, CERN, Geneva, 2014.
- [13] C. Fitzpatrick *et al.*, *Upgrade trigger: Bandwidth strategy proposal*, Tech. Rep. LHCb-PUB-2017-006. CERN-LHCb-PUB-2017-006, CERN, Geneva, Feb, 2017.
- [14] LHCb SciFi Collaboration, *Material for conferences*, https://twiki.cern.ch/twiki/bin/view/LHCb/SciFiConference#Material_for_conferences.

- [15] A. Fasso *et al.*, *FLUKA: a multi-particle transport code*, 2005. CERN-2005-10, INFN/TC05/11, SLAC-R-773.
- [16] G. Battistoni *et al.*, *The FLUKA code: Description and benchmarking*, in *Proceedings of the Hadronic Shower Simulation Workshop 2006* (M. Albrow and R. Raja, eds.), AIP Conference Proceeding 896, pp. 31–49, 2007.
- [17] N. Lopez March and M. Karacson, *Radiation studies for the LHCb tracker upgrade*, Tech. Rep. LHCb-PUB-2014-022. CERN-LHCb-PUB-2014-022. LHCb-INT-2013-003, CERN, Geneva, Feb, 2014.
- [18] T. Matsumura *et al.*, *Effects of radiation damage caused by proton irradiation on multi-pixel photon counters (mppcs)*, Nucl. Instrum. Meth. **A603** (2009), no. 3 301 .
- [19] D. Clark, *The intrinsic scintillation efficiency of plastic scintillators for ^{60}Co gamma excitation*, Nucl. Instrum. Meth. **117** (1974), no. 1 295 .
- [20] S. Fukuda *et al.*, *The Super-Kamiokande detector*, Nucl. Instrum. Meth. **A501** (2003), no. 2 418 .
- [21] IceCube Collaboration, A. Achterberg *et al.*, *First Year Performance of The IceCube Neutrino Telescope*, Astropart. Phys. **26** (2006) 155, arXiv:astro-ph/0604450.
- [22] CTA Consortium, M. Actis *et al.*, *Design concepts for the Cherenkov Telescope Array CTA: An advanced facility for ground-based high-energy gamma-ray astronomy*, Exper. Astron. **32** (2011) 193, arXiv:1008.3703.
- [23] Particle Data Group, C. Patrignani *et al.*, *Review of Particle Physics*, Chin. Phys. **C40** (2016), no. 10 100001.
- [24] P. Križan and S. Korpar, *Photodetectors in particle physics experiments*, Annual Review of Nuclear and Particle Science **63** (2013), no. 1 329, arXiv:https://doi.org/10.1146/annurev-nucl-102212-170604.
- [25] Hamamatsu Photonics K. K., *Photomultiplier Tubes: basics and applications*, 3a ed., 2007.
- [26] BaBar DIRC Collaboration, I. Adam *et al.*, *The DIRC particle identification system for the BaBar experiment*, Nucl. Instrum. Meth. **A538** (2005) 281.
- [27] K. Föhl *et al.*, *TORCH - Cherenkov and Time-of-Flight PID Detector for the LHCb Upgrade at CERN*, JINST **11** (2016), no. 05 C05020.
- [28] T. M. Conneely *et al.*, *The TORCH PMT: a close packing, multi-anode, long life MCP-PMT for Cherenkov applications*, JINST **10** (2015), no. 05 C05003.
- [29] Belle-II Collaboration, T. Abe *et al.*, *Belle II Technical Design Report*, arXiv:1011.0352.
- [30] S. Franz and P. Barrillon, *ATLAS ALFA — measuring absolute luminosity with scintillating fibres*, Nucl. Instrum. Meth. **A610** (2009), no. 1 35, New Developments In Photodetection NDIP08.

-
- [31] Hamamatsu Photonics K. K., *Opto-Semiconductor Handbook: solid state photodetectors*, 2014.
- [32] R. J. McIntyre, *Multiplication noise in uniform avalanche diodes*, IEEE Transactions on Electron Devices **ED-13** (1966) 164.
- [33] E. Waks *et al.*, *High-efficiency photon-number detection for quantum information processing*, IEEE Journal of Selected Topics in Quantum Electronics **9** (2003) 1502 .
- [34] BaBar Collaboration, D. Boutigny *et al.*, *BaBar technical design report*, in *BaBar Technical Design Report EPAC Meeting Stanford, California, March 17-18, 1995*, 1995.
- [35] C. Biino, *The CMS Electromagnetic Calorimeter: overview, lessons learned during Run 1 and future projections*, Journal of Physics: Conference Series **587** (2015), no. 1 012001.
- [36] CALET, S. Torii, *The CALorimetric Electron Telescope (CALET): a High-Energy Astroparticle Physics Observatory on the International Space Stati*, PoS **ICRC2015** (2016) 581.
- [37] CMS Collaboration, *Technical proposal for a MIP timing detector in the CMS experiment phase 2 upgrade*, Tech. Rep. CERN-LHCC-2017-027. LHCC-P-009, CERN, Geneva, Dec, 2017.
- [38] A. Fukasawa *et al.*, *High Speed HPD for Photon Counting*, IEEE Transactions on Nuclear Science **55** (2008) 758.
- [39] LHCb Collaboration, S. Amato *et al.*, *LHCb RICH: Technical Design Report*, Technical Design Report LHCb, CERN, Geneva, 2000.
- [40] Y. Yusa, *ARICH for Belle II*, JINST **9** (2014), no. 10 C10015.
- [41] Hyper-Kamiokande Collaboration, *Hyper-Kamiokande Design Report*, 2016.
- [42] ALICE Collaboration, K. Aamodt *et al.*, *The ALICE experiment at the CERN LHC*, JINST **3** (2008), no. 08 S08002.
- [43] R. H. Haitz, *Model for the electrical behavior of a microplasma*, Journal of Applied Physics **35** (1964), no. 5 1370, arXiv:<https://doi.org/10.1063/1.1713636>.
- [44] R. J. McIntyre, *Theory of microplasma instability in silicon*, Journal of Applied Physics **32** (1961), no. 6 983, arXiv:<https://doi.org/10.1063/1.1736199>.
- [45] C. Piemonte, *A new Silicon Photomultiplier structure for blue light detection*, Nucl. Instrum. Meth. **A568** (2006), no. 1 224, New Developments in Radiation Detectors.
- [46] D. Renker and E. Lorenz, *Advances in solid state photon detectors*, JINST **4** (2009), no. 04 P04004.
- [47] KETEK GmbH, *Microcell construction*, <https://www.ketek.net/sipm/technology/microcell-construction/>. Accessed: 06.04.2018.
- [48] C. R. Crowell and S. M. Sze, *Temperature dependence of avalanche multiplication in semiconductors*, Applied Physics Letters **9** (1966), no. 6 242, arXiv:<https://doi.org/10.1063/1.1754731>.

- [49] G. Collazuol *et al.*, *Studies of silicon photomultipliers at cryogenic temperatures*, Nucl. Instrum. Meth. **A628** (2011), no. 1 389 , VCI 2010.
- [50] F. Corsi *et al.*, *ASIC development for SiPM readout*, JINST **4** (2009), no. 03 P03004.
- [51] T. Nagano *et al.*, *Improvement of Multi-Pixel Photon Counter (MPPC)*, pp. 1657–1659, Oct, 2011. doi: 10.1109/NSSMIC.2011.6154655.
- [52] A. N. Otte, D. Garcia, T. Nguyen, and D. Purushotham, *Characterization of Three High Efficiency and Blue Sensitive Silicon Photomultipliers*, Nucl. Instrum. Meth. **A846** (2017) 106, arXiv:1606.05186.
- [53] SensL Technologies, Ltd., *An Introduction to the Silicon Photomultiplier*, 2011.
- [54] N. Otte, *The Silicon Photomultiplier: A New Device for High Energy Physics, Astroparticle Physics, Industrial and Medical Applications*, eConf **C0604032** (2006) 0018.
- [55] A. L. Lacaita, F. Zappa, S. Bigliardi, and M. Manfredi, *On the bremsstrahlung origin of hot-carrier-induced photons in silicon devices*, IEEE Transactions on Electron Devices **40** (1993) 577.
- [56] F. Acerbi *et al.*, *NUV Silicon Photomultipliers With High Detection Efficiency and Reduced Delayed Correlated-Noise*, IEEE Transactions on Nuclear Science **62** (2015) 1318.
- [57] S. Vinogradov, *Analytical models of probability distribution and excess noise factor of solid state photomultiplier signals with crosstalk*, Nucl. Instrum. Meth. **A695** (2012) 247, arXiv:1109.2014.
- [58] A. Gola *et al.*, *SiPM optical crosstalk amplification due to scintillator crystal: effects on timing performance*, Physics in Medicine and Biology **59** (2014), no. 13 3615.
- [59] M. Moll, *Radiation damage in silicon particle detectors: Microscopic defects and macroscopic properties*, PhD thesis, Hamburg U., 1999.
- [60] Y. Musienko *et al.*, *Radiation damage studies of silicon photomultipliers for the CMS HCAL phase I upgrade*, Nucl. Instrum. Meth. **A787** (2015) 319 , New Developments in Photodetection NDIP14.
- [61] A. Heering *et al.*, *Effects of very high radiation on SiPMs*, Nucl. Instrum. Meth. **A824** (2016) 111 , Frontier Detectors for Frontier Physics: Proceedings of the 13th Pisa Meeting on Advanced Detectors.
- [62] C. Joram, G. Haefeli, and B. Leverington, *Scintillating fibre tracking at high luminosity colliders*, JINST **10** (2015), no. 08 C08005.
- [63] T. O. White, *Scintillating fibres*, Nucl. Instrum. Meth. **A273** (1988), no. 2 820 .
- [64] O. Borshchev *et al.*, *Development of a new class of scintillating fibres with very short decay time and high light yield*, JINST **12** (2017), no. 05 P05013.
- [65] C. D’Ambrosio *et al.*, *Organic scintillators with large stokes shifts dissolved in polystyrene*, Nucl. Instrum. Meth. **A307** (1991), no. 2 430 .

-
- [66] M. Deckenhoff, *Scintillating Fibre and Silicon Photomultiplier Studies for the LHCb upgrade*, PhD thesis, Dortmund U., 2015-12-22.
- [67] C. Joram *et al.*, *LHCb Scintillating Fibre Tracker Engineering Design Review Report: Fibres, Mats and Modules*, Tech. Rep. LHCb-PUB-2015-008. CERN-LHCb-PUB-2015-008, CERN, Geneva, Mar, 2015.
- [68] A. B. Rodrigues Cavalcante, I. Bediaga, and C. Joram, *CP violation studies in three-body charmless B^\pm decays and contributions to the LHCb SciFi Tracker*, PhD thesis, Jul, 2017, Presented 28 Aug 2017.
- [69] J. Broll, *Experimental and simulation studies of crosstalk between scintillating fibres for the SciFi Tracker of the LHCb Upgrade*, Master's thesis, TU Dortmund, 2018.
- [70] M. S. Bieker, *Simulation Studies for the Scintillating Fibre Tracker of the LHCb Experiment*, Master's thesis, TU Dortmund, 2018.
- [71] S. Nieswand, *Measurement of the exit characteristics of light from optical multimode plastic fibres*, Master's thesis, RWTH Aachen, 2014.
- [72] S. Giani *et al.*, *Digitization of SiPM signals for the LHCb Upgrade SciFi tracker*, Tech. Rep. LHCb-PUB-2014-025. CERN-LHCb-PUB-2014-025. LHCb-INT-2013-065, CERN, Geneva, Feb, 2014.
- [73] C. Joram and T. Schneider, *Mirroring of fibre ends for the LHCb SciFi project*, Tech. Rep. LHCb-PUB-2014-020. CERN-LHCb-PUB-2014-020. LHCb-INT-2013-060, CERN, Geneva, Feb, 2014.
- [74] R. J. Ekelhof and B. Spaan, *Studies for the LHCb SciFi Tracker - Development of Modules from Scintillating Fibres and Tests of their Radiation Hardness*, PhD thesis, Mar, 2016, Presented 18 May 2016.
- [75] G. Pietrzyk, *SciFi mat: optical scan example*, Private communication, March, 2018.
- [76] P. von Doetinchem *et al.*, *PEBS — Positron electron balloon spectrometer*, Nucl. Instrum. Meth. **A581** (2007), no. 1 151 , VCI 2007.
- [77] B. Beischer *et al.*, *A high-resolution scintillating fiber tracker with silicon photomultiplier array readout*, Nucl. Instrum. Meth. **A622** (2010), no. 3 542 .
- [78] W. E. W. Vink *et al.*, *LHCb Scintillating Fiber detector front end electronics design and quality assurance*, JINST **12** (2017), no. 03 C03053.
- [79] J. Mazorra *et al.*, *PACIFIC: the readout ASIC for the SciFi Tracker of the upgraded LHCb detector*, JINST **11** (2016), no. 02 C02021.
- [80] A. Caratelli *et al.*, *The GBT-SCA, a radiation tolerant ASIC for detector control and monitoring applications in HEP experiments*, JINST **10** (2015), no. 03 C03034.
- [81] V. Radulovic *et al.*, *Large Object Irradiation Facility In The Tangential Channel Of The JSI TRIGA Reactor*, tech. rep., May, 2017.

- [82] M. M. Federico Ravotti, Maurice Glaser, *Active Radiation Monitoring Sensors for the High-Energy Physics Experiments of the CERN LHC*, RADMON Working Group, CERN, Technical Support Department.
- [83] M. Auger *et al.*, *Accelerator and detector physics at the Bern medical cyclotron and its beam transport line*, *Nukleonika* **61** (2016), no. 1 .
- [84] J. Anders *et al.*, *A facility for radiation hardness studies based on the Bern medical cyclotron*, arXiv:1803.01939.
- [85] LHCb SciFi Collaboration, *LHCb Scintillating Fibre Tracker Engineering Design Review: Silicon Photomultipliers*, Tech. Rep. LHCb-INT-2016-019. LPHE-2016-005, CERN, Geneva, April, 2016. <https://lphe.epfl.ch/publications/2016/LPHE-2016-005.pdf>.
- [86] R. Brun and F. Rademakers, *ROOT - An Object Oriented Data Analysis Framework*, Proceedings AIHENP'96 Workshop, Lausanne, Sep. 1996, Nucl. Inst. & Meth. in Phys. Res. A 389 (1997).
- [87] C. Piemonte *et al.*, *Development of an automatic procedure for the characterization of silicon photomultipliers*, in *2012 IEEE Nuclear Science Symposium and Medical Imaging Conference (NSS/MIC 2012)*, pp. 428–432, 2012. doi: 10.1109/NSSMIC.2012.6551141.
- [88] V. Arosio, M. Beretta, M. Caccia, and R. Santoro, *A robust and semi-automatic procedure for Silicon Photomultipliers characterisation*, *JINST* **12** (2017), no. 03 C03030.
- [89] L. Gallego, J. Rosado, F. Blanco, and F. Arqueros, *Modeling crosstalk in silicon photomultipliers*, *JINST* **8** (2013), no. 05 P05010.
- [90] A. Gola, C. Piemonte, and A. Tarolli, *The DLED Algorithm for Timing Measurements on Large Area SiPMs Coupled to Scintillators*, *IEEE Transactions on Nuclear Science* **59** (2012) 358.
- [91] M. E. Stramaglia, *Photon detection efficiency measurement setup*, Private communication, December, 2017.
- [92] E. Garutti *et al.*, *Characterization and X-Ray Damage of Silicon Photomultipliers*, *PoS TIPP2014* (2014) 070.
- [93] Z. Guoqing, H. Dejun, Z. Changjun, and Z. Xuejun, *Turn-on and turn-off voltages of an avalanche p—n junction*, *Journal of Semiconductors* **33** (2012), no. 9 094003.
- [94] S. C. Arfaoui, C. C. Joram, and C. E. Z. Casella, *Characterisation of a Sr-90 based electron monochromator*, Tech. Rep. PH-EP-Tech-Note-2015-003, CERN, Geneva, May, 2015.
- [95] M. G. Bagliesi *et al.*, *A custom front-end ASIC for the readout and timing of 64 SiPM photosensors*, *Nucl. Phys. Proc. Suppl.* **B215** (2011), no. 1 344 , Proceedings of the 12th Topical Seminar on Innovative Particle and Radiation Detectors (IPRD10).
- [96] S. C. D. Lorenzo *et al.*, *SPIROC: design and performances of a dedicated very front-end electronics for an ILC Analog Hadronic CALorimeter (AHCAL) prototype with SiPM readout*, *JINST* **8** (2013), no. 01 C01027.

-
- [97] S. Löchner and M. Schmelling, *The Beetle Reference Manual - chip version 1.3, 1.4 and 1.5*, Tech. Rep. LHCb-2005-105. CERN-LHCb-2005-105, CERN, Geneva, Nov, 2006.
- [98] O. Girard, G. Haefeli, A. Kuonen, and M. E. Stramaglia, *Read-out of irradiated SiPMs attached to short scintillating fibre module*, Tech. Rep. LPHE Note 2017-002, EPFL, Lausanne, 2017.
- [99] *HL-LHC Preliminary Design Report: Deliverable: D1.5*, tech. rep., Nov, 2014.
- [100] P. Hopchev *et al.*, *A Beam Gas Vertex Detector for Beam Size Measurement in the LHC*, in *Proceedings, 5th International Particle Accelerator Conference*, p. 175, 2014.
- [101] S. Vlachos *et al.*, *The LHC Beam Gas Vertex Detector - a Non-Invasive Profile Monitor for High Energy Machines*, in *2017 International Beam Instrumentation Conference*, 2017.
- [102] A. Alexopoulos *et al.*, *First LHC transverse beam size measurements with the beam gas vertex detector*, J. Phys. : Conf. Ser. **874** (2017), no. CERN-ACC-2017-315. 1 012086. 6 p.
- [103] LHCb Collaboration, *Precision luminosity measurements at LHCb*, JINST **9** (2014), no. 12 P12005.
- [104] P. Hopchev and B. Pietrzyk, *Absolute luminosity measurements at LHCb*, PhD thesis, 2011.
- [105] C. Barschel, *Precision luminosity measurement at LHCb with beam-gas imaging*, PhD thesis, RWTH Aachen U., 2014.
- [106] A. Kuonen, O. Girard, and G. Haefeli, *Characterisation of the Hamamatsu MPPC multi-channel array for LHCb SciFi Tracker v.9.2014*, Tech. Rep. LPHE Note 2015-001, EPFL, Lausanne, 2015.
- [107] Q. Veyrat and M. Ferro-Luzzi, *BGV Full MC Simulation - Particles fluence/dose on SiPM*, Presented at the BGV meeting 26, January, 2014.
- [108] A. Alexopoulos and O. Girard, *BGV radiation monitors reading*, Private communication, June, 2018.
- [109] V. Salustino Guimaraes and M. Santana Rangel, *Associated vector boson production with b-jets at LHCb and Beam-Gas Vertexing at LHC for beam instrumentation*, PhD thesis, Mar, 2016.
- [110] O. Girard, *Optimisation and validation of the cooling design and read-out electronics for the LHC Beam Gas Vertex detector modules*, Master's thesis, EPFL Lausanne, 2014.
- [111] G. Haefeli and A. Bay, *Contribution to the development of the acquisition electronics for the LHCb experiment*, PhD thesis, 2014.
- [112] K. Akiba *et al.*, *The algorithm for FIR corrections of the VELO analogue links and its performance*, Tech. Rep. LHCb-2008-015. CERN-LHCb-2008-015, CERN, Geneva, Jul, 2007.

Bibliography

- [113] O. Girard *et al.*, *BGV fibre module read-out, signal correction and clustering*, Tech. Rep. LPHE Note 2016-002, EPFL, Lausanne, 2016.
- [114] G. Haefeli and A. Gong, *LHCb VELO and ST clusterization on TELL1*, Tech. Rep. EDMS 690585, CERN, Geneva, 2006.
- [115] O. Girard, L. An, A. Kuonen, and G. Haefeli, *BGV fibre module - Test beam report*, Tech. Rep. LPHE Note 2016-004, EPFL, Lausanne, 2016.
- [116] O. Girard, G. Haefeli, A. Kuonen, and M. E. Stramaglia, *Modular telescope based on scintillating fibres coupled with low noise silicon photomultipliers*, in *6th Beam Telescopes and Test Beams Workshop*, 2018.
- [117] A. B. Rodrigues Cavalcante *et al.*, *LHCb Scintillating Fibre Tracker: Test Beam Report 2015*, Tech. Rep. LHCb-PUB-2015-025. CERN-LHCb-PUB-2015-025, CERN, Geneva, Nov, 2015.
- [118] K. Akiba *et al.*, *The Timepix Telescope for High Performance Particle Tracking*, Nucl. Instrum. Meth. **A723** (2013) 47, arXiv:1304.5175.
- [119] R. Battiston, *A Silicon tracker for the antimatter spectrometer on the international space station Alpha*, Nucl. Phys. Proc. Suppl. **44** (1995) 274.
- [120] B. D. Leverington, *Test beam results of the LHCb Scintillating Fibre Tracker*, in *6th Beam Telescopes and Test Beams Workshop*, 2018.
- [121] LHCb SciFi Tracker Collaboration, M. Deckenhoff, *Scintillating Fibre and Radiation Damage Studies for the LHCb Upgrade*, PoS **TIPP2014** (2014) 091.
- [122] A. B. Rodrigues Cavalcante *et al.*, *Irradiation of a 2.5 m long SciFi module with 24 GeV/c protons to the dose profile expected in LHCb*, Tech. Rep. LHCb-PUB-2016-001. CERN-LHCb-PUB-2016-001, CERN, Geneva, Jan, 2015.
- [123] C. Joram *et al.*, *Irradiation test of mirror samples for the LHCb SciFi tracker*, Tech. Rep. LHCb-PUB-2016-006. CERN-LHCb-PUB-2016-006, CERN, Geneva, Feb, 2016.
- [124] A. D. Bross and A. Pla-Dalmau, *Radiation damage of plastic scintillators*, IEEE Transactions on Nuclear Science **39** (1992) 1199.
- [125] H. Blumenfeld and M. Bourdinaud, *Aging of plastic scintillating fibers*, Tech. Rep. SACLAY-DPHPE-90-12, 1990.
- [126] A. Kuonen, *Characterisation of silicon photo multiplier arrays for the LHCb Scintillating Fibre Tracker Upgrade*, Master's thesis, EPFL Lausanne, 2014.
- [127] A. Kuonen *et al.*, *Characterisation of the Hamamatsu MPPC multichannel array for LHCb SciFi Tracker v.12.2015*, Tech. Rep. LPHE Note 2016-001, EPFL, Lausanne, 2016.
- [128] R. Mankel, *Measurement of the Transverse Beam Line Width Using Impact Parameter Correlations*, Tech. Rep. CMS AN-2010/196, CERN, Geneva, Jun, 2010.
- [129] S. Donati and L. Ristori, *Measuring beam width and SVX impact parameter resolution*, Tech. Rep. CDF-Note-4189, Fermilab, Batavia, IL, U.S.A., 2003.

Olivier GIRARD

Swiss and Swedish citizenship
28 years old
Married

Rue du Borgeaud 10B
1196 Gland
+41 77 403 46 18
girard_olivier@bluewin.ch



EDUCATION

EPFL, Ecole polytechnique fédérale de Lausanne

- Doctoral study in particle physics on the subject:
Development of a technology based on scintillating fibres (SciFi) and silicon photomultipliers (SiPM) for new instruments at CERN (LHCb detector upgrade and beam monitoring system for the LHC) 2014 – present
- Bachelor and Master in Engineering Physics 2009 – 2014
Specialisation: high energy physics

KTH, Royal Institute of Technology, Stockholm, Sweden

- Third year of studies in academic exchange 2011 – 2012

WORK EXPERIENCE

EPFL, Ecole polytechnique fédérale de Lausanne

09/2014 – present

- Teaching assistant for Bachelor and Master courses
- Supervisor for Bachelor and Master students (semester projects) and intern in detector development

CSEM SA, Basel

08/2013 – 01/2014

- R&D in fabrication and characterisation of large-surface organic light-emitting diodes (OLED)
- Projects in touch with industrial partners
- Extensive study of the charge carrier mobility in organic materials

CERN, Geneva

06/2012 – 09/2012

- Characterisation of the radiation-induced damage of silicon detectors in the framework of the CERN silicon sensor R&D group
- Development of a charge transport characterisation method based on the photocurrent analysis
- Attendance at several conferences on physics research performed at CERN

SELECTION OF R&D PROJECTS

Silicon photomultipliers for the LHCb detector upgrade at CERN

09/2014 – present

*Long R&D process with several industrials
Automation of characterisation setups, quality assurance of 5500 photodetectors*

New beam monitoring system for the LHC at CERN

02/2014 – 07/2017

*From R&D to commissioning of a particle tracker
Validation of the system for other particle accelerators*

Cosmic particle tracker for outreach

01/2016 – 10/2016

*Design, development and construction of a 1m³ detector
Custom software for live event visualisation
Presented at exhibitions at EPFL (general public, students, innovation start-ups)*

Balloon-borne cosmic gamma-ray detector

02/2013 – 07/2013

*Development of a light-weight detector and read-out electronics (Arduino-based)
Successful launch in the upper atmosphere (35km altitude) in collaboration with MétéoSuisse*

CONFERENCES, SCHOOLS AND WORKSHOPS

6th Beam telescope and test beam workshop , Zürich	01/2018
<i>Talk: Modular beam telescope based on scintillating fibres and silicon photomultipliers</i>	
IEEE Nuclear Science Symposium & Medical Imaging Conference , Atlanta, USA	10/2017
<i>Poster: Silicon photomultiplier multichannel arrays for the LHCb scintillating fibre tracker</i>	
Swiss Physical Society annual meeting , Lugano	08/2016
<i>Talk: Scintillating fibre technology for the next LHCb tracking system and other applications</i>	
Austrian and Swiss Physical society joint meeting , Vienna, Austria	09/2015
<i>Poster: R&D for SiPM based scintillating fibre tracker in high energy physics</i>	
EIROforum School on Instrumentation , Garching, Germany	06/2015
<i>Poster: Read-out of irradiated silicon photo-multipliers attached to a short fibre module</i>	
<i>Award for the best poster</i>	

TECHNICAL SKILLS

Strong R&D experience

Solid-state device characterisation, measurement setup automation (f.ex. quality assurance), read-out electronics (debugging), custom device fabrication (f.ex. OLED), collaboration with industrials

Programming and scientific softwares

Data monitoring and analysis using: C++, Python, Qt, Matlab, LabView, ROOT (CERN data analysis), Git

Office

LaTeX, Microsoft Office, Adobe Photoshop, Inkscape

Operating system

Unix/Linux, Microsoft Windows

LANGUAGES

French	Mother language
English	Fluent (C1), working language
German	Intermediate (B1-B2), six months of internship in Basel
Swedish	Intermediate (B1), one year of studies in Sweden
Italian	Beginner (A2)

OTHER WORK EXPERIENCE

Student jobs	2006 – 2014
<i>EPFL: assistant for experimental works during my studies; Migros; MGB SA (equipment for paper mills/bookshops); city of Nyon; Compass Group SA (Nyon's high school restaurant); private lessons in physics for scholars and high school students</i>	

INTERESTS

Sports	Volleyball, football, running, hiking, ski
Astronomy	Amateur astronomy, astrophotography, sky observations, outreach
Others	Travelling, meeting friends, Staff member of Paléo festival during several Summers

